Journal of Seismic Exploration

ISSN: 0963-0651

Volume 34 · Issue 2
2025

ACCSCIENCE PUBLISHING

State Key Laboratory for Fine Exploration and Intelligent Development of Coal Resources

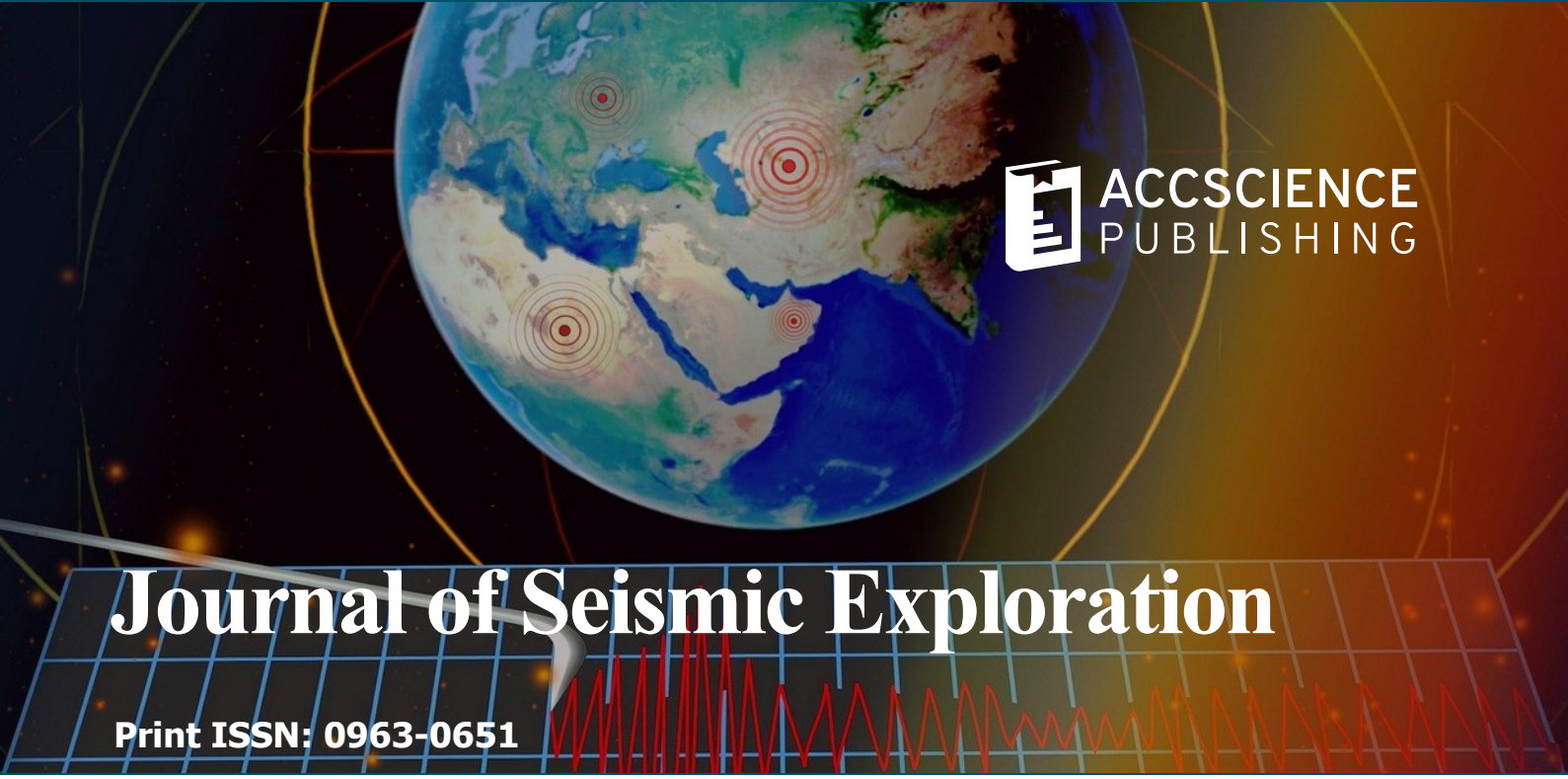

Journal of Seismic Exploration

Print ISSN: 0963-0651

The Journal of Seismic Exploration (JSE) is an international medium for the publication of research in seismic modeling, processing, inversion, interpretation, field techniques, borehole techniques, tomography, instrumentation and software. The aim and goal of JSE is to serve the interests and objectives of seismic petroleum exploration. All seismic processing methods have assumptions and prerequisites- and when they are satisfied methods are effective-and when they are violated methods become ineffective and can fail. The latter contributes to drilling dry hole exploration wells and suboptimal development wells.

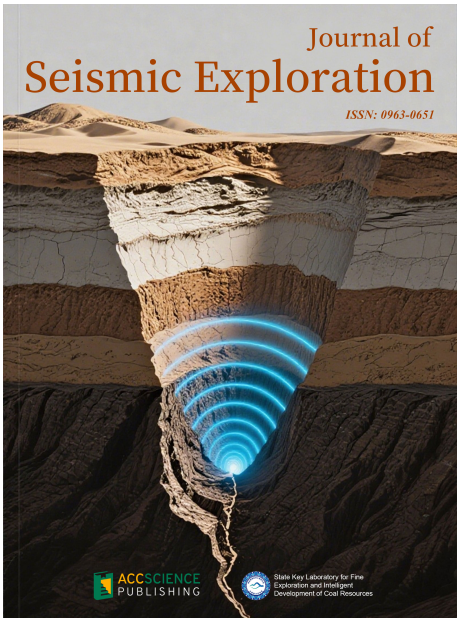

About the Publisher

AccScience Publishing is a publishing company based in Singapore. We publish a range of high-quality, open-access, peer-reviewed journals and books from a broad spectrum of disciplines.

Contact Us

Managing Editor
jse.office@accscience.sg

AccScience Publishing
9 Raffles Place, Republic Plaza 1 #06-00 Singapore 048619.

Volume 34 • Issue 2 • 2025
ISSN 0963-0651 (print)

Journal of Seismic Exploration

ACCSCIENCE PUBLISHING

Access Science Without Barriers

JOURNAL OF SEISMIC EXPLORATION

ISSN: 0963-0651 (print)

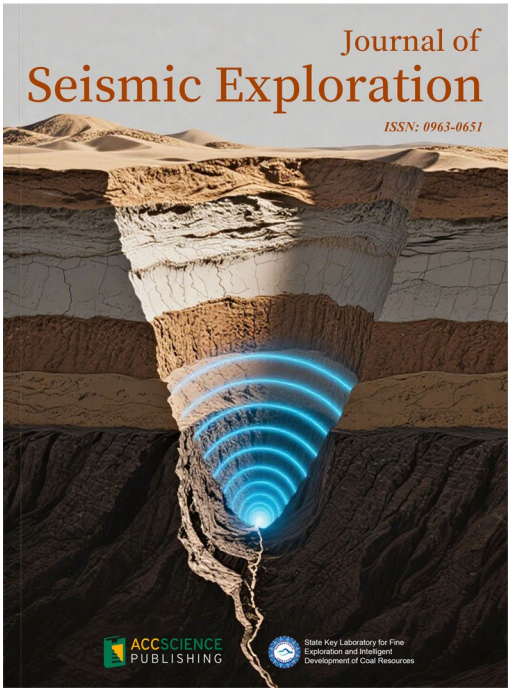

Editorial and Production Credits

Publisher: AccScience Publishing
Managing Editor: Gary Liu
Production Editor: Lim Mingyuan
Article Layout and Typeset: Sinjore Technologies (India)

Supplementary file

Supplementary files of articles can be obtained at https://accscience.com/journal/JSE/34/2.

Disclaimer

AccScience Publishing is not liable to the statements, perspectives, and opinions contained in the publications. The appearance of advertisements in the journal shall not be construed as a warranty, endorsement, or approval of the products or services advertised and/or the safety thereof. AccScience Publishing disclaims responsibility for any injury to persons or property resulting from any ideas or products referred to in the publications or advertisements. AccScience Publishing remains neutral with regard to jurisdictional claims in published maps and institutional affiliations.

Journal of Seismic Exploration

Editorial Board

ACCSCIENCE PUBLISHING

Volume 34 | Issue 2 | Page 1 – 72 |

Journal of Seismic Exploration

https://accscience.com/journal/JSE

CONTENTS

ARTICLES

1 **Modeling the seismic wave equation using a staggered grid finite-difference method optimized with a genetic algorithm**
Mounika Vanga, Maheswar Ojha

14 **An innovative method for computing static corrections using seismic reflection horizons analysis**
Youcef LADJADJ, Mohamed Cherif BERGUIG, Said GACI

28 **Optimization of the SOM neural network model using CEEMDAN distribution entropy and ALO for seismic and blasting identification**
Ailing Wang, Cong Pang, Guoqing Chen, Chawei Li, Tianwen Zhao

44 **Seismic signal denoising using variational mode decomposition and a denoising convolutional neural network**
Shengrong Zhang, Liang Zhang, Xuesha Qin

60 **Microseismic event locations using grid-searching method and Newton–Raphson-based optimizer**
Shaohui Zhou, Tianqi Jiang, Junhao Qu, Peng Lin, Yu Wang, Yajun Li

RETRACTION

72 **Retraction Note for "Efficient and low-cost node seismic data recovery based on curvelet compression sensing"**
Editorial Office of Journal of Seismic Exploration

ACCSCIENCE PUBLISHING

Journal of Seismic Exploration

ARTICLE

Modeling the seismic wave equation using a staggered grid finite-difference method optimized with a genetic algorithm

Mounika Vanga[1,2] and Maheswar Ojha[1,2]*

[1]CSIR – National Geophysical Research Institute, Uppal Road, Hyderabad-500007, Telangana, India

[2]Academy of Scientific and Innovative Research (AcSIR), Ghaziabad, Uttar Pradesh-201002, India

(This article belongs to the *Special Issue: Full Waveform Inversion Methods and Applications for Seismic Data in Complex Media*)

Abstract

Simulation of seismic waves is a critical component in the imaging of subsurface structures using actual data, where numerical dispersion remains a challenging task. The finite-difference (FD) approach is popular for solving wave equations because it is simple to implement and requires less memory and computing time due to recursion. However, the staggered grid finite-difference (SGFD) methods have gained popularity due to their improved accuracy and stability. In this study, we introduce an optimization approach using a genetic algorithm (GA) to minimize numerical dispersion. The SGFD coefficients were optimized to reduce numerical errors and improve the accuracy of seismic wave simulations, considering both spatial and temporal domains. Numerical simulations applied to both homogeneous and heterogeneous velocity models demonstrate that the GA-optimized SGFD schemes achieve substantial reductions in dispersion, even with lower-order approximations, when compared to other methods. An important advantage of the proposed method is that it maintains high accuracy while using lower-order approximations, which significantly reduces computational costs. For example, the optimization of 12^{th}-order FD coefficients took approximately 20 s on a standard computer with 64 GB RAM. The findings demonstrate the efficiency of the proposed approach in improving the accuracy and stability of seismic wave simulations, providing a reliable solution for high-resolution seismic imaging.

Keywords: Numerical dispersion; Seismic wavefield; Staggered grid finite-difference method; Genetic algorithm; Modeling; Optimization

***Corresponding author:**
Maheswar Ojha
(maheswarojha.ngri@csir.res.in)

Citation: Vanga M, Ojha M. Modeling of seismic wave equation using staggered grid finite-difference method, optimized by genetic algorithm. *J Seismic Explor*. 2025;34(2):1-13.
doi: 10.36922/JSE025290035

Received: July 15, 2025

Revised: July 29, 2025

Accepted: July 30, 2025

Published online: August 15, 2025

1. Introduction

The numerical simulation of seismic waves has several applications in both applied seismic and seismology, and it is essential for understanding the Earth's subsurface structure. The finite-difference method (FDM) is one of the most popular techniques used to solve wave equations.[1-4] However, despite its popularity, the issue of numerical dispersion in simulating seismic waves remains a significant challenge. Numerical dispersion is a phenomenon that occurs in numerical simulations of wave propagation,

where the phase velocity depends on its wavelength and the discretization parameters of the numerical method. This leads to artificial distortion of the wave as it travels through the computational domain.

The numerical representation of a wave equation introduces errors that alter the phase velocity of the wave components. The causes of numerical dispersion include inadequate spatial or temporal resolution (i.e., large grid spacing or time steps), the choice of numerical scheme, and its truncation errors. Wave components with shorter wavelengths are more susceptible to numerical dispersion. The effects of dispersion may manifest as waves appearing to travel at incorrect speeds, smearing, or degraded modeling accuracy. Numerical dispersion is analyzed through the dispersion relation, which relates the numerical wavenumber to the physical wavenumber.

Alternative numerical approaches, including the Finite Element Method[5-9] and Finite Volume Method,[10-12] can be employed. Moreover, different grid schemes—such as conventional grid, staggered grid, variable grid, irregular grid—and various explicit and implicit formulas, offer further alternatives for numerical modeling. Staggered grid finite-difference (SGFD) methods, in particular, have gained prominence due to their enhanced accuracy and stability compared to conventional grid FDMs. The key distinction in SGFD methods is the utilization of first-order stress and strain relations instead of the direct second-order displacement relations. This approach not only increases accuracy but also leads to faster convergence[13] by reducing interpolation errors.

In general, finite-difference (FD) coefficients are determined through two main approaches: Taylor series expansion and optimization. Taylor series expansion involves representing functions as polynomials and estimating FD coefficients by comparing the coefficients of the polynomial dispersion relation equations.[14-17] Optimization methods[18-23] seek to minimize the dispersion error using techniques such as least squares, simulated annealing, and the sampling approximation method.[24] Recent studies also explore reducing dispersion at low wavenumbers using Lagrange dual problems[25] and explicit methods with optimized constant coefficients.[26]

Conventionally, SGFD coefficients are calculated in the space domain, but the dispersion relation depends on both space and time domains. Therefore, to achieve greater accuracy at designated frequencies, it is necessary to consider both domains.[14] A recent study[4] proposed an optimized FDM that minimizes dispersion by deriving explicit (conventional grid) FD coefficients using a genetic algorithm (GA). This method uses the combined time and space dispersion relation to compute FD coefficients adaptively based on parameters such as velocity, grid size, and time sampling to achieve greater accuracy.

SGFD methods have several advantages over conventional grid FDMs. SGFD methods can handle a wider range of grid geometries and boundary conditions than conventional grid methods. They are less constrained by Courant number limitations, which can significantly reduce computing time by allowing the use of greater time steps without compromising stability. In addition, SGFD methods are well-suited to optimization techniques. Improved results can be obtained by further minimizing numerical dispersion through the optimization of FD coefficients.

We implemented an approach to solve the wave equation using SGFD with GA, aiming to decrease numerical dispersion and computation time. The SGFD coefficients were derived from a dispersion relation by considering both time and space, using plane wave theory. The normalized phase velocity was used as the objective function in our optimization approach, which considers all pertinent variables such as velocity, grid size, and time step.

2. Methodology

2.1. FD coefficients through conventional methods

The 1D acoustic wave equation can be expressed as[27]:

$$\frac{1}{M'}\frac{\partial^2 u}{\partial t^2}=\left(\frac{\partial}{\partial x}\left(\frac{1}{\rho}\frac{\partial u}{\partial x}\right)\right)+s(t) \tag{I}$$

where ρ is the density; $s(t)$ is the source field; and M' is the P-wave modulus, given by $M'=\lambda+2\mu=\rho v^2$, where λ and μ are the lame constants, v is the velocity, and is the pressure field.

The $2M^{th}$ order SGFD formula for calculating the first-order derivatives is expressed as:

$$\frac{\partial u}{\partial x}=\frac{1}{\Delta x}\sum_{i=1}^{M}a_i\left(u^0_{i+\frac{1}{2}}-u^0_{i-\frac{1}{2}}\right) \tag{II}$$

where $u_i^j=u\left(x+i\Delta x,t+j\Delta t\right)$; x and t are the spatial and temporal coordinates; Δx and Δt are the grid spacing and time step, respectively; i and j are the spatial and temporal indices, and a_i is the i^{th} FD coefficient.

The second-order FD time derivative is used as:

$$\frac{\partial^2 u}{\partial t^2}=\frac{1}{\Delta t^2}\left(u_0^1-2u_0^0+u_0^{-1}\right) \tag{III}$$

where u_0^0 is the pressure field at the point (x,t); u_0^1 is at the future time step $(x,t+\mathrm{j}\Delta t)$; and u_0^{-1} is at the past time step $(x,t-\mathrm{j}\Delta t)$.

Using this second-order time derivative and the 2M[th] order spatial derivatives, the wave equation is expressed as:

$$\frac{1}{\Delta x^2}\sum_{i=1}^{M}\sum_{j=1}^{M}a_i a_j\left(\left(u_{i+j-1}^0-u_{i-1}^0\right)-\left(u_{-i+j}^0-u_{-i-j+1}^0\right)\right)$$
$$=\frac{1}{v^2\Delta t^2}\left(u_0^1-2u_0^0+u_0^{-1}\right) \quad \text{(IV)}$$

where a_i *and* a_j are the coefficients.

By considering plane wave theory, the wave equation is expressed as:

$$u_i^j=e^{\iota\left(k(x+i\Delta x)-\omega(t+j\Delta t)\right)} \quad \text{(V)}$$

where k is the wavenumber, ω is the angular frequency, and $\iota=\sqrt{-1}$.

Substituting **Equation (V)** into the spatial derivative term **Equation (II)**, the wavenumber is written as:

$$k\approx\frac{2}{\Delta x}\sum_{i=1}^{M}a_i\sin\left(\left(i-\frac{1}{2}\right)k\Delta x\right) \quad \text{(VI)}$$

Using Taylor series expansion, the wavenumber is written as:

$$k\approx\frac{2}{\Delta x}\sum_{i=1}^{M}a_i\sum_{j=1}^{\infty}\frac{\sin\left(\left(i-\frac{1}{2}\right)k\Delta x\right)}{(2j-1)!} \quad \text{(VII)}$$

$$\approx\frac{2}{\Delta x}\sum_{i=1}^{M}a_i\sum_{j=1}^{\infty}\frac{(-1)^{j-1}((i-0.5)\Delta x k)^{2j-1}}{(2j-1)!} \quad \text{(VIII)}$$

By comparing the coefficients of on both sides of **Equation (VIII)**, we obtain the SGFD coefficients $a_1, a_2,\ldots a_m$.

2.2. FD coefficients using both time and space domains

Liu and Sen[15] introduced an improved FDM by considering the joint time and space dispersion relation, ensuring better accuracy and stability. This method modifies the FD coefficients to satisfy the exact dispersion relation, thereby reducing errors in wave propagation.

By substituting **Equation (V)** into **Equation (II)**, we obtain:

$$-\frac{4}{\Delta x^2}\sum_{i=1}^{M}a_i\sin\left((i-0.5)k\Delta x\right)\approx-\frac{4}{v^2\Delta t^2}\left[\sin(0.5vk\Delta t)\right]^2 \quad \text{(IX)}$$

Using the sine function expansion, the coefficients for wave equation modeling are derived as:

$$a_i=\frac{(-1)^{i+1}}{2i-1}\prod_{1\le j\le M,\, i\ne j}\left|\frac{(2i-1)^2-(v\Delta t/\Delta x)^2}{(2i-1)^2-(2j-1)^2}\right| \quad \text{(X)}$$

2.3. FD coefficients through the optimization method

To minimize numerical dispersion and enhance accuracy, it is necessary to balance spatial and temporal discretization. Although refining the grid size and reducing the time step can improve accuracy, this significantly increases the computation time. An efficient alternative is to optimize FD coefficients by considering both spatial and temporal dispersion relations. Instead of relying solely on conventional Taylor series expansions, a GA can be employed to fine-tune FD coefficients. This approach reduces dispersion errors while maintaining computational efficiency, without the need for higher-order approximations, smaller grid sizes, or reduced time steps. GA, a global optimization method based on the theory of natural evolution, has been shown in previous studies to produce results that are equal to or better than those of simulated annealing[28] and to provide improved accuracy.[29] GA maintains a population of individuals, from which new generations are created through crossover and mutation operations. As the dispersion relation depends on both space and time, the phase velocity ratio was used as a fitness function for optimization. Over successive generations, the population evolves toward an optimal solution. The workflow for optimization is shown in Figure 1, and the steps for obtaining optimized FD coefficients are described below.

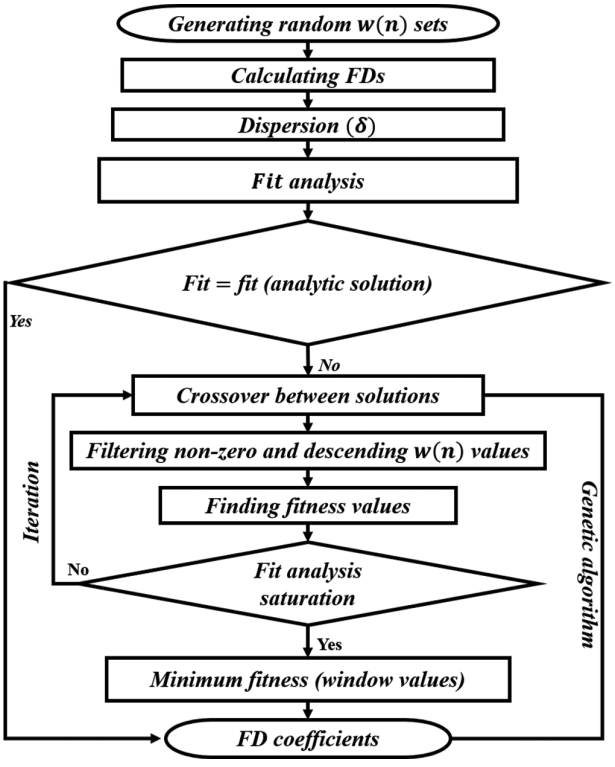

Figure 1. Workflow for optimization of finite-difference (FD) coefficients.

The sinc interpolation was used to derive the FD operator.[16] By applying the window values derived from this method, FD coefficients can be determined using Shannon's sampling theorem[30] as:

$$u(x)=\sum_{n=-\infty}^{\infty}\frac{\sin\frac{\pi}{\Delta x}(x-n\Delta x)}{\frac{\pi}{\Delta x}(x-n\Delta x)}u_n \tag{XI}$$

The first derivative on a staggered grid was evaluated at midpoint $x=\frac{1}{2}\Delta x$, as follows:

$$\frac{\partial u}{\partial x}\Big|_{x=\frac{1}{2}\Delta x}=\frac{1}{\Delta x}\sum_{n=-\infty}^{\infty}\left\{-\frac{1}{\pi}\frac{\sin\left[(\frac{1}{2}-n)\pi\right]}{(\frac{1}{2}-n)^2}\right\}u_n \tag{XII}$$

For a 2M-point SGFD operator approximation, **Equation (XII)** becomes:

$$\frac{\partial u}{\partial x}\Big|_{x=\frac{1}{2}\Delta x}=\frac{1}{\Delta x}\sum_{n=1-M}^{M}w_n^M\left\{-\frac{1}{\pi}\frac{sin\left[(\frac{1}{2}-n)\pi\right]}{(\frac{1}{2}-n)^2}\right\}u_n \tag{XIII}$$

where w_n^M are the window values.

The SGFD coefficients (a_n) were then determined from **Equation (XIII)** as:

$$a_n=-\frac{1}{\pi}\frac{\sin\left[\left(\frac{1}{2}-n\right)\pi\right]}{\left(\frac{1}{2}-n\right)^2}w_n^M,\qquad n=1-M,2-M,\ldots,M \tag{XIV}$$

In the optimization process, an initial population comprising numerous sets of random M window values is generated for the 2N-order approximation, within the range of 0–1. Any number of initial sets can be considered; in this study, around 100 sets were used to ensure that the algorithm performs a global search. The FD coefficients are then computed using **Equation (XIV)**. The phase velocity ratio (or dispersion relation) was used as the fitness function in GA.

The phase velocity ratio was calculated by substituting **Equation (V)** in **Equation (IV)**, expressed as:

$$\delta=\frac{2}{rk\Delta x}\sin^{-1}\left(r\sum_{m=1}^{M}a_m\sin\left[\left(\frac{2m-1}{2}\right)k\Delta x\right]\right) \tag{XV}$$

where $r=\frac{v\Delta t}{\Delta x}$.

During each iteration process, crossover and mutation operations are applied to generate child populations of window values that better fit the fitness function. A weighted function was incorporated into the fitness function to minimize errors more effectively at low wavenumbers, as described by Vanga *et al.*[4] The final fitness function is given by:

$$fit=w_1 err_{mean}+w_2 err_{std} \tag{XVI}$$

where w_1 and w_2 are the weights assigned to the mean error (err_{mean}) and the standard deviation of the error (err_{std}), respectively, with the condition $w_1+w_2=1$. The mean error was calculated as:

$$err_{mean}=\frac{1}{\sum_{i=1}^{K}wg(i)}\sum_{i=1}^{K}wg(i)|1-\delta_i|$$

Where $wg(i)$ is the weighting function over K samples, K is the total number of wavenumber indices.

The standard deviation of the error is calculated as:

$$err_{std}=\sqrt{\frac{\sum_{i=1}^{K}[err(i)-err_{mean}]^2}{K}}$$

where $err(i)=|(1-\delta_i)|$ is the absolute error of the phase velocity ratio.

The weights w_1 and w_2 are user-defined parameters that determine the contribution of each error component to the final fitness value. In this study, different weighting functions were tested to identify the most suitable configuration.

3. Results

We tested linear, exponential, and cubic weighting functions by varying the weights used to calculate the mean dispersion error and standard deviation. After conducting several trials and evaluating the results, the linear weighting function $wg(i)=(k_{max}-i+1)$ was found to provide the best outcomes.[4] Based on this finding, we finalized the weight values as $w_1=0.8$ and $w_2=0.2$, which yielded optimal performance. These values are used in all subsequent numerical examples. We computed the FD coefficients derived using the GA and compared the resulting dispersion curves (phase velocity ratios), as shown in Figure 2, with those obtained using conventional and time-space Taylor series-derived FD coefficients.[15] These GA-derived solutions provide broader kh coverage and show minimal frontal (time) dispersion, as the coefficients are optimized considering both space and time domains.

The proposed method achieves the accuracy of higher-order conventional and time-space methods even at lower orders (e.g., the proposed 8th-order method is equivalent to the 16th-order time-space and the 12th-order conventional method, as shown in Figure 2). The grid spacing is 10 m, the time step is 1 ms, and the wave propagation velocity is 2.5 km/s.

We also compared the results with the previously proposed GA-based explicit FD method,[4] as shown in Figure 3, which shows improved performance when using the staggered grid FDM over the explicit FDM.

To examine how dispersion varies with velocity for three different methods, we calculated phase velocity ratios (Figure 4) for wave velocities of 1.5 km/s (Figure 4A), 2.5 km/s (Figure 4B), and 4.5 km/s (Figure 4C), using 4th, 8th, 12th, and 16th orders of approximation. As shown in Figure 4, it is observed that the new method produces significantly less dispersion compared to the conventional and time-space methods across all approximation orders and velocity settings.

Figure 5 shows the dispersion curves for different velocities using a 12th-order approximation for the conventional method (Figure 5A), the time-space method (Figure 5B), and the proposed method (Figure 5C). As shown in Figure 5A, it is clearly observed that, with increasing velocity, the conventional method exhibits high dispersion in both temporal and spatial components. In the case of the time-space method, temporal dispersion is eliminated; however, spatial dispersion remains significantly high at larger *kh* values compared to the proposed method.

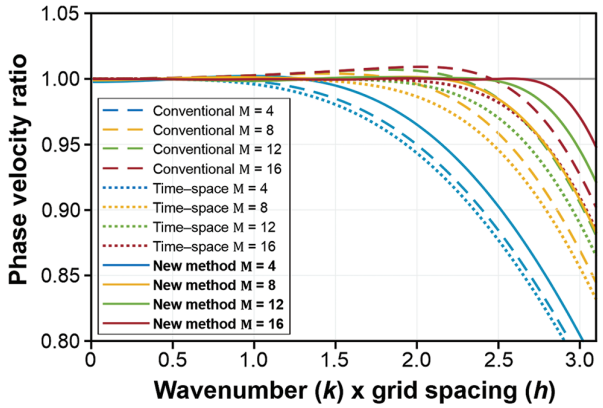

Figure 2. Plot of phase velocity ratio (dispersion) versus the product of the wavenumber (*k*) and grid spacing (*h*) for conventional, time-space and new genetic algorithm-based staggered grid methods, across various orders (M) of approximations.

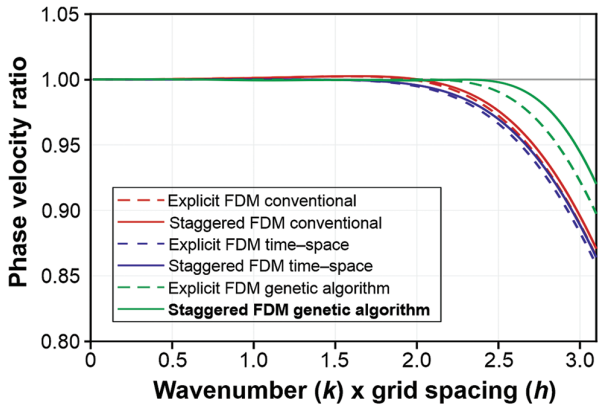

Figure 3. Dispersion curves versus *kh* for conventional, time-space, and new genetic algorithm (GA)-based staggered grid finite-difference methods (FDM) compared with the GA-based explicit FDM for a 12th-order approximation.

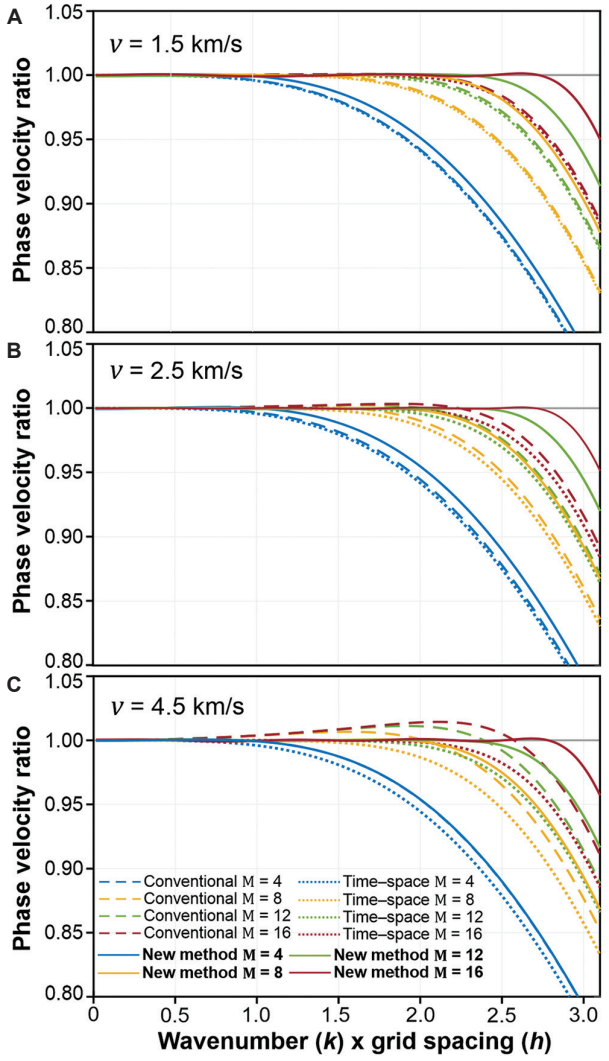

Figure 4. Dispersion versus the *kh* for different velocities *v*: (A) 1.5 km/s, (B) 2.5 km/s, and (C) 4.5 km/s, for various order sof approximations *M*, using conventional, time-space, and new genetic algorithm-based staggered grid methods. The grid spacing is 15 m, and time step is 1 ms.

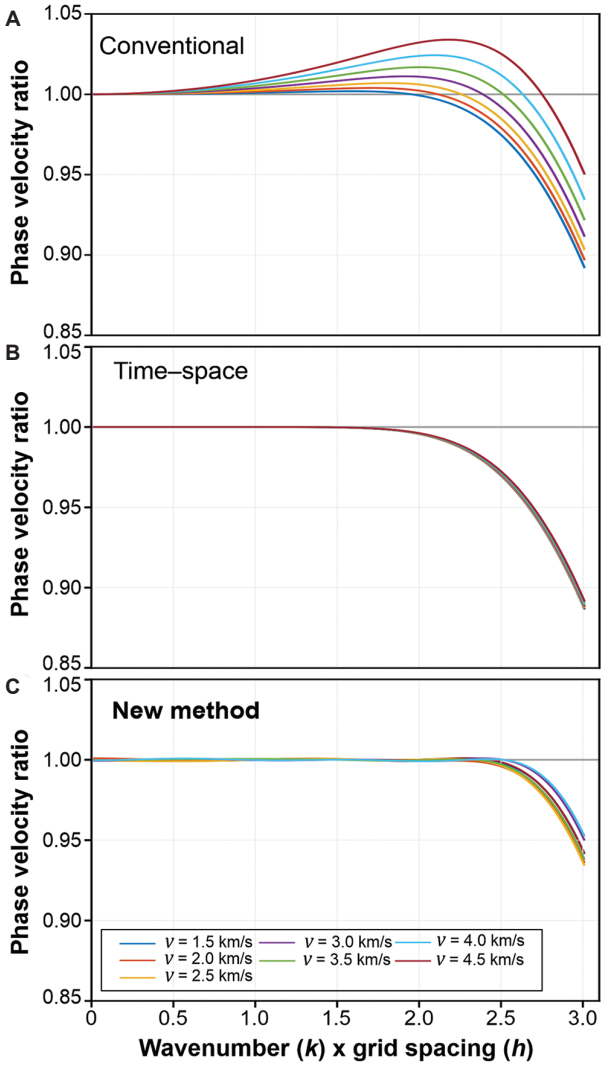

Figure 5. Dispersion versus *kh* for varying velocities *v*, using a 12th-order approximation for: (A) conventional, (B) time-space, and (C) new genetic algorithm-based staggered grid methods. Grid spacing is 10 m, and time step is 1 ms.

Although the time-space method exhibits stable dispersion behavior, it has limited wavenumber coverage. In contrast, the proposed method demonstrates greater stability and broader wavenumber coverage than both the conventional and time-space methods. The stability ratio (*s*) was calculated using the conventional eigenvalue method of stability analysis[15]:

$$s = \left(\sum_{m=1}^{M} a_m \right)^{-1}$$

Figure 6 shows the stability ratio as a function of increasing approximation order for the conventional, time-space, and proposed methods, using a velocity of 2.5 km/s,

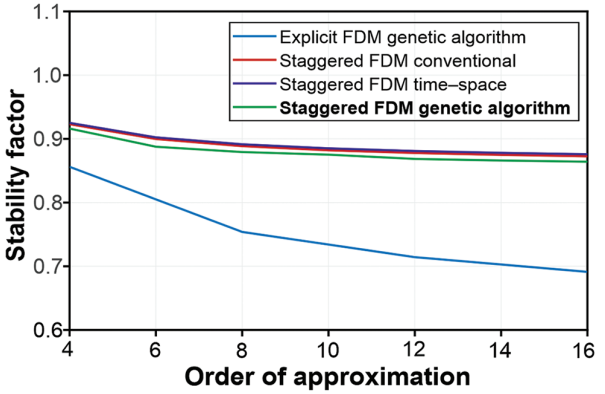

Figure 6. Comparison of stability conditions for the proposed genetic algorithm (GA)-based staggered grid finite-difference method (FDM; green) with the GA-based explicit FDM (blue), conventional staggered grid FDM (red), and time-space staggered grid FDM (purple).

a time step of 1 ms, and a grid spacing of 15 m. It is also evident that the staggered FDM offers greater stability than the explicit FDM. SGFD methods are less constrained by Courant number limitations, which allows for the use of larger time steps without compromising stability. This, in turn, significantly reduces computation time.

3.1. Numerical examples of 2D wave propagation

For the 2D wave simulation, we consider three models: (i) a single velocity medium with 2.5 km/s, (ii) a horizontal-layered model, and (iii) the 2004 British Petroleum (BP) benchmark salt-dome model. We compared 2D wave propagation results at different simulation times using the conventional and time-space method for 4th, 8th, and 12th-order approximations. A 40th-order conventional method was used as the reference solution. Figure 7 presents 2D wave propagation snapshots for the single-velocity medium. Quarter I shows the reference solution using the 40th-order conventional method; quarter II displays results from the GA-based method; quarter III shows the conventional method; and quarter IV is the time-space method. Snapshots were taken at 0.5 s (top panel) and 1.15 s (bottom panel). The wavefields were generated in a single velocity (2.5 km/s) medium measuring 3 km × 3 km, using a grid spacing of 15 m, a time step 1 ms, and a 30 Hz Ricker wavelet as the source. The results show that the proposed GA-based method exhibits significantly lower dispersion across all snapshot times compared to other SGFD methods.

Figure 8 shows the horizontal-layered model (Figure 8A) and the 2004 BP benchmark salt-dome model[31] (Figure 8B), both used to generate synthetic shot gathers. To reduce computational cost, we used staggered FD coefficients optimized for the minimum velocity in each

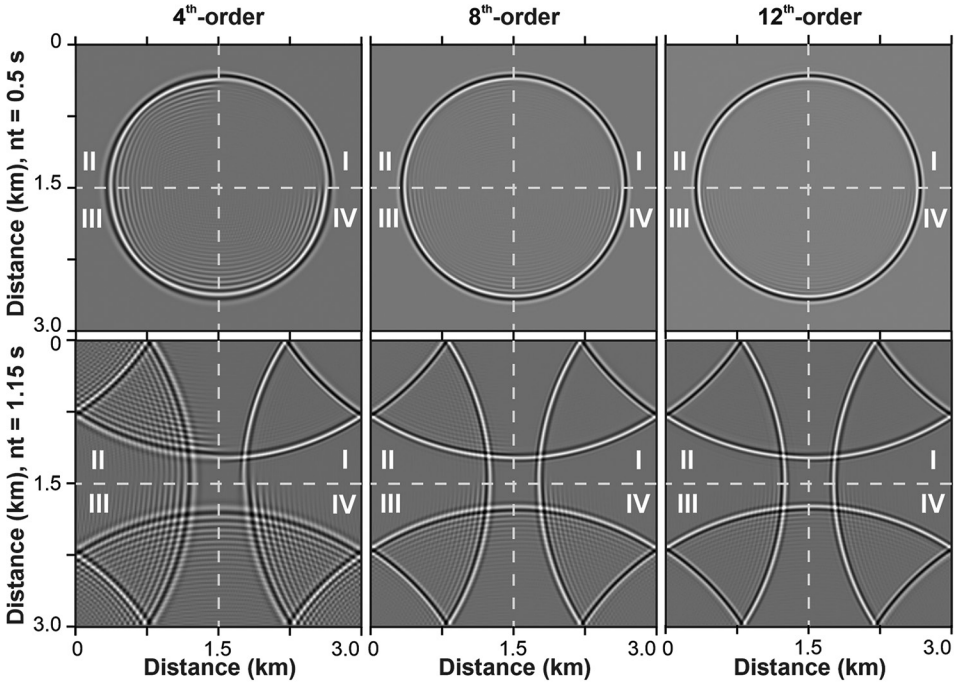

Figure 7. Snapshots of 2D wave propagation in a homogeneous model for 4th, 8th, and 12th orders. Quarter I shows the reference wavefield generated using the 40th-order conventional method; quarter II is the new genetic algorithm-based method; quarter III is the time-space method; and quarter IV is the conventional method.

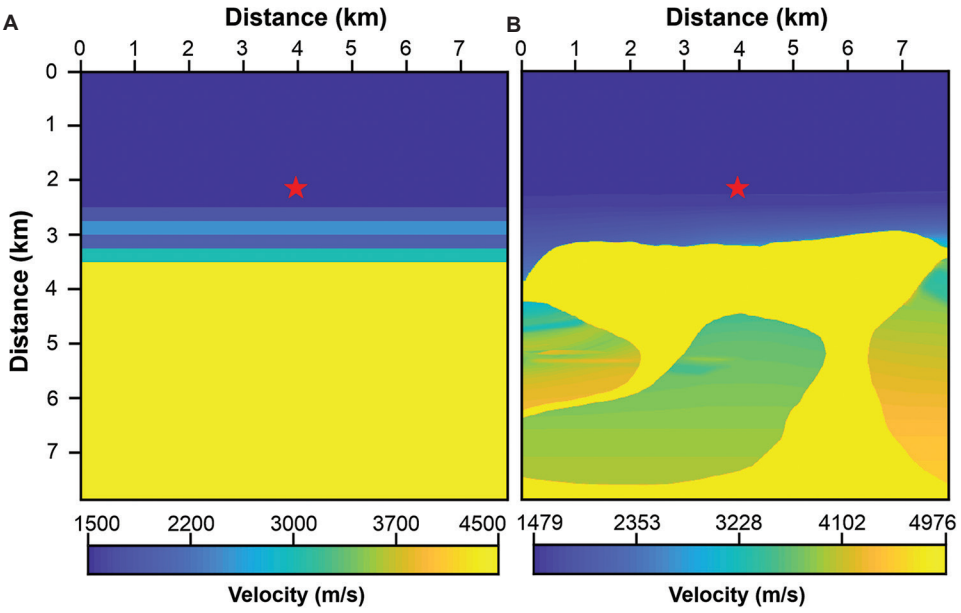

Figure 8. Velocity models used in the study: (A) the horizontal-layered model, and (B) the 2004 BP benchmark salt-dome model. Red stars indicate the source positions.

model. Given that lower velocities (i.e., higher kh) are more dispersive and exhibit reduced wavenumber (k) coverage compared to higher velocities, coefficients optimized for the lowest velocity in the model can be applied effectively across the full velocity range. However, if the velocity range in the model is very broad, coefficients may need to be optimized for different velocity zones to achieve better accuracy. The values of the optimized coefficients for a

Table 1. Optimized finite-difference coefficients for 12th-order approximation

Velocity (m/s)	Coefficient 1	Coefficient 2	Coefficient 3	Coefficient 4	Coefficient 5	Coefficient 6
1,500	1.24712819	−0.11964252	0.03317386	−0.01119058	0.00340783	−0.00058573
2,000	1.23966780	−0.11480708	0.03063733	−0.00987106	0.00270170	−0.00024662
2,500	1.23345081	−0.11135320	0.02889657	−0.00883066	0.00214908	−0.00018497
3,000	1.23220741	−0.11342553	0.03262676	−0.01146971	0.00397580	−0.00101733
3,500	1.21853003	−0.10458359	0.02795159	−0.00870379	0.00224119	−0.00036994
4,000	1.21355644	−0.10444543	0.03043838	−0.01101295	0.00394510	−0.00101733
4,500	1.19863567	−0.09518902	0.02546479	−0.00804402	0.00217978	−0.00033911

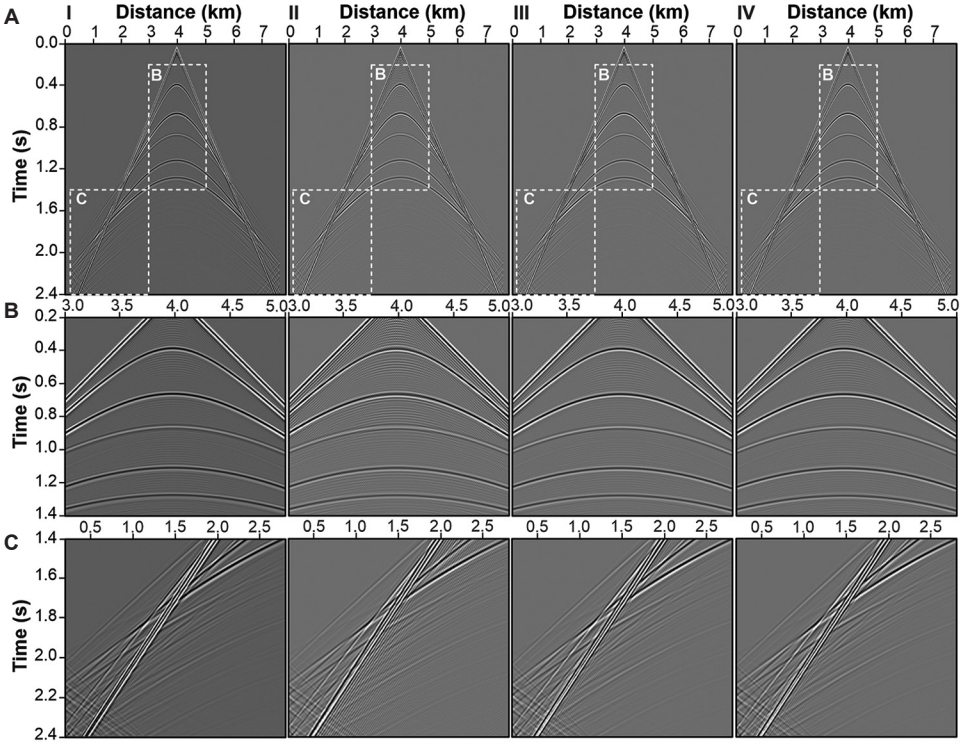

Figure 9. Shot gathers (A) for the horizontal-layered model (Figure 8A). (I) Reference gather generated using the 40th-order conventional method, (II) 12th-order conventional method, (III) new genetic algorithm (GA)-based method with finite-difference (FD) coefficients optimized for the lowest velocity in the model, and (IV) new GA-based method with varying FD coefficients optimized across a range of velocities. Zoomed-in views of the dashed white boxes (B and C) inside Figure A are shown below the corresponding gathers.

12th-order approximation, using a grid size of 10 m and a time step of 1 ms, are provided in Table 1.

Figure 9 shows the shot gathers computed using the horizontal-layered model (Figure 8A) and Figure 10 shows the shot gathers generated from the BP 2004 benchmark salt-dome model (Figure 8B). The horizontal-layered model was used to interpret wave propagation without diffraction effects. The source was placed at x = 3990 m and z = 2250 m. We employed the first derivative of the staggered scheme to discretize the wave equation and used a time step Δt = 1 *ms* and grid spacing Δx = 10 m. Shot gathers were computed using both the conventional and GA-based methods. The gather generated using the 40th-order conventional method is considered the reference (Figures 9I and 10I). Figures 9(II) and 10(II) show the results for the 12th-order conventional method. Figures 9(III) and 10(III) present the new GA-based method using FD coefficients optimized with the lowest velocity in the model, while Figures 9(IV) and 10(IV) show the new GA-based method using FD coefficients optimized over a range of velocities. Compared to the conventional method, the GA-based optimized method yielded improved results with reduced dispersion and lower computational cost by using a lower-order expansion

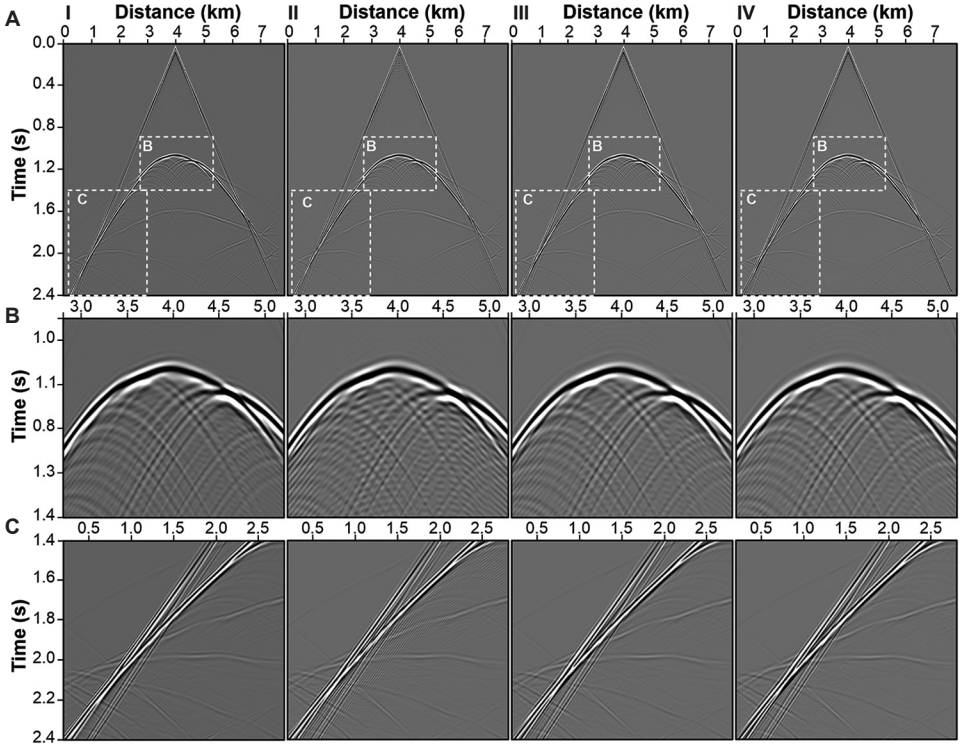

Figure 10. Shot gather (A) for the BP salt-dome model (Figure 8B). (I) Reference gather generated using the 40th-order conventional method, (II) 12th-order conventional method, (III) new genetic algorithm (GA)-based using finite-difference (FD) coefficients optimized for the lowest velocity in the model, and (IV) new GA-based method using varying FD coefficients optimized for a range of velocities. Zoomed-in views of the dashed white boxes (B, C) inside Figure A are shown below the corresponding gathers.

with optimized coefficients. Two optimization approaches were considered: Figures 9(III) and 10(III) show that FD coefficients were optimized using the lowest velocity in the model, while Figures 9(IV) and 10(IV) show that FD coefficients were optimized across a range of velocities. Specifically, SGFD coefficients were optimized at intervals of every 500 m/s. Figures 9(III) and 10(III) good balance between computational efficiency and accuracy, making it suitable for applications requiring broad adaptability across varying velocities. In contrast, as shown in Figures 9(IV) and 10(IV), though slightly more computationally intensive, provide enhanced accuracy in regions with sharp velocity contrasts or complex geological features. This approach is generally more effective in minimizing dispersion errors under varying velocity conditions, thereby improving the reliability of wave propagation simulations in challenging environments.

Numerical modeling using 12th-order approximations of the GA-based, conventional and reference (40th-order conventional) was performed. The simulated results are shown in Figures 11 and 12 for the horizontal-layered and salt-dome velocity models, respectively (Figure 8). Figures 11A and 12A present the reference wavefields generated using the 40th conventional method. Figures 11B and 12B correspond to the 12th-order conventional method. Figures 11C and 12C show results from the proposed SGFD method using FD coefficients optimized for the minimum velocity in the model, while Figures 11D and 12D show the SGFD method using FD coefficients optimized over a range of velocities. In the horizontal-layered model, five interfaces are present, with the third interface being a negative interface. In the bottom panel of Figure 11, the first signal in the seismic traces corresponds to the direct wave; the second to the first interface; the third to the second interface; the fourth to the negative interface; the fifth to the fourth interface; and the sixth to the fifth interface. The 12th-order conventional method shows more dispersion in all reflected signals (including direct and interface reflections), as observed in the seism mic traces beneath the snapshots. As shown in Figures 11 and 12, it is evident that the seismogram produced by the proposed method exhibits significantly less dispersion compared to the conventional method.

4. Discussion

This study focused on modeling seismic wave equations using the SGFD approach combined with GA optimization. The primary goals of seismic wave simulation are to reduce numerical dispersion, improve accuracy, and minimize

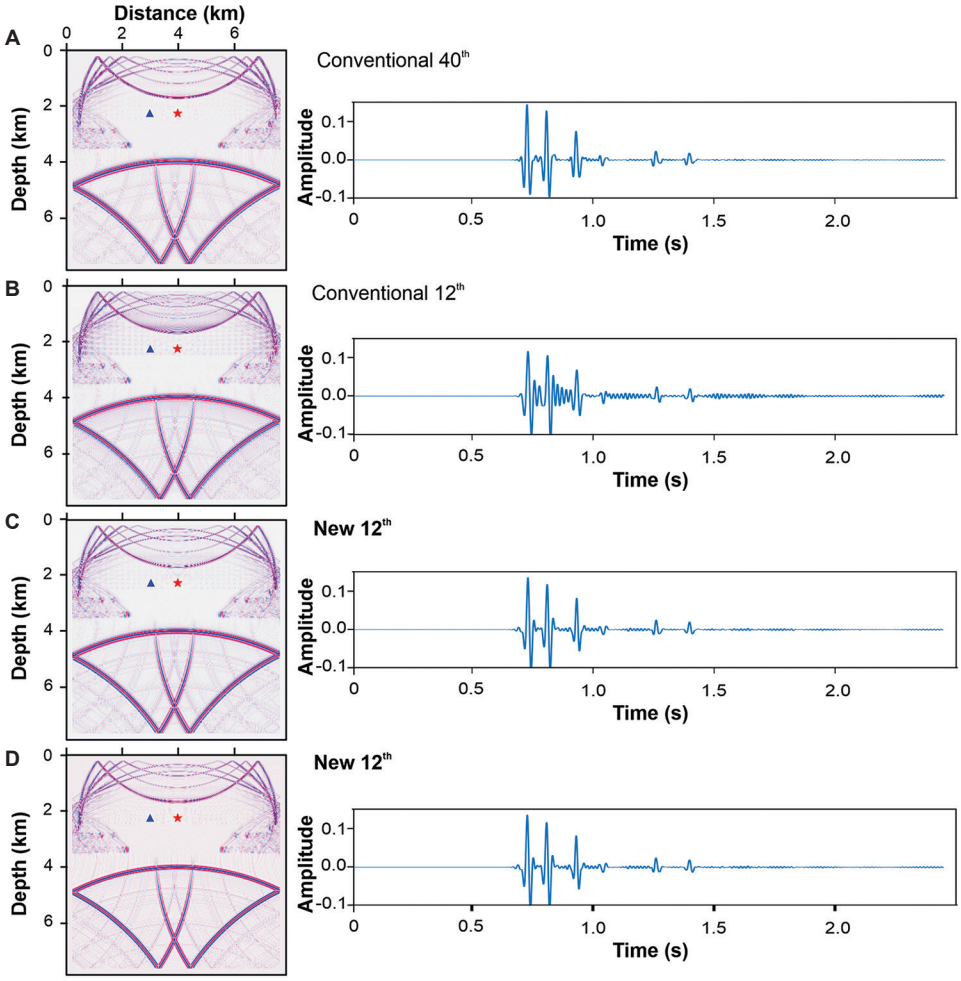

Figure 11. Acoustic wave simulations in the horizontal-layered model (Figure 8A). (A) Reference wavefield generated using the 40th-order conventional method. Wavefields generated using the 12th-order approximation for: (B) conventional and (C) new genetic algorithm (GA)-based method using finite-difference (FD) coefficients optimized for the minimum velocity, and (D) new GA-based staggered grid FD method with varying FD coefficients optimized for a range of velocities. Seismic traces shown below the wavefields correspond to the source (red stars) and receiver (blue triangles) locations.

computational time. The staggered grid approach is preferred over conventional methods due to its inherent interpolation accuracy and stability. GA is employed to improve FD coefficients by considering velocity, grid spacing, and time step, resulting in coefficients that better satisfy both spatial and temporal dispersion relations. Even with lower-order approximations, the study demonstrates that GA-optimized coefficients outperform traditional and time-space Taylor series-derived coefficients by providing broader wavenumber coverage and reduced frontal dispersion.

The computation times for optimizing coefficients over 20 iterations using a standard workstation with 60 Gb RAM are 12.873, 21.390, 21. 993, and 22.064 s for the 4th, 8th, 10th, and 12th orders, respectively. The computational cost of optimizing FD coefficients using GA does not scale linearly with the order of approximation. While higher-order schemes, such as the 12th order, involve more coefficients than lower-order schemes like the 6th order, the increase in computation time is not directly proportional. This is because the solution space expands significantly at higher orders, providing more flexibility for GA to converge efficiently toward an optimal set of coefficients. As a result, although higher-order approximations require more iterations, the search benefits from a larger parameter space, leading to a more gradual increase in computation time rather than linear growth. There is some randomness in the values of each optimized coefficient during the GA process due to its stochastic nature. However, after a sufficient number of iterations, the overall accuracy and wavenumber coverage remain consistent. This ensures that variations in individual coefficients do not significantly affect the modeling outcomes.

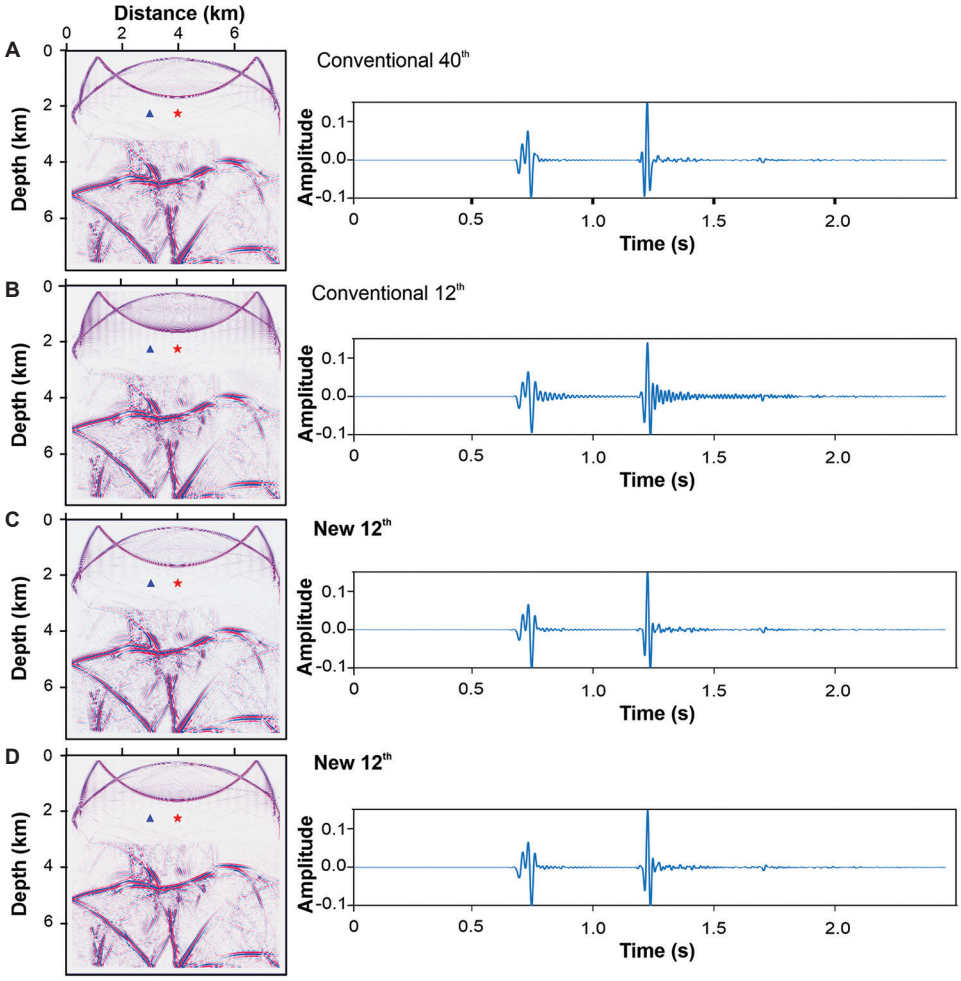

Figure 12. Acoustic wave simulations in the BP salt-dome model (Figure 8B). (A) Reference wavefield generated using the 40th-order conventional method. Wavefields generated using the 12th-order approximation for: (B) conventional, and (C) new genetic algorithm (GA)-based method using finite-difference (FD) coefficients optimized for the minimum velocity, and (D) new GA-based method with varying FD coefficients optimized for a range of velocities. Seismic traces shown below the wavefields were generated using the source and receiver locations indicated by red stars and blue triangles, respectively.

For wavefield simulation, the computation time for both the horizontal-layered and salt-dome model was approximately 110 s, as both models used the same grid size and simulation time (2.4 s). However, when using FD coefficients optimized across a range of velocities, the same simulations take about 130 s due to the additional computation required to apply multiple velocity-dependent stencils. These results show the adaptability of the method to complex structures and highlight how optimized FD coefficients can be reused across a range of velocities within a model. When modeling complex geological structures, velocity variations tend to increase. For such models, FD coefficients optimized across a range of velocities can be precomputed and stored them as stencils for future simulations, providing an efficient and flexible solution.

5. Conclusion

We propose an SGFD method for seismic wavefield simulation, in which the FD coefficients are optimized using a GA. Our results show improved accuracy and reduced numerical dispersion compared to both conventional and time-space methods. Although the computational cost for determining the optimized coefficients is higher than that of conventional methods, this is a 1-time expense. Once the algorithm is run for a set of representative velocities in the model and the optimal coefficients are obtained, the final simulation cost is reduced. This is because the proposed method achieves high accuracy even with lower-order approximations. For example, the eighth-order approximation using the proposed method provides results similar to the 12th-order time-space method (Figure 2), and the 12th-order approximation yields results comparable to

the 40th-order conventional method (Figures 11 and 12). The results presented in this study demonstrate that the optimized SGFD method can be effectively used for seismic wave simulation and may support comparison with real data to obtain more accurate subsurface imaging.

Acknowledgments

The authors gratefully acknowledge the Council of Scientific and Industrial Research—National Geophysical Research Institute (CSIR-NGRI), Hyderabad, for providing academic guidance and research infrastructure. The authors also thank the Academy of Scientific and Innovative Research (AcSIR) for serving as the academic body facilitating the doctoral program and for their continuous support throughout this research.

Funding

This research was supported by the Ministry of Earth Science (MoES), New Delhi (grant number: MoES/OSMART/EFC2021 - OM No. 01(01)/PFC-I/2022).

Conflict of interest

The authors declare that they have no competing interests.

Author contributions

Conceptualization: Mounika Vanga, Maheswar Ojha
Formal analysis: Mounika Vanga
Investigation: Mounika Vanga
Methodology: Mounika Vanga
Software: Mounika Vanga
Writing–original draft: Mounika Vanga
Writing–review & editing: Mounika Vanga, Maheswar Ojha

Availability of data

No data is associated with this theoretical work.

References

1. Kelly KR, Ward RW, Treitel S, Alford R. Synthetic seismograms: A finite -difference approach. *Geophysics*. 1976;41(1):2-27.

   doi: 10.1190/1.1440605.

2. Zhi-Yang W, Hong L, Xiang-De T, Yang W. Optimized finite-difference operator based on chebyshev auto-convolution combined window function. *Chin J Geophys*. 2015;58(2):192-206.

   doi: 10.1002/cjg2.20166

3. Jing H, Yang G, Wang J. An optimized time-space-domain finite difference method with piecewise constant interpolation coefficients for scalar wave propagation. *J Geophys Eng*. 2019L;16(2):309-324.

   doi: 10.1093/jge/gxz008

4. Vanga M, Barman D, Ojha M. An optimized finite difference method to minimize numerical dispersion of acoustic wave propagation using a genetic algorithm. *Geophysics*. 2022;87(3):T265-T279.

   doi: 10.1190/geo2021-0382.1

5. Patera AT. A spectral element method for fluid dynamics: Laminar flow in a channel expansion. *J Comput Phys*. 1984;54(3):468-488.

   doi: 10.1016/0021-9991(84)90128-1

6. Komatitsch D, Vilotte JP. The spectral element method: An efficient tool to simulate the seismic response of 2D and 3D geological structures. *Bull Seismol Soc Am*. 1998;88(2):368-392.

   doi: 10.1785/bssa0880020368

7. Chaljub E, Komatitsch D, Vilotte JP, Capdeville Y, Valette B, Festa G. Spectral-element analysis in seismology. *Adv Geophys*. 2007;48:365-419.

   doi: 10.1016/s0065-2687(06)48007-9

8. Cristini P, Komatitsch D. Some illustrative examples of the use of a spectral-element method in ocean acoustics. *J Acoust Soc Am*. 2012;131(3):EL229-EL235.

   doi: 10.1121/1.3682459

9. Bottero A, Cristini P, Komatitsch D, Asch M. An axisymmetric time-domain spectral-element method for full-wave simulations: Application to ocean acoustics. *J Acoust Soc Am*. 2016;140(5):3520-3530.

   doi: 10.1121/1.4965964

10. Dormy E, Tarantola A. Numerical simulation of elastic wave propagation using a finite volume method. *J Geophys Res Atmos*. 1995;100(B2):2123-2133.

    doi: 10.1029/94jb02648

11. Eymard R, Gallouët T, Herbin R. Finite volume methods. In: *Handbook of Numerical Analysis*. Amsterdam: Elsevier; 2000. p. 713-1018.

    doi: 10.1016/s1570-8659(00)07005-8

12. Komatitsch D, Erlebacher G, Göddeke D, Michéa D. High-order finite-element seismic wave propagation modeling with MPI on a large GPU cluster. *J Comput Phys*. 2010;229(20):7692-7714.

    doi: 10.1016/j.jcp.2010.06.024

13. Igel H, Riollet B, Mora P. *Accuracy of Staggered 3-D finite-Difference Grids for Anisotropic Wave Propagation*. Society of Exploration Geophysicists. 1992. p. 1244-1246.

    doi: 10.1190/1.1821960.

14. Finkelstein B, Kastner R. Finite difference time domain dispersion reduction schemes. *J Comput Phys*. 2006;221(1):422-438.

doi: 10.1016/j.jcp.2006.06.016

15. Liu Y, Sen MK. Scalar wave equation modeling with time-space domain dispersion-relation-based staggered-grid finite-difference schemes. *Bull Seismol Soc Am*. 2011;101(1):141-159.

doi: 10.1785/0120100041

16. Chu C, Stoffa PL. Determination of finite-difference weights using scaled binomial windows. *Geophysics*. 2012;77(3):W17-W26.

doi: 10.1190/geo2011-0336.1

17. Tan S, Huang L. An efficient finite-difference method with high-order accuracy in both time and space domains for modelling scalar-wave propagation. *Geophys J Int*. 2014;197(2):1250-1267.

doi: 10.1093/gji/ggu077

18. Tam CK, Webb JC. Dispersion-Relation-Preserving finite difference schemes for computational acoustics. *J Comput Phys*. 1993;107(2):262-281.

doi: 10.1006/jcph.1993.1142

19. Geller RJ, Takeuchi N. Optimally accurate second-order time-domain finite difference scheme for the elastic equation of motion: One-dimensional case. *Geophys J Int*. 1998;135(1):48-62.

doi: 10.1046/j.1365-246x.1998.00596.x

20. Zhang JH, Yao ZX. Optimized finite-difference operator for broadband seismic wave modeling. *Geophysics*. 2012;78(1):A13-A18.

doi: 10.1190/geo2012-0277.1

21. Zhang JH, Yao ZX. Optimized explicit finite-difference schemes for spatial derivatives using maximum norm. *J Comput Phys*. 2013;250:511-526.

doi: 10.1016/j.jcp.2013.04.029

22. Liu Y. Globally optimal finite-difference schemes based on least squares. *Geophysics*. 2013;78(4):T113-T132.

doi: 10.1190/geo2012-0480.1

23. Liu Y. Optimal staggered-grid finite-difference schemes based on least-squares for wave equation modelling. *Geophys J Int*. 2014;197(2):1033-1047.

doi: 10.1093/gji/ggu032

24. Yang L, Yan H, Liu H. Optimal implicit staggered-grid finite-difference schemes based on the sampling approximation method for seismic modelling. *Geophys Prospect*. 2015;64(3):595-610.

doi: 10.1111/1365-2478.12325

25. Miao Z, Zhang J. Simplified implicit finite-difference method of spatial derivative using explicit schemes with optimized constant coefficients based on L1 norm. *Geophysics*. 2023;89(2):T47-T59.

doi: 10.1190/geo2023-0246.1

26. Peng W, Huang J, Shen Y. Reducing the low-wavenumber dispersion error by building the Lagrange dual problem with a powerful local restriction. *J Geophys Eng*. 2023;20(4):798-815.

doi: 10.1093/jge/gxad047

27. Brekhovskikh, L.M. *Waves in Layered Media*. Vol. 42. New York: Academic Press; 1960. p. 129.

28. Manikas TW, Cain JT. *Genetic Algorithms vs. Simulated Annealing: A Comparison of Approaches for Solving the Circuit Partitioning Problem*; 1996. Available from: https://digitalrepository.smu.edu/engineering_compsci_research/1 [Last accessed on 2025 Apr 13].

29. Santos EPD, Xavier CR, Goldfeld P, Dickstein F, Santos RWD. Comparing genetic algorithms and Newton-Like methods for the solution of the history matching problem. In: *Lecture Notes in Computer Science*. Berlin: Springer; 2009. p. 377-386.

doi: 10.1007/978-3-642-01970-8_37

30. Smith, Julius O. *Physical Audio Signal Processing*. California: Stan Ford University: 2010. Available from: https://ci.nii.ac.jp/ncid/bb07079768?l=en [Last accessed on 2025 Apr 13].

31. Billette FJ, Brandsberg-Dahl S. The 2004 BP Velocity Benchmark. In: *67th EAGE Conference and Exhibition*. Bunnik: European Association of Geoscientists and Engineers; 2005.

ACCSCIENCE PUBLISHING

Journal of Seismic Exploration

ARTICLE

An innovative method for computing static corrections using seismic reflection horizons analysis

Youcef LADJADJ[1,2]*, Mohamed Cherif BERGUIG[1], and Said GACI[3]

[1]Laboratory of Geophysics, Department of Geophysics, Faculty of Earth Sciences, Geography and Regional Planning, University of Sciences and Technology Houari Boumediene, Algiers, Algeria

[2]Department of Physics, Faculty of Sciences, Ferhat Abbas University, Sétif, Algeria

[3]Central Directorate Research and Development, Sonatrach, Boumerdès, Algeria

Abstract

Seismic exploration faces significant challenges due to the physical parameters and geometric complexity of near-surface layers, making their modeling essential for accurately calculating static corrections. These corrections are crucial for preserving the image of geological structures represented by seismic reflectors. However, obtaining key physical parameters, such as the replacement velocity of the substrate and the velocities and thicknesses of near-surface layers, remains challenging. This study proposes a novel approach that addresses the issue in an alternative way. The innovative calculation method allows the direct computation of static corrections, relying solely on the structural analysis of seismic horizons in the near-trace section. Notably, this approach does not require prior knowledge of the weathered zone model. The application of this method to both simulated and real reflection seismic data demonstrates its potential and effectiveness. The static corrections derived from this approach significantly improve seismic image quality and eliminate abnormal regional static corrections compared to calibrated refraction static corrections. Furthermore, this method does not require calibration with borehole data, simplifying the process and representing a significant advantage over traditional methods. In summary, this innovative approach provides an effective solution to the challenges of near-surface layer modeling, delivering substantial improvements quantitatively—through time and effort savings, and reduced error—and qualitatively by enhancing data quality, ensuring consistency with geological realities, and enabling more reliable geological interpretations.

Keywords: Static corrections; Weathered zone model; Near-surface layers; Near-surface structures; Near-trace section; Seismic horizons; Frequency decomposition

***Corresponding author:**
Youcef LADJADJ
(youcef.ladjadj@univ-setif.dz)

Citation: LADJADJ Y, BERGUIG MC, GACI S. An innovative method for computing static corrections using seismic reflection horizons analysis. *J Seismic Explor*. 2025;34(2):14-27.
doi: 10.36922/JSE025240016

Received: June 13, 2025

Revised: August 4, 2025

Accepted: August 5, 2025

Published online: August 22, 2025

1. Introduction

In seismic exploration, the heterogeneity and anisotropy associated with velocity variations, along with the geometric and lithological complexity of near-surface layers, significantly influence the arrival times of seismic waves. As a result, these factors affect imaging characteristics such as continuity, coherence, resolution, and particularly the

shape of seismic horizons and the geological information obtained.[1-4]

Computing static corrections is a processing operation that involves aligning the source and receiver points on the same reference plane. This is achieved by filling the gap between the datum plane and the bedrock of low-velocity layers with a replacement velocity close to or equal to that of the consolidated layer.[1,4]

The refraction statics method is the most commonly used approach for determining static corrections in seismic processing centers. It calculates statics by modeling near-surface layers, a process that remains challenging. Existing methods utilize the travel times of refracted waves to generate a model of the weathered zone (WZ) for computing static corrections. However, these refraction statics methods require picking the first arrivals on seismic reflection records, which consumes time and necessitates significant human intervention.[5-9]

Near-surface structures often coexist with low-quality first arrivals, particularly in scenarios involving complex geometries, which complicates the picking process.[10] Constructing accurate surface models requires high-quality first arrivals; however, results from the refraction method based on these data are not always satisfactory. Therefore, calibrating static corrections with borehole information is essential to achieve reliable values.[11] In regions with poor-quality refractors and terrestrial areas with intricate surface features, the correction process is often complicated, making it time-consuming. To tackle these challenges, automatic picking techniques for first arrivals have been developed.[12-16] However, low-quality first arrivals frequently coincide with complex near-surface structures, further complicating the picking procedure.[10,17] In addition, surface conditions and the characteristics of the near-surface layer—such as heterogeneity, anisotropy, discontinuities, geological uplifts, velocity inversions, and variations in interface shape and dip—affect the recorded refraction waves. These factors contribute to the difficulties in modeling the WZ.[1,4]

The challenges faced when using refracted waves from reflection seismic acquisition underscore the limitations of static refraction corrections and raise the question of whether these first arrival waves are truly suitable for modeling the WZ.

In this work, we introduce a novel technique for computing primary static corrections from the travel time of reflected waves, eliminating the need for first arrival picking and the requirement to model the WZ. This technique utilizes near-trace sections to facilitate the rapid and straightforward identification of seismic horizons (reflectors) affected by static anomalies. The potential, performance, and effectiveness of this method are confirmed and validated through its application to simulated data, followed by real seismic data.

It is well established that one of the quality control procedures for static corrections involves verifying the data from seismic sections post-stacking.[11] Using this criterion, the quality control was conducted on seismic profile data measuring 68 km, characterized by clearly variable surface conditions and morphology.

The seismic sections of the profile were processed using two static correction solutions: the proposed technique and the diminishing residual matrices (DRM) refraction statics method.[18] A comparison of the results was then performed on both obtained seismic sections.

This comparison demonstrates that the proposed method significantly reduces the errors associated with the DRM approach. Consequently, the results highlight the advantages of this new technique and provide a comprehensive evaluation of its impact on the interpretation of seismic data.

2. Methodology

Sedimentary basins have generally undergone multiple tectonic phases, significantly altering sedimentation patterns and basin morphology. The impact of tectonic forces on the formation and evolution of geological layers and sedimentary environments highlights the geological deformations from the Paleozoic to the Cenozoic eras.[19-26] Consequently, geological layers did not form simultaneously. These layers have experienced syn-sedimentary deformations, resulting in geological interfaces that are globally uncorrelated and linearly independent of one another. This characteristic serves as a valuable criterion for evaluating the accuracy of the structural image represented by the seismic reflection horizons in the near-trace section.[27] Thus, in a zero-offset seismic section without applied static corrections, it can be observed that all seismic horizons, from top to bottom, are influenced by the same deformation. This deformation manifests as a common curve among the seismic horizon curves in the zero-offset seismic section, corresponding to the total static corrections. Consequently, calculating this common curve provides the requisite static corrections for accurate interpretation.[28]

This study aims to extract this common curve, or common solution, from the seismic horizons selected on the near-trace section. The principle of the method is illustrated on simulated data, corresponding to a geological model with three synthetic horizons, before and after removing the common curve (Figure 1).

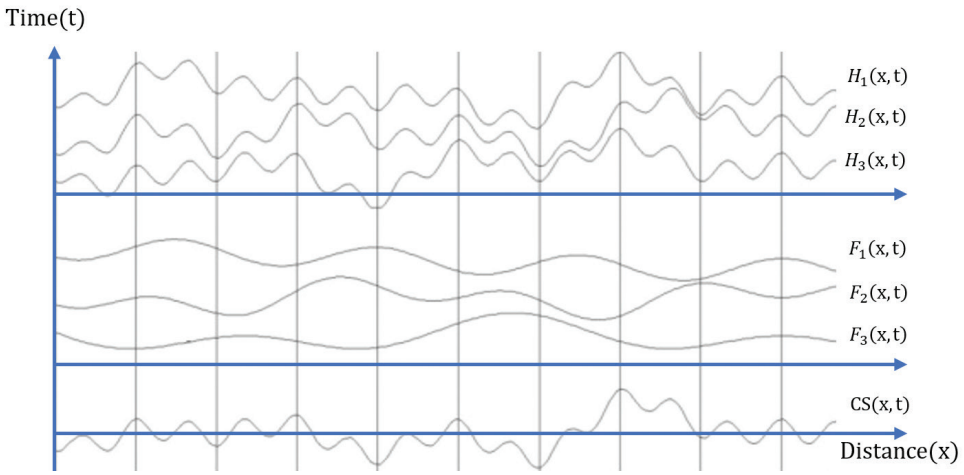

Figure 1. Synthetic model of seismic horizons on the near-trace section, with and without effects of elevation and near-surface layers. Abbreviation: CS: Common solution.

$$\begin{cases} H_1(x,t) = F_1(x,t) + CS(x,t) \\ H_2(x,t) = F_2(x,t) + CS(x,t) \\ H_3(x,t) = F_3(x,t) + CS(x,t) \end{cases} \quad \text{(I)}$$

In **Equation I**, H_1, H_2, and H_3 refer to the horizons before application of static corrections (time geological model), F_1, F_2, and F_3 refer to the horizons after application of static corrections, CS refers to the common solution (static corrections model), and (x, t) is the spatiotemporal localization.

The process applied the Fourier transform to the mathematical functions representing the horizon curves selected on the seismic section of the near-trace section into several frequency classes.[4,27-29] Then, these frequency classes were constructed and used as matrix data to calculate the separation operator matrix and, consequently, the common solution curve, $CS(x, t)$.

The computational procedure employed by the proposed method for calculating static corrections is summarized in Table 1.

Table 1. The algorithm to calculate static correction using seismic reflection horizons

Input	Data input and preprocessing
1	Construction of a near-trace seismic section with no applied static corrections
2	Selection of significant seismic horizons
3	Spectral decomposition of selected horizons
4	Matrix computing
4.1	Construction of a binary matrix, the "separation operator," by normalizing and stacking all the frequency classes
4.2	Obtaining the common matrix through outer multiplication of the separation operator with each decomposed horizon
4.3	The common curve is the stacking of all columns of the common matrix
4.4	The total statics curve is obtained by averaging stacks of all common curves
End	Separation of source and receiver statics

3. Results

3.1. Application to simulated data

To demonstrate the potential of the suggested technique, it was applied to simulated data.[30-33] For this purpose, a four-layer model was constructed and a known static anomaly containing high- and medium-frequency components was introduced. The obtained results are shown in Figures 2 and 3. The separation operator was applied to all the decomposed selected horizons. The obtained curves of the common solutions were consistent and comparable (Figure 3). The average stack of all common solutions was considered to improve the solution accuracy.

The effectiveness of the method was further validated through a comparison of the original (theoretical) static model and the static corrections calculated post-separation. This comparison revealed a negligible discrepancy between the two curves, as illustrated by the error curve (Figure 4). In addition, the successful application of this method on simulated data confirmed its high calculation accuracy, highlighting its reliability and potential for application to real seismic data processing.

3.2. Application to real data

The shape of the time seismic horizons in the near-trace section indicated good geological interfaces deformed by

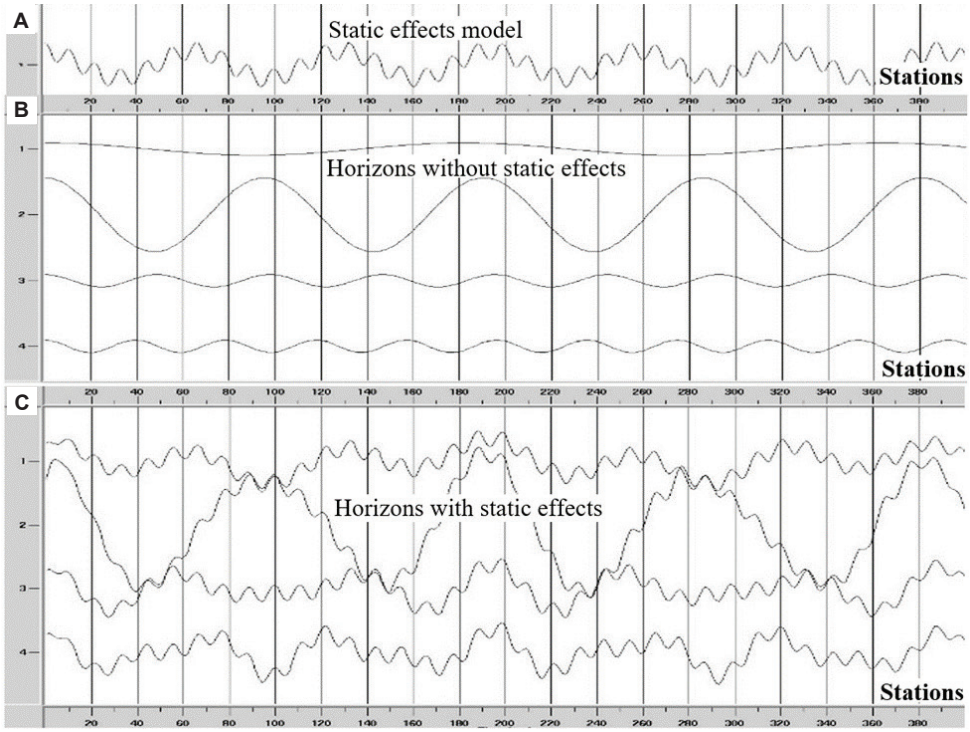

Figure 2. Model of synthetic seismic horizons on near-trace section. (A) Static anomalies model at 15 Hz, summing to 90 Hz. (B) Horizons unaffected by statics at 5 Hz, 10 Hz, 20 Hz, and 25 Hz. (C) Horizons with static effects.

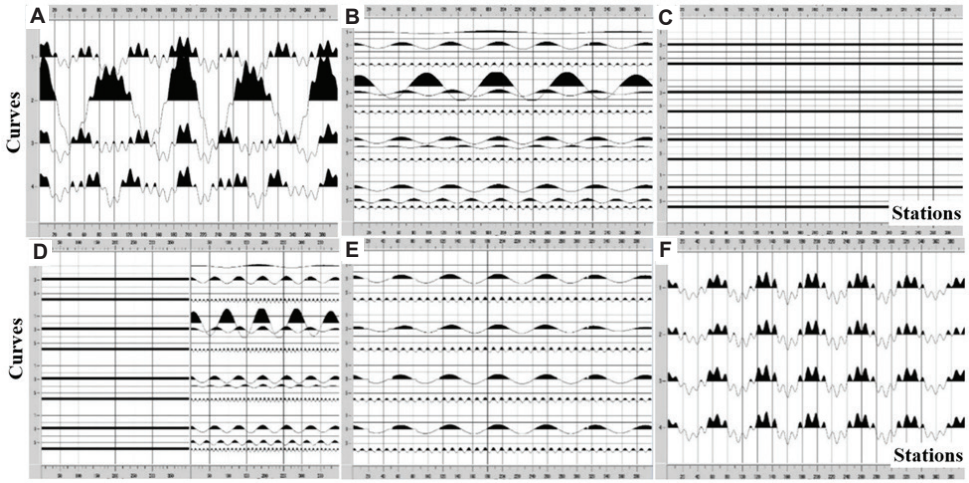

Figure 3. Graphical illustration of the static correction process, showing the decomposed horizons, the separation operator, and the common solution pre-stack and post-stack curves. (A) The geological model is affected by static effects. (B) Decomposed horizons. (C) Separator operator. (D) Operator versus decomposed horizons. (E) Common components. (F) Computed statics model.

the effects of surface elevation and the properties of the near-surface layers (Figure 5). A near-trace seismic section was constructed by selecting the near-offset traces without applying static corrections, using data that had already been preprocessed (Figures 5 and 6). Five seismic horizons were identified and picked from top to bottom (Figure 5).

The common curve was determined based on the spectral decomposition of seismic horizons selected on a near-trace section. The elementary decomposition of each seismic horizon curve was performed within a common frequency band, established through the spectral frequency analysis of all horizon curves.

The curves were converted into traces with an inter-common medium point of 12.5 m, and the sampling rate was set to 2 ms to adapt to the frequency range (0.1–60 Hz) for software processing (Figure 7). High frequencies

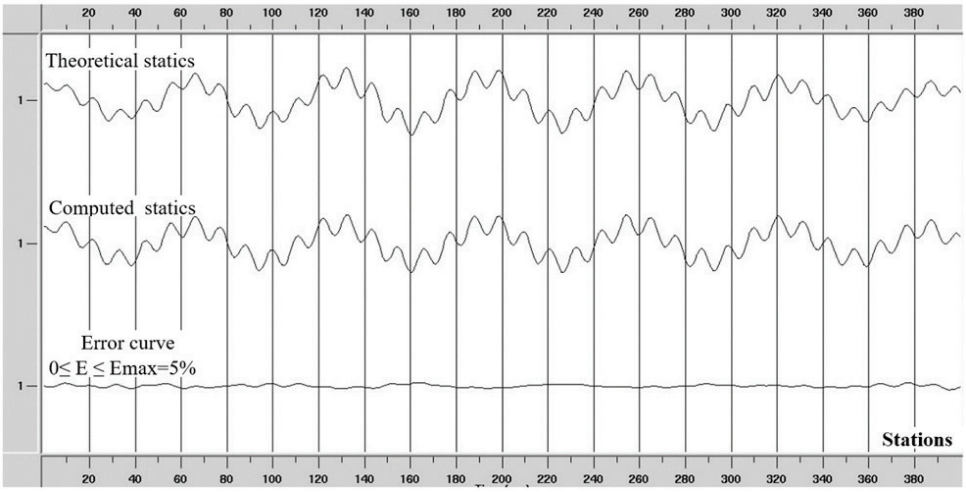

Figure 4. Comparison between the theoretical static model and the computed static corrections. The error curve indicates a maximum deviation of 5% (Emax=5%).

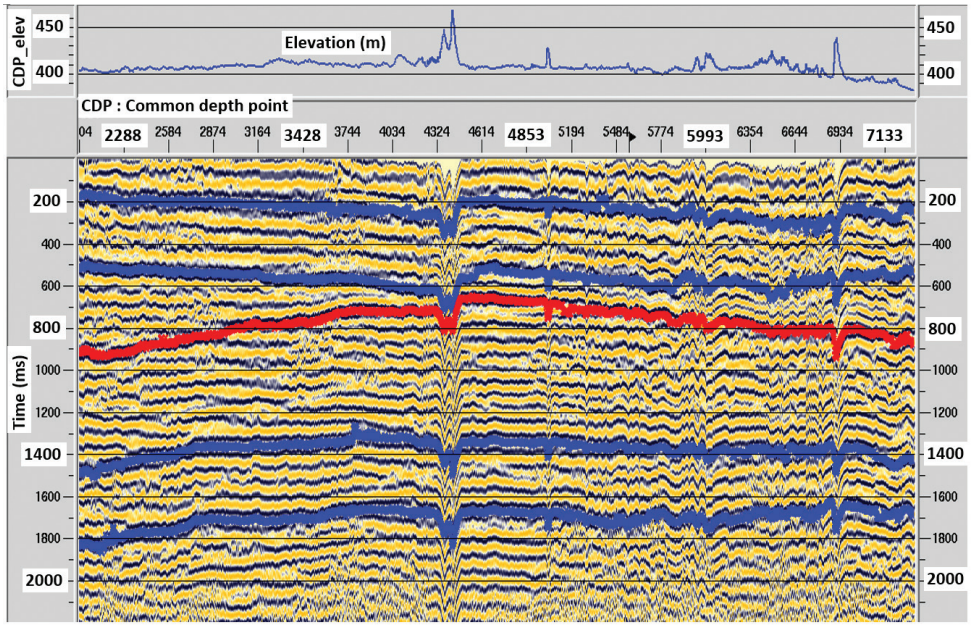

Figure 5. Seismic reflection horizons interpreted on the near-trace section without applying static corrections.

exhibited low amplitudes, which helped determine the maximum frequency limit for effective processing. The frequency analysis of each horizon revealed that high-frequency components have low amplitudes (Figure 7E), aiding in determining the optimal maximum frequency and the overall frequency band for the subsequent elementary frequency decomposition (Figures 7 and 8).

Each curve was decomposed into elementary frequencies and sorted into frequency classes. The selected horizon curves, non-stationary signals, were individually decomposed using the short-time Fourier transform and then categorized into their respective frequency classes (Figure 9).

Each elementary trace was normalized, and a separation operator matrix was constructed. The common curve was then obtained by multiplying the operator matrix by each decomposed horizon matrix. The total statics curve was calculated as the average stack of all resulting curves. The common curve, derived from all horizons, was generated through element-by-element matrix multiplication of the normalized frequency elementary components, followed by summation to produce a common global solution curve (Figure 10).

When applied to all selected horizons, the operator matrix yielded consistent and comparable results with

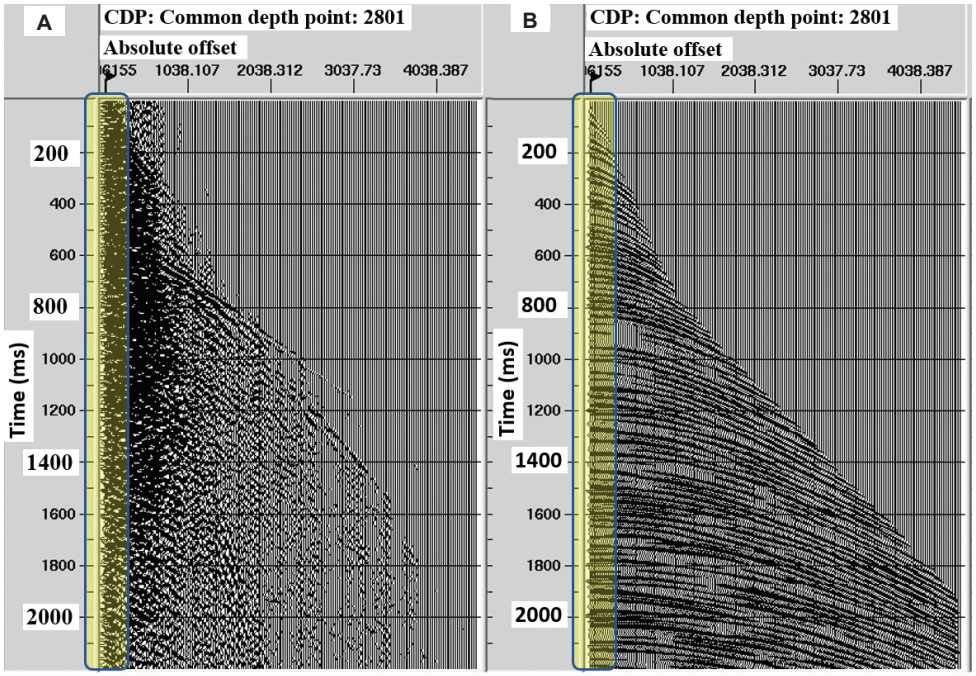

Figure 6. CDP gathers traces. (A) Raw CDP gather traces compared to (B) filtered CDP gather traces, illustrating the enhancement in signal clarity following preprocessing.
Abbreviation: CDP: Common depth point.

acceptable accuracy (Figure 10). To enhance the precision of the total static correction, the average of all common solution curves was computed (Figure 11).

An approximate calculation (**Equations II–IX**) was proposed to separate the source and receiver static corrections from the total static corrections using the elevations of the source and receiver to deduce a mean velocity. It considers the difference between source and receiver elevations, as well as the mean elevation of the entire seismic line (Z_{mean} = 400 m in this case) (Figures 12 and 13).

$$\delta_z = Z_r - Z_S \quad \text{(II)}$$

where δ_z is the difference between source and receiver elevations (in m), Z_s is the source elevation (in m), and Z_r is the receiver elevation (in m).

$$Z_m = (Z_S + Z_r)/2 \quad \text{(III)}$$

where $Z_m = Z_{CMP}$, in which Z_m is the mean elevation between the source and the receiver (in m), also referred to as the common midpoint elevation (Z_{CMP}). Z_{CMP} is the elevation of the common medium point between the source and the receiver (in m).

$$V_m = 2\,(Z_m - Z_{mean})/CS_T \quad \text{(IV)}$$

Where V_m is the average velocity between the mean elevation Z_m and the reference elevation Z_{mean}.

$$\delta_T = \delta_z / V_m \quad \text{(V)}$$

where δ_T is the time difference between the source and the receiver static corrections (in s).

$$CS_T = 2\,(Z_m - Z_{mean})/V_m \quad \text{(VI)}$$

where CS_T is the total static correction (in m), and Z_{mean} is the mean elevation of the entire seismic line (400 m).

$$CS_T = CS_S + CS_R \quad \text{(VII)}$$

$$CS_S = (CS_T - \delta_T)/2 \quad \text{(VIII)}$$

$$CS_R = CS_T - CS_S \quad \text{(IX)}$$

Where CS_s is the source static correction, and CS_R is the receiver static correction.

We present a novel technique for computing static corrections directly from the travel times of reflected waves. This approach calculates total static corrections by identifying seismic reflection horizons on the near-trace section. The static corrections for both the source and the receiver are derived from elevation values. To illustrate the effectiveness and efficiency of this method, the results were compared with those obtained from refraction statics based on the DRM method (Figures 14-17).

The suggested technique was applied to a 68-km seismic profile, and the results obtained were compared to those

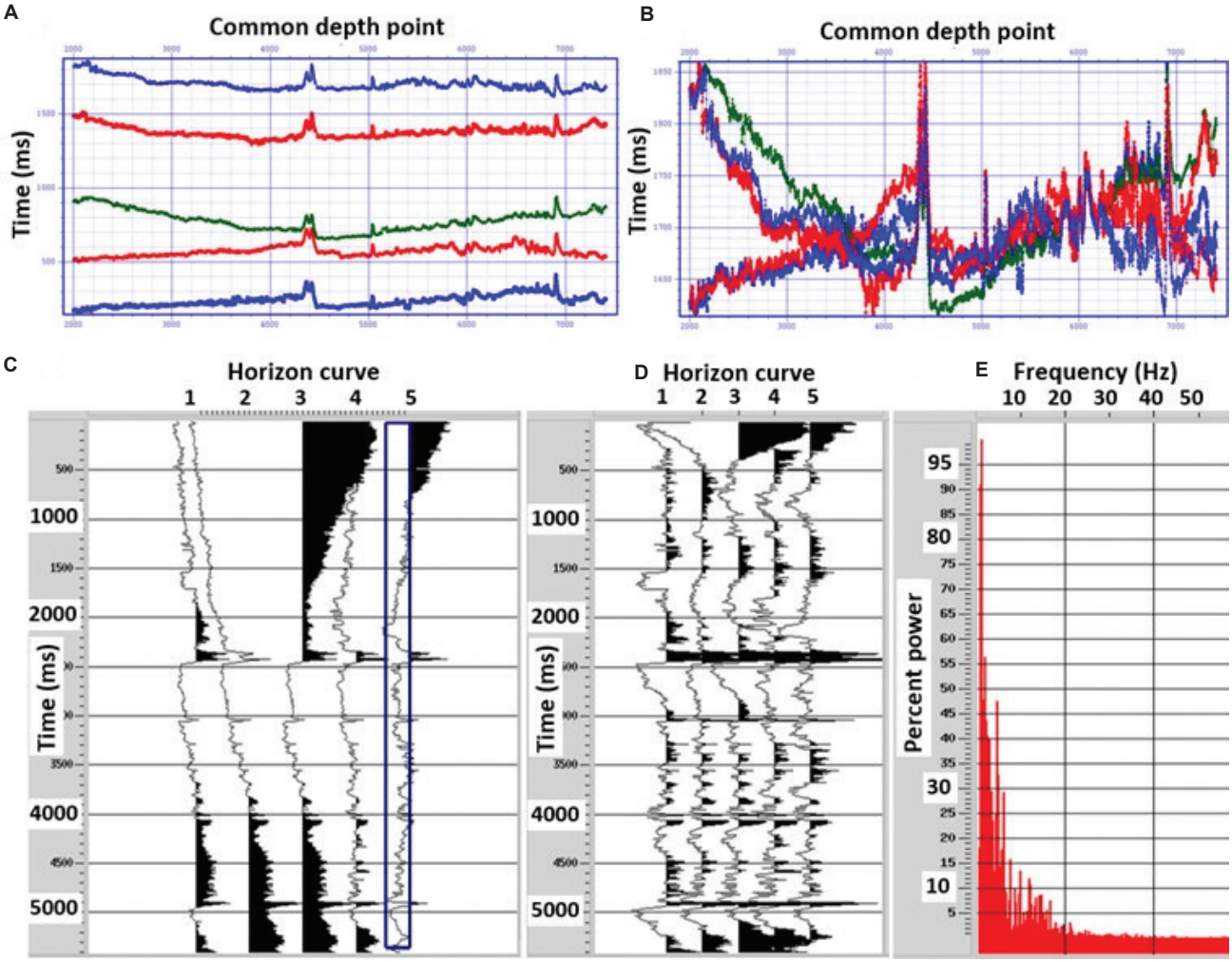

Figure 7. Conversion and processing of horizon curves. (A) Selected horizon curves. (B) Superposition of selected horizon curves. (C) Horizon curves converted into traces. (D) Traces with a common frequency band. (E) Frequency spectrum of all the traces (percent power).

derived using the DRM-based refraction statics method.[18] The refraction statics solution was computed by picking the first arrivals in the offset range of 150–1100 m, using V0=800 m/s and V1=2,400 m/s (Figure 14).

The curves of the refraction static corrections and the proposed corrections displayed a similar global trend; however, notable differences were observed in the regional, medium, and short wavelengths (Figures 14 and 15). The differences in values (10–20 ms) between the static curves from the receivers over distances ranging from 10 km to 20 km (Figure 15) suggest the presence of significant errors that could result in misleading and erroneous structural interpretations, thereby distorting the overall geological interpretation.

This comparison demonstrated that the proposed method significantly reduced the errors associated with the DRM method (Figures 14 and 15). In addition, it enhanced the quality of seismic data and ensured accurate interpretation of geological structures (Figures 16 and 17). Consequently, the results highlighted the advantages of the proposed approach and offered a comprehensive evaluation of its impact on the interpretation of seismic data.

One quality control procedure for static corrections involves checking the data on the seismic section after stacking.[11] The proposed method improved the seismic image and provided more precise and accurate static corrections. The horizons were clearer in the seismic section obtained. In addition, the comparison with calibrated refraction statics revealed significant improvements in seismic imaging and regional static anomalies removal (Figures 16 and 17).

Unlike static corrections derived from refraction methods, which require calibration with borehole data to correct regional trends, the suggested method eliminates the need for such calibration. This improved

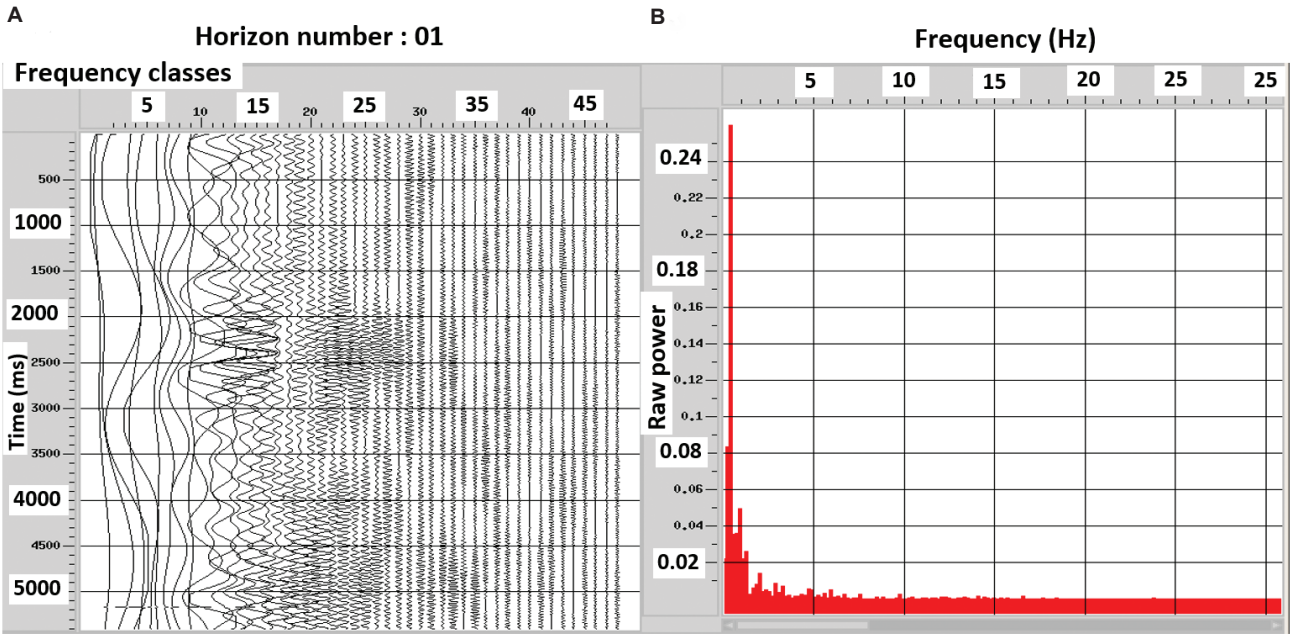

Figure 8. Horizon curve frequency decomposition and amplitude analysis. (A) Elementary frequency decomposition and (B) corresponding frequency spectrum.

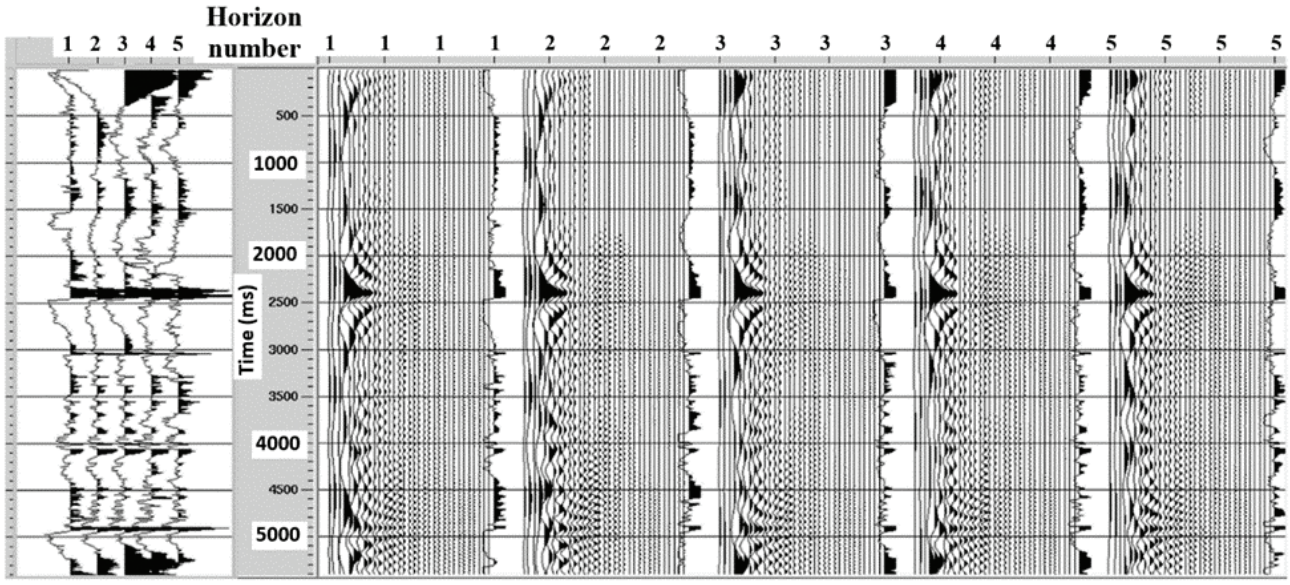

Figure 9. Elementary frequency decomposition of the selected seismic horizons using the short-time Fourier transform.

accuracy enhances continuity, coherence, resolution, and the representation of geological structures, making this approach highly efficient for seismic data processing.

A comparison of the results showed that this method provided more accurate static corrections, significantly reducing errors and enhancing the quality of seismic horizons in terms of continuity, energy, resolution, and signal-to-noise ratio across the entire seismic section (Figures 16 and 17).

4. Discussion

In this study, we proposed an innovative method for calculating static corrections by analyzing horizons in the near-trace section, thereby eliminating the need for prior modeling of the near-surface layers.

The impact of heterogeneity and discontinuous structures near the surface on seismic wave velocity is evident in the variations observed in the travel times

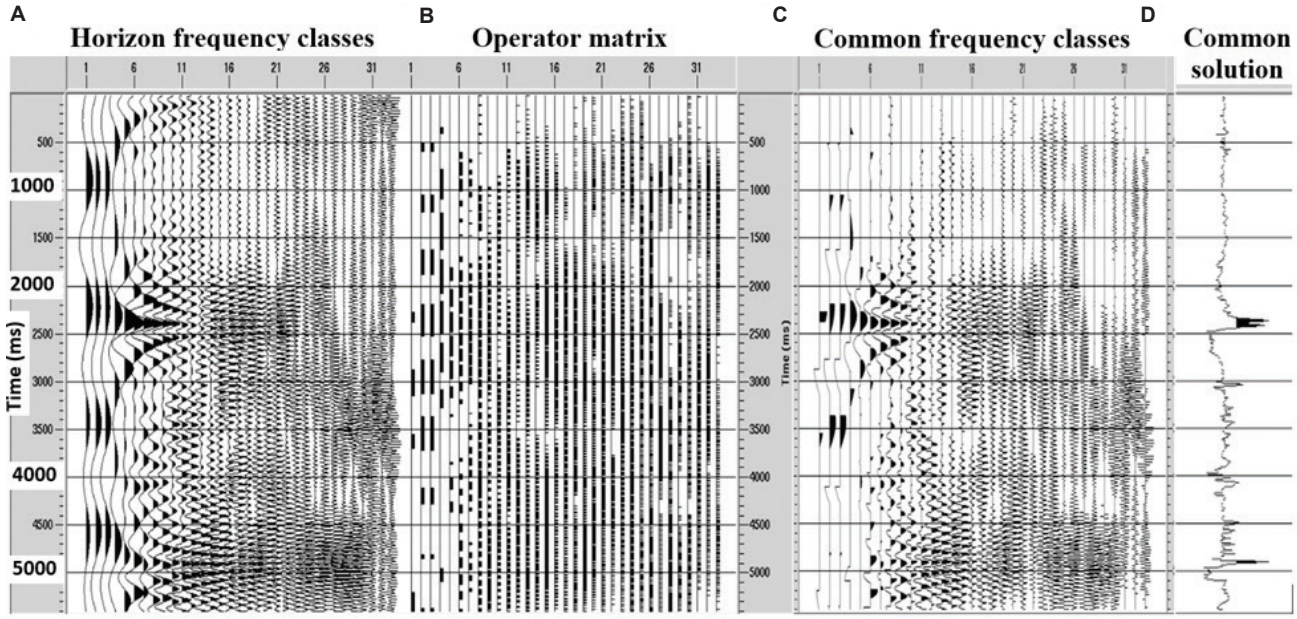

Figure 10. Decomposed horizons matrix, the separation operator matrix, and the common solution pre-stack matrix and post-stack curve. (A) Decomposed horizons. (B) Separation operator. (C) Pre-stack common solution. (D) Common solution curve.

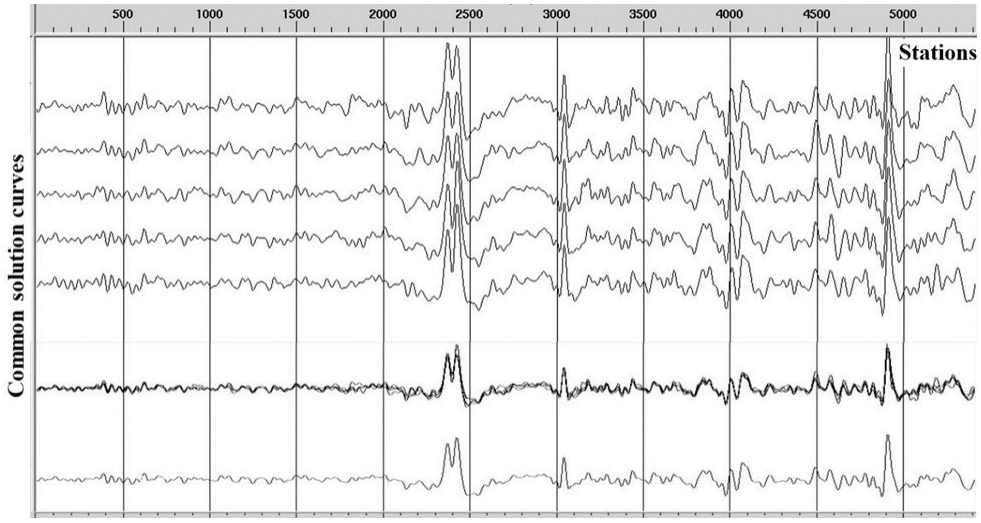

Figure 11. All common solution curves obtained from each reflector (top). Middle: Superposed all common curves. Bottom: Average stack of the common curves (Total static solution).

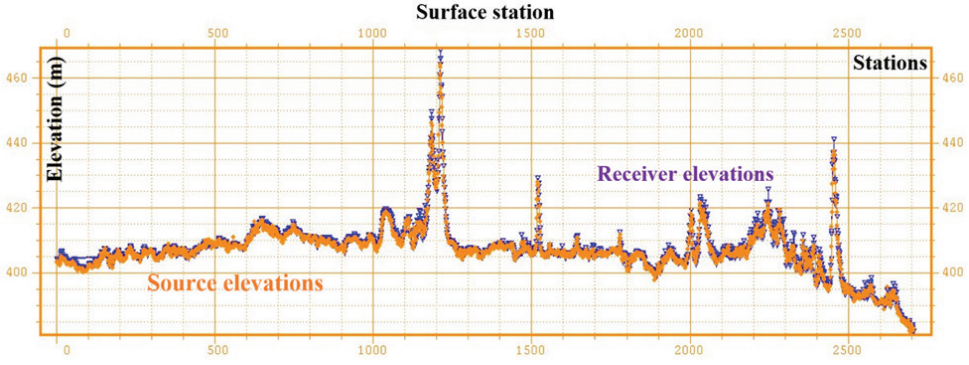

Figure 12. Source elevations (orange) and receiver elevations (blue) along the acquisition line.

of reflected seismic waves. The method is based on accurately identifying these horizons in a zero-offset section (before applying static corrections). The total static correction is derived by extracting the common deformation curve shared among the horizons. However, regardless of the complexity of the near-surface structures, if the seismic horizons cannot be clearly identified after advanced processing and filtering, the method will not be applicable and will be considered a limitation.[34,35] The application of the proposed methodology to simulated data demonstrated its effectiveness, showing excellent agreement with theoretical models and thereby validating the robustness of the technique. This robust performance on simulated datasets provided a solid foundation for its application to real-world seismic data. However, while the results obtained from the real data offered valuable insights, they also revealed certain limitations, particularly under challenging conditions. These observations raise important considerations regarding the method's reliability in less-than-ideal acquisition or geological contexts.

The results obtained from both simulated and real seismic data demonstrated that the proposed approach significantly outperformed traditional methods, particularly refraction statics, in terms of both accuracy and efficiency. When applied to real data, it yielded a notable enhancement in seismic image quality by effectively mitigating regional anomalies typically observed with calibrated static corrections. This improvement is critical for ensuring the continuity and consistency of seismic horizons, which are fundamental for reliable geological interpretation. Compared to calibrated refraction statics, the method produced substantial gains in image clarity, including enhanced structural continuity and resolution. Moreover, eliminating the need for borehole calibration streamlines the processing workflow while delivering clearer and more coherent seismic sections than conventional techniques.

Although the results are promising, it is essential to acknowledge certain limitations of the study. One of the

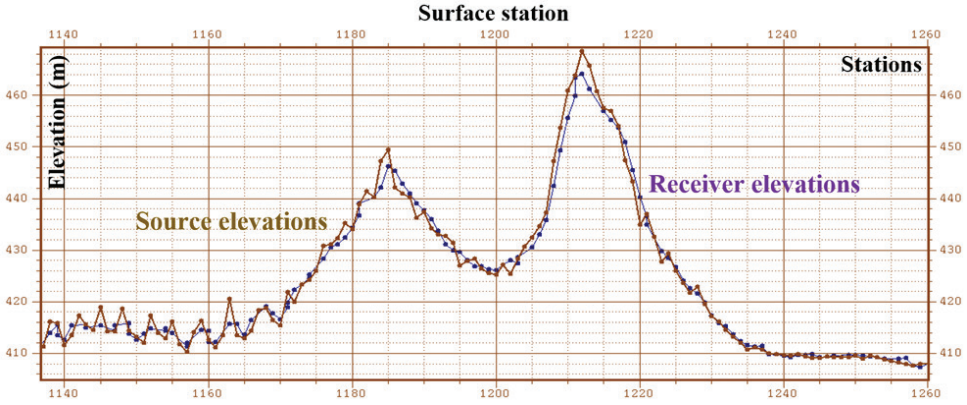

Figure 13. Zoomed-in view of source (brown) and receiver (blue) elevation curves, highlighting elevation variations along the seismic profile.

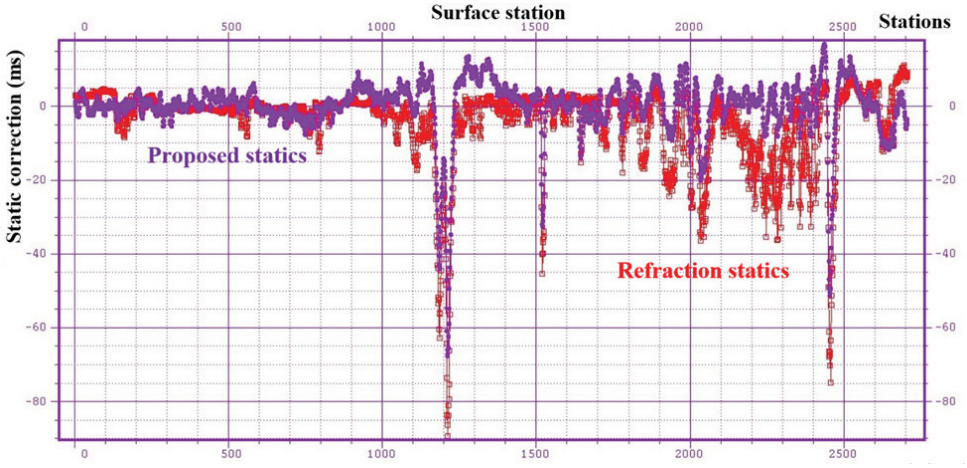

Figure 14. Comparison of static correction curves obtained using the proposed method (purple) and the refraction method (red).

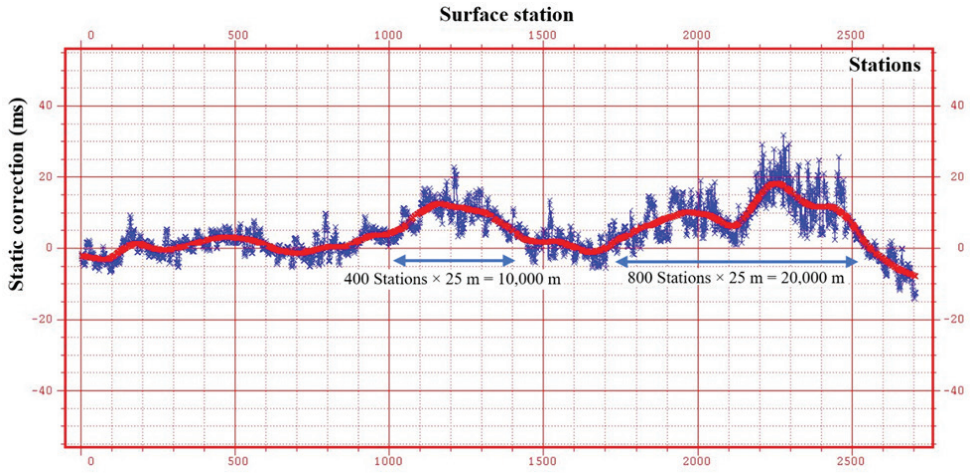

Figure 15. The difference between the static curves obtained from the proposed method and the refraction method, presented with smoothing (red) and without smoothing (blue).

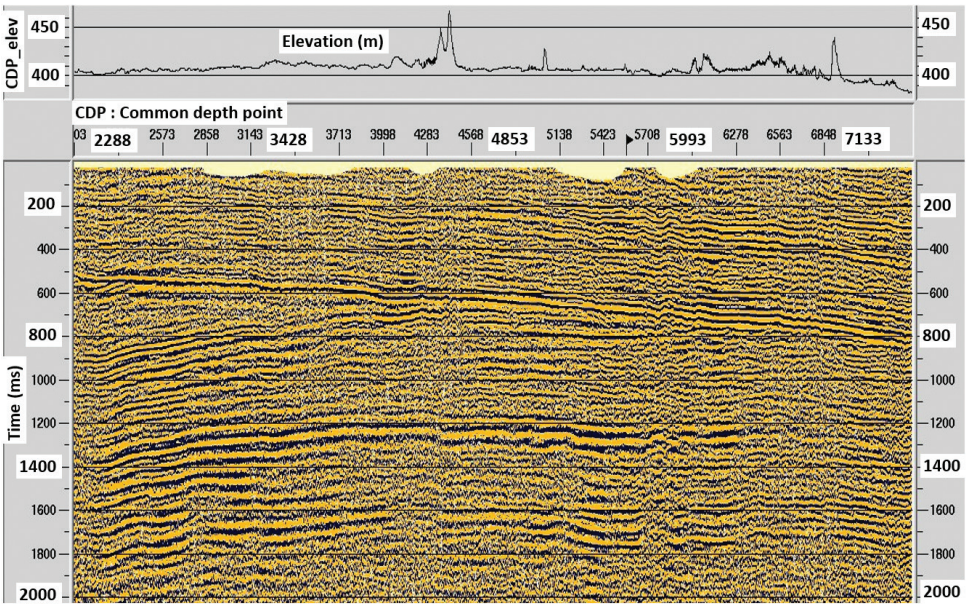

Figure 16. Seismic section processed using refraction static corrections. CDP_elev refers to CDP elevation.
Abbreviation: CDP: Common depth point.

main sources of error lies in the data quality, particularly when the data presents a low signal-to-noise ratio. In such cases, powerful filtering is required to clarify reflected seismic horizons, complicating their analysis and shape tracking.

In summary, this method demonstrated that the proposed method offers an efficient and reliable solution for calculating static corrections in seismic exploration. By simplifying the process and improving the quality of seismic images, it addresses one of the main challenges in seismic exploration: the modeling of complex and heterogeneous near-surface layers. Traditional methods, such as refraction statics, heavily rely on the quality of first arrivals, which can be problematic in challenging geological environments.[10,11,36] The proposed method circumvents the need for first arrival picking and near-surface layers modeling, which are both time-consuming and prone to human error.

Although this study has demonstrated the applicability of our methodology, it is essential to continue refining this approach to maximize the impact of the results in the field. It would be relevant to develop this method to integrate the study and analysis of discontinuous and segmented seismic horizons in the case of sedimentary basins with complex

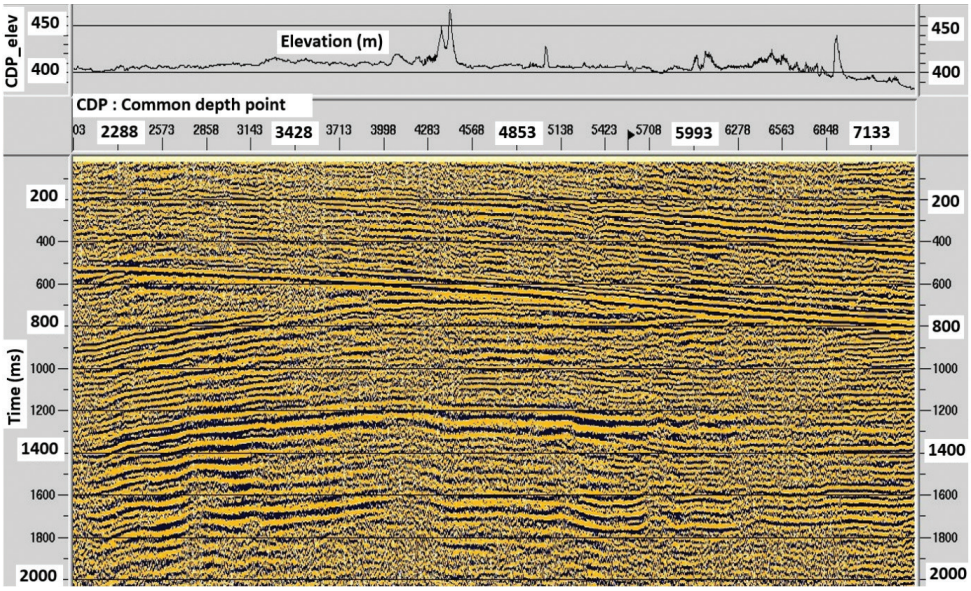

Figure 17. Seismic section processed using the proposed static corrections. CDP_elev refers to CDP elevation.
Abbreviation: CDP: Common depth point.

and rugged geology. Furthermore, it is essential to further develop this method to be suitable for three-dimensional studies. These complementary avenues of research could strengthen the robustness of the method and broaden its scope of application.

5. Conclusion

The innovative method developed for calculating static corrections represents a significant advancement in seismic exploration methodologies. Based on the reality of geological structures, this approach utilized images of seismic horizons to directly estimate total static corrections without relying on prior information from the WZ model. This independence streamlined the correction process and enhanced the reliability of seismic interpretations.

The technique analyzes time seismic horizons (reflectors) selected from the near-trace section. By correcting for variations in surface elevation, the velocities of near-surface layers, and the bedrock (replacement velocity), the method effectively addresses the regional components of static corrections. This analysis prevents the introduction of fictitious structures, ensuring the final seismic images remain true to geological reality.

A comparison of the results showed that this method provides more accurate static corrections, and improves the seismic imaging and the quality of seismic horizons in terms of continuity, coherence, energy, resolution, signal-to-noise ratio, while respecting the reality of geological structures over the entire seismic section, making this approach efficient for seismic data interpretation (Figures 16 and 17).

In addition, utilizing the near-trace section for horizon selection reduces the effort required for first arrival picking. This expedites the process and minimizes human error, resulting in faster execution than conventional methods. This advancement is achieved without needing borehole data surveys, increasing efficiency and accessibility, particularly in challenging terrains.

Overall, the results highlight the advantages of this method in improving seismic imaging and its impact on data interpretation. The proposed static corrections are more reliable than traditional techniques, particularly in complex geological settings.

The methodological advances introduced in this study encompass several key innovations and offer a robust and efficient alternative for computing static corrections in seismic exploration. It overcomes key limitations of traditional techniques. First, directly calculating static corrections eliminates the need for prior knowledge of the WZ model. In addition, the study removes the necessity for picking first arrivals and avoids calibration with borehole data, which reduces human error, simplifies the process, and lowers costs. The method is also independent of complex near-surface structures, effectively addressing discontinuity, heterogeneity, and anisotropy challenges in the near-surface layers. Moreover, it demonstrates efficiency in execution, achieving faster processing times through near-trace sections. Finally, the quality and

reliability of seismic images are enhanced by adhering to the structural geological reality.

Furthermore, this innovative method represents a substantial advancement in seismic exploration, contributing to more reliable and efficient geological assessments.

Acknowledgments

We would like to express our sincere gratitude to Halliburton for providing the SeisSpace software, which greatly contributed to the completion of this study. This software was installed at our university as part of a research and scientific development co-operation agreement.

Funding

None.

Conflict of interest

The authors declare they have no competing interests.

Author contributions

Conceptualization: Youcef LADJADJ
Formal analysis: Youcef LADJADJ
Investigation: Youcef LADJADJ
Methodology: Youcef LADJADJ
Supervision: Mohamed Cherif BERGUIG, Said GACI
Validation: Youcef LADJADJ, Mohamed Cherif BERGUIG, Said GACI
Visualization: Youcef LADJADJ
Writing–original draft: Youcef LADJADJ
Writing–review & editing: Youcef LADJADJ, Mohamed Cherif BERGUIG, Said GACI

Availability of data

All data analyzed have been presented in the paper.

Further disclosure

Part of the findings has been presented in the:
(i) 9th International Symposium on Hydrocarbons and Chemistry (ISHC9) on Jun 25 and 26, 2024, at Boumerdès (Algeria), under the title, "Seismic Reflection Data for Accurate Statics Correction Determination: A Novel Approach."
(ii) Near Surface Modeling and Imaging Workshop (SEG) in Muscat, Oman, from September 27–29, 2022, under the title, "A New Approach for Estimating Accurate Statics Correction."

References

1. Cox M. *Static Corrections for Seismic Reflection Surveys*. Thousand Oaks: SEG Books; 1999.
doi: 10.1190/1.9781560801818
2. Marsden D. Static corrections: A review. Part I. *Geophys Lead Edge*. 1993a;12(1):43-49.
doi: 10.1190/1.1436912
3. Marsden D. Static corrections: A review. Part II. *Lead Edge*. 1993b;12(2):115-120.
doi: 10.1190/1.1436936
4. Yilmaz Ö, Stephen MD. *Seismic Data Analysis: Processing, Inversion, and Interpretation of Seismic Data*. Vol. I. Thousand Oaks: SEG Books; 2001.
5. Gaci S. The use of wavelet-based denoising techniques to enhance the first-arrival picking on seismic traces. *IEEE Trans Geosci Remote Sens*. 2013;52(8):4558-4563.
doi: 10.1109/TGRS.2013.2282422
6. Lei J, Fang H, Zhu Y, *et al*. GPR detection localization of underground structures based on deep learning and reverse time migration. *NDT E Int*. 2024;143:103043.
doi: 10.1016/j.ndteint.2024.103043
7. Li J, Hu Z, Cui J, Lin G. Efficient GPU-accelerated seismic analysis strategy and scenario simulation for large-scale nuclear structure cluster-soil interaction over ten million DOFs. *Comput Geotech*. 2024;174:106583.
doi: 10.1016/j.compgeo.2024.106583
8. Zhou G, Jia G, Zhou X, *et al*. Adaptive high-speed echo data acquisition method for bathymetric LiDAR. *IEEE Trans Geosci Remote Sens*. 2024;62:1-17.
doi: 10.1109/tgrs.2024.3386687
9. Zhou G, Song N, Jia G, *et al*. Adaptive adjustment for laser energy and PMT gain through self-feedback of echo data in bathymetric LiDAR. *IEEE Trans Geosci Remote Sens*. 2024;62:1-22.
doi: 10.1109/TGRS.2024.3403895
10. Tlalka S, Sobocinski R. Modelling for Statics Correction. In: *75th EAGE Conference and Exhibition*, London, UK; 2013. p. 10-13.
11. Tlalka S. *Static Corrections in Challenging Cases*. India: Society of Petroleum Geophysicists; 2010.
12. Boschetti F, Dentith MD, List RD. A fractal-based algorithm for detecting first arrivals on seismic traces. *Geophysics*. 1996;61:1095-1102.
doi: 10.1190/1.1444030
13. Coppens F. First arrival picking on common-offset trace collections for automatic estimation of static corrections. *Geophys Prospect*. 1985;33:1212-1231.
doi: 10.1111/j.1365-2478.1985.tb01360.x
14. Molyneux JB, Schmitt DR. First-break timing: Arrival onset times by direct correlation. *Geophysics*. 1999;64:1492-1501.

doi: 10.1190/1.1444653

15. Mousa WA, Al-Shuhail A, Al-Lehyani A. A new technique for first-arrival picking of refracted seismic data based on digital image segmentation. *Geophysics*. 2011;76:V79-V89.

doi: 10.1190/geo2010-0322.1

16. Zhang H, Thurber C, Rowen C. Automatic P-wave arrival detection and picking with multiscale wavelet analysis for single-component recordings. *Bull Seismol Soc Am.* 2003;93:1904-1912.

doi: 10.1785/0120020241

17. Alao JO, Lawal KM, Dewu BBM, Raimi J. Near-surface seismic refraction anomalies due to underground target models and the application in civil and environmental engineering. *Phys Chem Earth.* 2025;138:103845.

doi: 10.1016/j.pce.2024.103845

18. Gülünay N. The diminishing residual matrices method for surface-consistent statics: A review. *Geophysics*. 2017;82(4):V257-V274.

doi: 10.1190/geo2016-0602.1

19. Allen PA, Allen JR. *Basin Analysis: Principles and Application to Petroleum Play Assessment*. 3rd ed. United States: Wiley and Blackwell; 2013.

20. Biddle KT, Christie-Blick N. Deformation and sedimentation in basins. In: *Tectonics and Sedimentation*. Tulsa: Society of Economic Paleontologists and Mineralogists; 1985.

21. Gaci S, Hachay O, Nicolis O. *Methods and Applications in Petroleum and Mineral Exploration and Engineering Geology*. USA: Elsevier Editions; 2021. p. 410.

22. Gaci S, Hachay O. *Oil and Gas Exploration: Methods and Application*. American Geophysical Union. USA: Wiley Editions; 2017. p. 296.

23. Gaci S, Hachay O. *Advances in Data, Methods, Models and Their Applications in Oil/Gas Exploration*. Broadway: Publishing Group Editions; 2014. p. 382.

24. Ladjadj Y. *Structural Study of the Lower Chellif Basin Based on Gravimetric, Magnetic, and Seismic Data. (Thesis Title Translated from French). Master's Thesis*. Ferhat Abbas University-Sétif 1; 2018. Available from: https://dspace.univ-setif.dz:8888/jspui/handle/123456789/2448 [Last accessed on 2025 Aug 20].

25. Sclater JG, Christie PAF. Continental stretching: An explanation of the post-mid-cretaceous subsidence of the central North Sea Basin. *J Geophys Res.* 1980;85(B7):3711-3739.

26. Ziegler PA. Geodynamic evolution of the north sea rift and its influence on the development of the North Sea Basin. In: *The North Sea: A Geoscientific Perspective*. London: The Geological Society; 1990.

27. Robinson EA, Treitel S. Principles of digital filtering. *Geophysics*. 1964;29:395-404.

28. Buttkus B. *Spectral Analysis and Filter Theory in Applied Geophysics*. Berlin, Heidelberg: Springer; 2000.

doi: 10.1007/978-3-642-57016-2

29. Oppenheim AV, Schafer RW. *Discrete-Time Signal Processing*. 3rd ed. United Kingdom: Pearson; 2013.

30. Dong X, Yang D. Crustal flow-induced earthquake revealed by full-waveform tomography and implications for prehistoric civilization destruction. *J Geophys Res Solid Earth*. 2025;130(4).

doi: 10.1029/2024JB029745

31. Fu L, Guo J, Shen W, *et al*. Geophysical evidence of the collisional suture zone in the Prydz Bay, East Antarctica. *Geophys Res Lett.* 2024;51(2):e2023GL106229.

doi: 10.1029/2023GL106229

32. Zhang H, Bao X, Zhao H. High-precision deblending of 3-D simultaneous source data based on prior information constraint. *IEEE Geosci Remote Sens Lett.* 2025;22:1.

doi: 10.1109/LGRS.2025.3526972

33. Zhou G, Xu C, Zhang H, *et al*. PMT gain self-adjustment system for high-accuracy echo signal detection. *Int J Remote Sens.* 2022;43(19-24):7213-7235.

doi: 10.1080/01431161.2022.2155089

34. Zhai Z, Shu Q, Chen H, Liu Y. CCQC-based multi-seismic level optimum design of supplemental dampers in steel moment resisting frame. *J Build Eng.* 2025;108:112922.

doi: 10.1016/j.jobe.2025.112922

35. Zhang C, Zhu Z, Dai L, Wang S, Shi C. The incompatible deformation mechanism of underground tunnels crossing fault conditions in the southwest edge strong seismic zone of the Qinghai-Tibet Plateau: A study of shaking table test. *Soil Dyn Earthq Eng.* 2025;197:109482.

doi: 10.1016/j.soildyn.2025.109482

36. Liang S, Suping P, Dengke H. A novel static correction approach for eliminating the effect of geophones - a case study in coal reservoirs, Ordos Basin, China. *Energies*. 2018;11:3240.

doi: 10.3390/en11123240

ACCSCIENCE PUBLISHING

Journal of Seismic Exploration

ARTICLE

Optimization of the SOM neural network model using CEEMDAN distribution entropy and ALO for seismic and blasting identification

Ailing Wang[1], Cong Pang[2,3], Guoqing Chen[1], Chawei Li[2,3], and Tianwen Zhao[4]*

[1]Mathematical Modeling Research Center, Chengdu Jincheng College, Chengdu, Sichuan, China

[2]Institute of Seismology, China Earthquake Administration, Wuhan, Hubei, China

[3]National Observation and Research Station for Wuhan Gravitation and Solid Earth Tides, Hubei Earthquake Administration, Wuhan, Hubei, China

[4]Department of Trade and Logistics, Daegu Catholic University, Gyeongsan, Daegu, Republic of Korea

Abstract

As seismic signals and artificial blasting signals exhibit high similarity in time–frequency domain features, resulting in insufficient recognition accuracy, we propose a self-organizing map (SOM) neural network classification model based on complete ensemble empirical mode decomposition with adaptive noise (CEEMDAN) multiscale distribution entropy (MDE) feature extraction and Ant Lion Optimization (ALO) algorithm improvement. The multiscale decomposition of the original seismic and blasting signals was carried out using CEEMDAN, and the distribution entropy values of the obtained multiple intrinsic mode functions were calculated to construct multidimensional feature inputs containing complexity information in the time–frequency domain. The ALO algorithm optimized the key parameters of the SOM neural network (competing layer dimensions and number of training iterations), with the root mean squared error serving as the fitness function. The optimal solution obtained by ALO optimization replaced the hyperparameter values in the original model, and multiple prediction rounds were performed on the seismic data test set to address unstable classification performance caused by random initialization in the traditional SOM network. The results revealed that the recognition performance of the CEEMDAN–MDE combined with the ALO–SOM model was significantly improved compared with machine learning models, such as linear discriminant analysis (LDA), decision tree, support vector machine, probabilistic LDA, and AdaBoost. Its recognition accuracy, recall, and F1-score were 99.3373%, 99.1479%, and 99.4557%, respectively, suggesting that this method can serve as a reliable approach for accurately differentiating between natural earthquakes and artificial blasting events, with important application value for seismic monitoring and blasting event exclusion.

Keywords: Seismic signal recognition; Complete ensemble empirical mode decomposition with adaptive noise; Self-organizing feature mapping neural network; Ant Lion Optimization algorithm; Multiscale distributional entropy

***Corresponding author:**
Tianwen Zhao
(zhaotianwen305@gmail.com)

Citation: Wang A, Pang C, Chen G, Li C, Zhao T. Optimization of the SOM neural network model using CEEMDAN distribution entropy and ALO for seismic and blasting identification. *J Seismic Explor*. 2025;34(2):28-43.
doi: 10.36922/JSE025280033

Received: July 13, 2025

Revised: August 3, 2025

Accepted: August 12, 2025

Published online: August 28, 2025

1. Introduction

High-precision identification of earthquakes and explosions is one of the major challenges in seismic observation data processing. Although there are essential differences between the two in terms of earthquake mechanisms and energy release modes, they exhibit high similarity in time-domain waveforms and spectral characteristics, which is of great significance for earthquake early warning, nuclear explosion monitoring, and engineering safety assessment.[1-4] Traditional identification methods typically rely on artificial empirical features (e.g., P/S wave amplitude ratio, spectrum envelope shape, energy spectrum statistical parameters, and P-wave initial motion direction), and the recognition rate drops significantly in strong-noise environments and when the ground-motion energy difference is small.[5-7] With the increase in seismic network density and the improvement of monitoring requirements, intelligent recognition methods based on machine learning have gradually become mainstream; however, their performance is still limited by two bottlenecks: insufficient feature representation capability and weak model generalization. Therefore, integrating adaptive signal decomposition, non-linear dynamic feature extraction, and intelligent optimization models to overcome the recognition accuracy limitations of existing technologies has become a frontier research direction in seismic waveform recognition.

Techniques combining spectrum analysis and machine learning can be used for the accurate recognition of seismic waves at this stage. The integration of non-linear signal processing methods, such as wavelet transform and Hilbert–Huang transform with neural networks has been successfully applied to seismic data processing.[8-10] The development of adaptive signal decomposition methods provides a new paradigm for seismic wave feature extraction. Empirical mode decomposition (EMD) and its derivatives achieve multiscale analysis of signals by decomposing non-linear and non-stationary signals into intrinsic mode functions (IMFs).[11,12] However, traditional EMD suffers from mode aliasing. Although ensemble EMD (EEMD) alleviates this defect by adding Gaussian white noise, it introduces residual noise interference.[13,14] To address these limitations, complete ensemble empirical mode decomposition with adaptive noise (CEEMDAN) has been developed. Its core innovation lies in the adaptive noise injection mechanism and residual noise isolation strategy: (i) signal contamination is avoided by adding auxiliary noise IMF components decomposed by EMD to the original signal (rather than adding raw white noise); and (ii) after each IMF extraction, integrated averaging is performed immediately to prevent residual noise transmission to low-frequency components. These improvements make CEEMDAN significantly superior to previous methods in signal completeness, modal separation, and computational efficiency, and particularly suitable for pre-processing non-stationary signals, such as seismic waves.[15,16]

At the feature quantification level, multiscale distribution entropy (MDE), an emerging representative of non-linear dynamic characteristics, effectively reveals the essential differences between earthquake and explosion signals by measuring the probability distribution complexity of IMF components at different time scales. Compared with traditional sample entropy,[17] MDE has three major advantages:

(i) Multiscale analysis capability: extracts multiscale information of time series through a coarse-graining process, avoiding the one-sidedness of single-scale analysis.
(ii) Distribution sensitivity: based on probability distribution difference (Euclidean distance or Kullback–Leibler divergence) rather than mean quantization complexity, making it more suitable for non-Gaussian distribution signals.
(iii) Noise robustness: sensitivity to random noise is significantly lower than that of sample entropy. This feature was verified in the processing of earthquake data from Maduo County, Qinghai Province, China, in 2021.

Early recognition models were mainly based on statistical classifiers (e.g., support vector machines [SVMs], random forests, and Adaboost) and shallow neural networks (e.g., backpropagation, radial basis function, and probabilistic neural network), and their performance was highly dependent on artificial feature engineering.[18-21] By extracting features, such as the number of spectral peaks and the short-time energy zero-crossing rate of seismic signals and combining them with SVM classification, recognition rates of up to 85% can be achieved in simple scenarios. However, these models face two major challenges:

(i) Feature–model decoupling: feature extraction and classification models are designed independently, resulting in information transmission loss.
(ii) Overfitting of small samples: seismic event samples are scarce and unevenly distributed, making complex models prone to local optimality.

In recent years, deep neural networks have shown great potential in seismic analysis. As an unsupervised competitive learning model, self-organizing map (SOM) networks retain the ability to reduce the dimensionality of high-dimensional data while preserving topological

structures and are adept at handling complex, non-linear, non-stationary data, making them an ideal choice for seismic signal recognition. Their core advantages are:

(i) Visual interpretability: mapping high-dimensional features to a two-dimensional grid to intuitively display the separation of earthquake and explosion clusters.
(ii) Small-sample adaptability: a robust mapping can be constructed without large-scale training data.[22]

However, the fixed network structure and sensitivity to random initialization parameters of traditional SOMs can affect the overall performance of earthquake and explosion recognition, leading to prediction results with large standard deviations (SDs).[23-25] To address this issue, intelligent biomimetic algorithms are introduced to optimize multiple network hyperparameters of the SOM model, aiming to identify the optimal hyperparameters for the training set and thereby improve the prediction accuracy and output robustness of the original model. Ant Lion Optimization (ALO) simulates the collaborative hunting mechanism of antlions, balancing global exploration and local exploitation capabilities through elite individual guidance and random walk strategies. It is particularly suitable for weight initialization and topological structure adjustment in SOM models, helping determine appropriate competition-layer parameters and initial learning rates, which are then applied to the prediction model in this study.[26,27]

To address the defects of low recognition rate, poor robustness, and imperfect feature learning of machine learning models in seismic wave recognition, the present study employs novel spectrum analysis technology and an improved unsupervised learning algorithm to develop a hybrid model for natural earthquake and artificial explosion signal recognition. The key objective is to design a series of new multiscale spectrum feature criteria based on CEEMDAN with adaptive noise and distribution entropy (DistEn),[28,29] and to propose an innovative CEEMDAN–MDE–ALO–SOM hybrid model optimized using the ALO algorithm.[30] This study makes the following important contributions to the field of natural earthquake and artificial explosion signal recognition:

(i) Novel multiscale feature extraction framework: an improved signal decomposition method based on CEEMDAN is proposed. Across the adaptive noise injection mechanism and residual noise isolation strategy, the modal aliasing problem in the traditional EMD/EEMD method is effectively solved. Combined with the 12-dimensional feature vector constructed by MDE, a comprehensive quantitative characterization of the complexity of seismic signals in the time and frequency domains is achieved for the first time.
(ii) Intelligent optimization of neural network architecture: ALO is innovatively applied to parameter optimization of the SOM neural network, and an automatic parameter adjustment mechanism is established, with the competition-layer dimension and the number of training iterations as optimization variables and root mean squared error as the fitness function. This method addresses the performance instability problem caused by the random initialization of traditional SOM and reduces the SD of classification accuracy to 1.166.
(iii) Interdisciplinary method integration: for the first time, adaptive signal processing (CEEMDAN), non-linear dynamics (MDE), bionic optimization algorithm (ALO), and unsupervised learning (SOM) are systematically integrated to construct an end-to-end intelligent recognition framework. This fusion model is theoretically innovative in the coordinated optimization of feature extraction and classification decision-making.
(iv) Large-scale empirical verification: a rigorous verification scheme, including hundreds of Monte Carlo experiments, is designed based on 414 sets of multi-source data from authoritative institutions, such as the Institute of Engineering Mechanics, China Earthquake Administration. The experimental results not only confirm the model's 99.337% recognition accuracy (F1-score = 99.456%) but also quantify its stability advantage through statistical indicators, such as the coefficient of variation (CV) (CV = 0.0117).
(v) Engineering application value: the developed feature extraction and classification module is encapsulated as a MATLAB-callable function library, supporting real-time signal processing. The model's test performance in the 2021 Qinghai Maduo earthquake aftershock sequence (recall rate = 99.148%) provides a feasible technical solution for reducing the false alarm rate of earthquake monitoring systems.

This study adopts a progressive structure of "theoretical modeling–method innovation–experimental verification–application discussion" to organize the full text. Section 2 systematically explains the mathematical principles of the ALO–SOM model, including the elite retention mechanism and random walk strategy of the ALO algorithm, the competitive learning dynamics model of the SOM network, and the complete algorithm flow chart (Figure 1). Section 3 details the CEEMDAN–MDE feature extraction method, covering the adaptive noise injection strategy of CEEMDAN, the multiscale probability distribution quantization method of MDE, and the criteria for selecting IMF components (Figures 2 and 3). Section 4 presents a rigorous controlled-variable experiment,

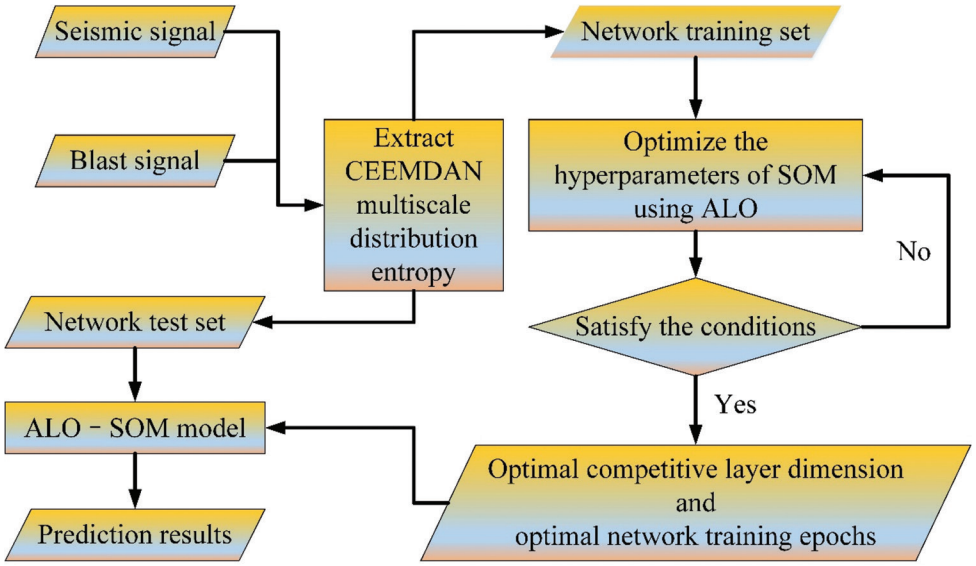

Figure 1. Flowchart of the ALO–SOM model for recognizing earthquakes and blasting.
Abbreviations: ALO: Ant Lion Optimization; CEEMDAN: Complete ensemble empirical mode decomposition with adaptive noise; SOM: Self-organizing map.

explaining the data sources and pre-processing procedures, demonstrating the ALO optimization process (Figure 4) and hyperparameter sensitivity analysis, and finally comparing six benchmark models through box plots (Figure 5) and statistical tables (Tables 1 and 2). Section 5 discusses three key issues in depth, including a comparison of spectral resolution with methods, such as EEMD–VMD, the robustness boundary in strong-noise environments, and the trade-off between computational efficiency and real-time performance. Section 6 summarizes the research results and future directions, including lightweight model deployment, cross-regional generalization testing, and the construction of a multimodal data fusion recognition framework.

2. ALO–SOM seismic wave identification model

2.1. ALO

ALO is a heuristic algorithm proposed by Mirjalili *et al.*[31] in 2015, inspired by the behavior of antlions hunting prey in nature. The algorithm imitates the habits of antlions setting traps, prey random walks, and antlions waiting to hunt. It adopts a fast convergence mechanism based on trap boundary search and elite retention, and applies roulette and random walk strategies to improve global search capabilities. It features strong robustness and simple algorithm settings. The ALO algorithm process is described in the following sections.

2.1.1. Ant random walk

The set of ant random walk steps is defined as $X_i(t)$, with the initial step number set to 0. The ant random walk is constrained within a range-limited domain, and the ant position needs to be normalized based on **Equation I**:

$$X_i^t = \frac{\left(X_i - a_i\right)\times\left(d_i^t - c_i^t\right)}{\left(b_i - a_i\right)} + c_i^t \quad \text{(I)}$$

where X_i^t is the normalized result of the ant random walk step set X_i within the feasible domain; a_i and b_i are the minimum and maximum values of the ant position vector on the i-th dimension, preset by the algorithm; and c_i^t and d_i^t are the minimum and maximum values of the ant position on the i-th dimension at the t-th iteration.

2.1.2. Antlion sets a trap

When an ant mistakenly enters the trap pit dug by the antlion, the ant's movement is restricted, and the walking formulas within the trap are given in **Equations II and III**:

$$c_i^t = A_j^t + c^t \quad \text{(II)}$$

$$d_i^t = A_j^t + d^t \quad \text{(III)}$$

Where c^t is the minimum value of all variables at the t-th iteration, d^t is the maximum value of all variables at the t-th iteration, and A_j^t is the antlion j selected at the t-th iteration.

2.1.3. Antlion trapping target

When the antlion finds an ant, it throws sand to the edge of the sand pit to prevent the ant from escaping, causing

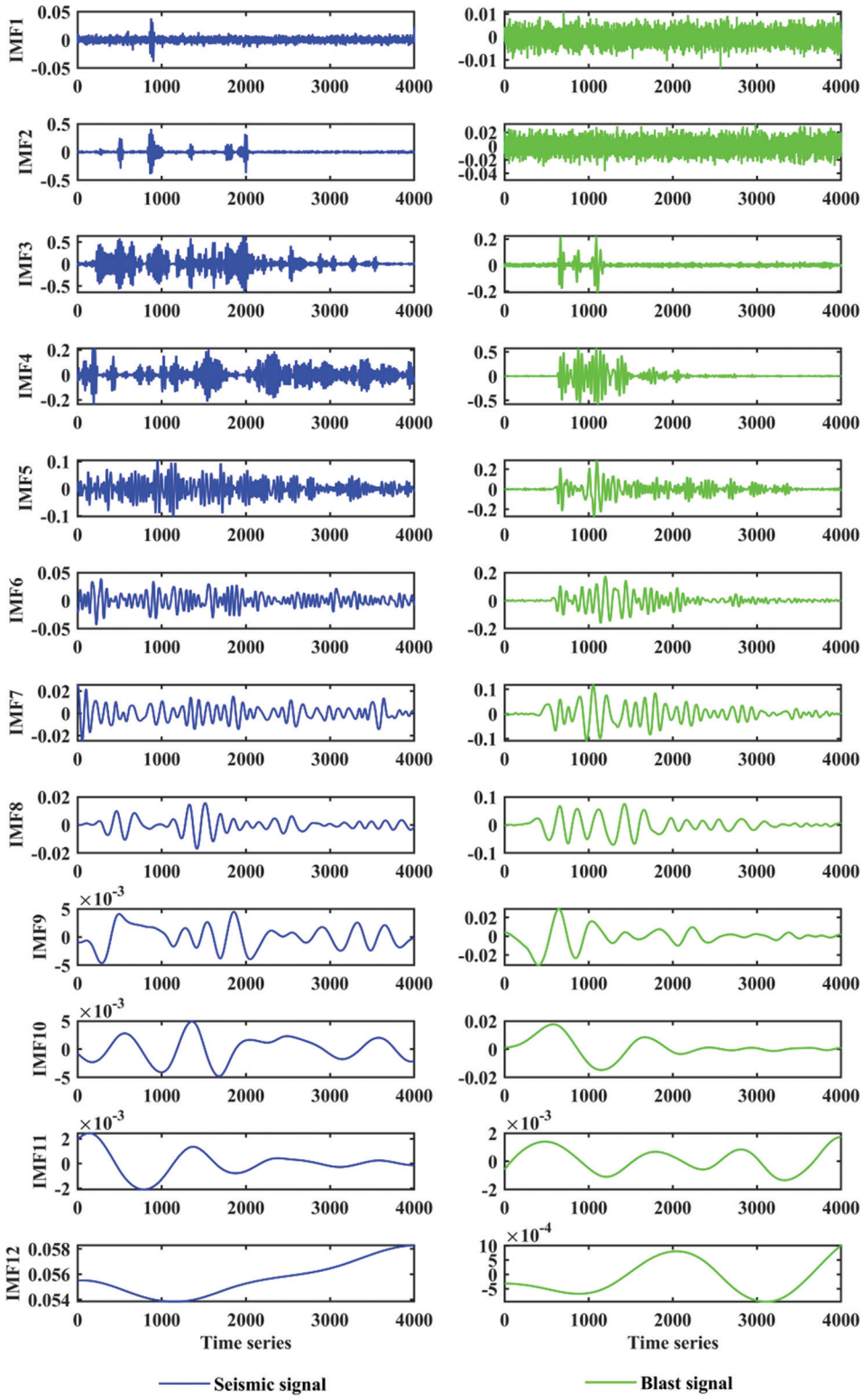

Figure 2. Comparison of complete ensemble empirical mode decomposition with adaptive noise decomposition results between single earthquake and blasting waveforms.
Abbreviation: IMF: Intrinsic mode function.

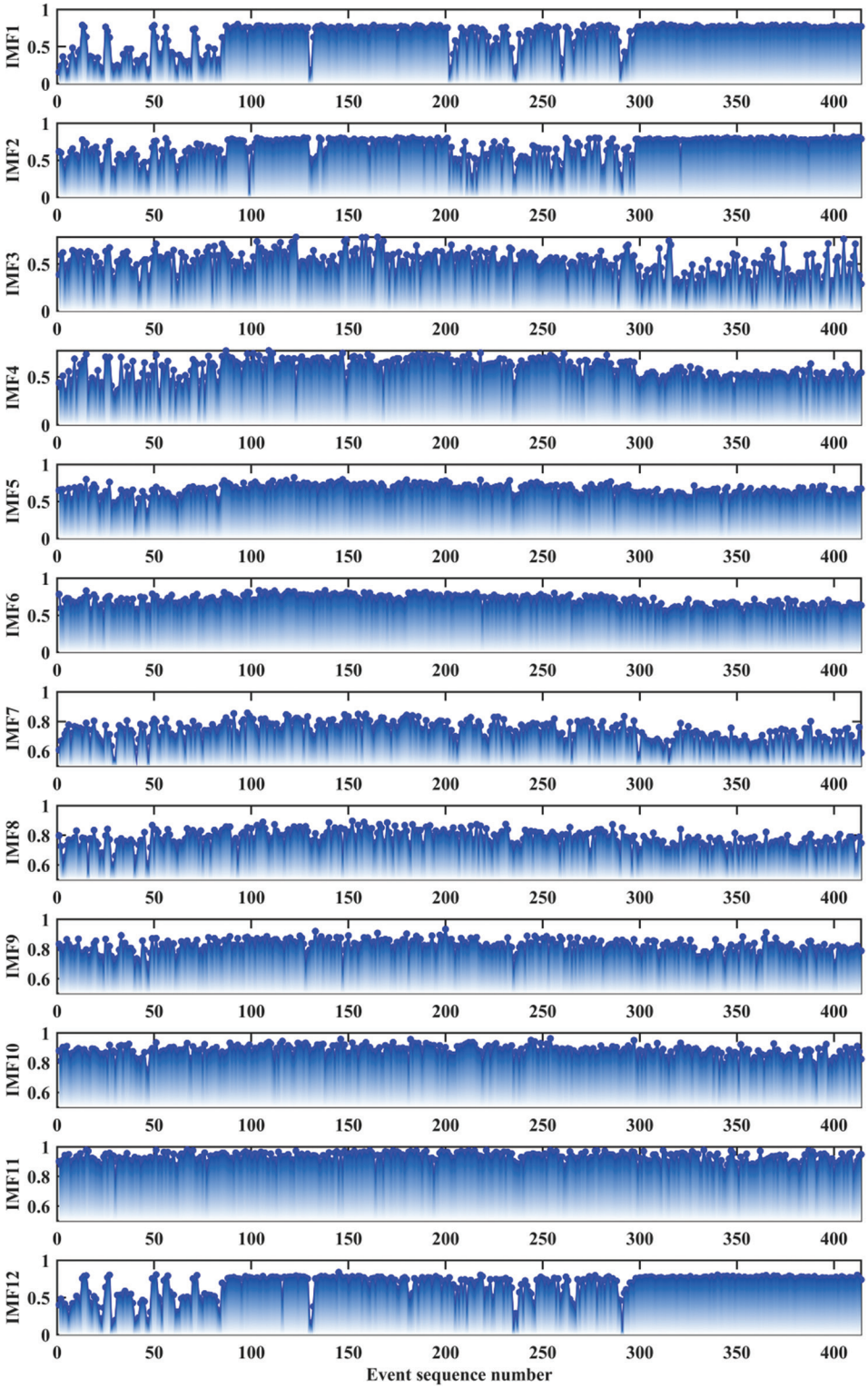

Figure 3. Distribution entropy of IMF components from complete ensemble empirical mode decomposition with adaptive noise for earthquake and explosion waveforms.
Abbreviation: IMF: Intrinsic mode function.

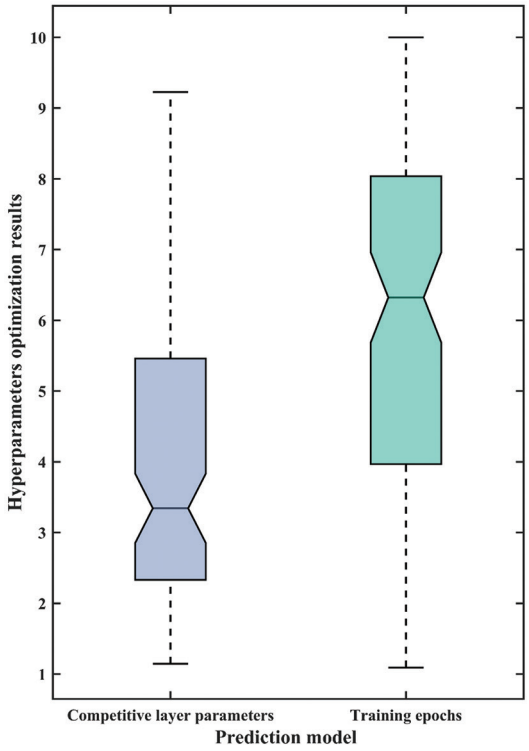

Figure 4. Hyperparameter results for the Ant Lion Optimization-optimized self-organizing map across 100 discrimination subtrials.

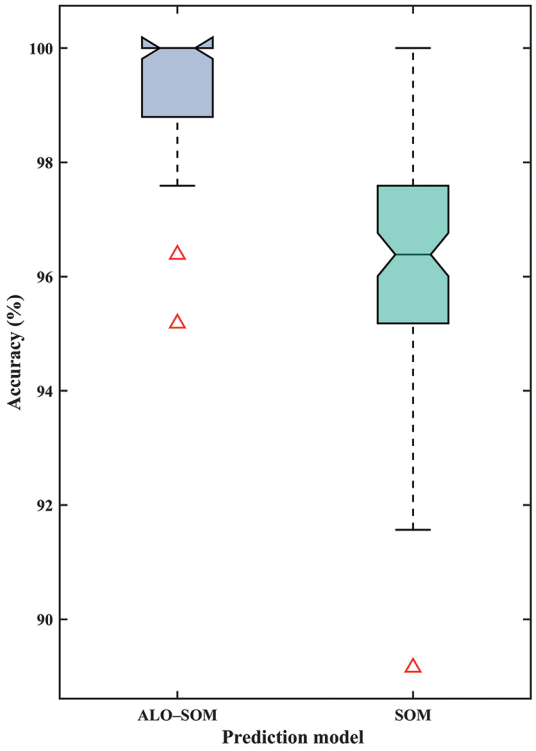

Figure 5. Box plot of 100 identification results comparing the ALO–SOM model and the SOM model. Data points marked with red triangles are identified as outliers in the box plot.
Abbreviations: ALO: Ant Lion Optimization; SOM: Self-organizing map.

the ant to slide continuously toward the antlion at the bottom of the pit. The ALO algorithm uses roulette wheel selection to identify the appropriate antlion position and dynamically narrows the trap range to speed up the capture of ants. The relevant formulas are given in **Equations IV–VI**:

$$c^t = \begin{cases} c^t, t \le 0.1T \\ T \times c^t\left(10^w \times t\right), t > 0.1T \end{cases} \quad \text{(IV)}$$

$$d^t = \begin{cases} d^t, t \le 0.1T \\ T \times d^t\left(10^w \times t\right), t > 0.1T \end{cases} \quad \text{(V)}$$

$$w = \begin{cases} 2, 0.10T < t \le 0.50T \\ 3, 0.50T < t \le 0.75T \\ 4, 0.75T < t \le 0.90T \\ 5, 0.90T < t \le 0.95T \\ 6, 0.95T < t \le T \end{cases} \quad \text{(VI)}$$

Where T is the preset upper limit of the number of algorithm iterations, and w is the dynamic weight factor related to the present number of iterations t. **Equation VI** shows a stepwise increasing trend for w.

Table 1. Statistical summary of 100 comparison tests between the ALO–SOM and SOM models

Identification model	Accuracy				
	Mean (%)	SD	Range	CV	IQR
SOM	96.5904	1.9303	10.8434	0.0200	2.4096
ALO–SOM	99.3373	1.1662	4.8193	0.0117	1.2048

Abbreviations: ALO: Ant Lion Optimization; CV: Coefficient of variation; IQR: Interquartile range; SOM: Self-organizing map; SD: Standard deviation.

2.1.4. Preying on ants

When the prey slides to the bottom of the pit, the antlion moves quickly and catches the prey. This biological phenomenon is modeled algorithmically by comparing the fitness values of the ant and the antlion. When the ant's fitness value is higher than that of the antlion, the position of the antlion is updated to the present position of the ant. The relevant formula is given in **Equation VII**:

$$Antlion_j^t = Ant_i^t, f_{obj}^{ant}\left(t\right) < f_{obj}^{antlion}\left(t\right) \quad \text{(VII)}$$

where $Antlion_j^t$ is the position of the antlion at the t-th iteration; Ant_i^t is the position of the ant at the t-th iteration;

Table 2. Statistical summary of the recognition effect of 100 rounds of six machine learning models

Identification method	Mean		
	Accuracy (%)	Recall (%)	F1-score (%)
LDA	94.4458	95.0857	96.0652
Decision tree	94.7590	96.7272	96.2864
SVM	96.7470	97.8544	97.7154
PLDA	94.7229	95.5762	96.2838
AdaBoost	94.2892	95.8346	96.0004
CNN	93.4504	94.6401	95.0182
ALO–SOM	99.3373	99.1479	99.4557

Abbreviations: ALO: Ant Lion Optimization; CNN: Convolutional neural network; LDA: Linear discriminant analysis; PLDA: Probabilistic linear discriminant analysis; SOM: Self-organizing map; SVM: Support vector machine.

and $f_{obj}^{ant}(t)$ and $f_{obj}^{antlion}(t)$ are the fitness function values of the ant and antlion, respectively, at the t-th iteration.

2.1.5. Elite antlion strategy

The movement of the ant is influenced by both the present elite antlion position and the antlion position selected by the roulette wheel. The ant position is defined by **Equation VIII**:

$$Ant_i^{t+1} = \frac{R_A^t(l) + R_E^t(l)}{2} \quad \text{(VIII)}$$

where Ant_i^{t+1} represents the position of the i-th ant in iteration $t + 1$; $R_A^t(l)$ is the latest position of the random walk steps near the antlion selected by roulette at the t-th iteration; and $R_E^t(l)$ is the position of the ant in the random walk of l steps near the elite antlion at iteration t (the best antlion position found at each iteration).

2.2. Self-organizing feature mapping neural network

SOM is an unsupervised machine learning method, also known as the Kohonen network. Its key idea is to map and compress high-dimensional data onto a two-dimensional plane while preserving the topological structure of the original data to obtain the feature similarity distribution of the output layer. It has advantages, such as effective processing of non-linear data, producing intuitive and visual results, and not requiring preset labels. The calculation steps of the SOM network are detailed in the following sections.

2.2.1. Competition process

The Euclidean distance between the input vector X and the weight vector W_j of the competition layer neuron is calculated based on **Equation IX**:

$$d_j = X - W_j = \sqrt{\sum_{i=1}^{m}\left(x_i(t) - w_{ij}(t)\right)^2} \quad \text{(IX)}$$

Where $X = (x_1, x_2, \ldots, x_m)^T$ is the input vector; W_j is the weight vector of the competition layer neuron j; w_{ij} is the weight connecting input neuron i and competition neuron j.

The best matching unit (BMU) is defined as the neuron with the smallest d_j:

$$BMU = \arg\min_j X - W_j \quad \text{(X)}$$

2.2.2. Cooperation process

During the cooperation process, the weights of the BMU and its adjacent neurons are updated. The adjacent spatial range is defined by the Gaussian function h, where σ decreases with time t, thereby dynamically adjusting the adjacent spatial range of the BMU. The formula is given in **Equation XI**:

$$h(j, BMU, t) = \exp\left(-\frac{distance(j, BMU)^2}{2\sigma(t)^2}\right) \quad \text{(XI)}$$

2.2.3. Adaptation process

To make the BMU approach the input vector, this process introduces the learning rate η and the Gaussian function h to update the BMU and the weights of its neighboring neurons. The learning rate η decreases with the number of iterations based on the initial learning rate η_0, as defined in **Equation XII**:

$$\eta(t) = \eta_0 \exp\left(-\frac{t}{\tau}\right) \quad \text{(XII)}$$

where τ is the time constant that determines the decay rate of the learning rate.

$W_j(t + 1)$ is the weight vector of the competition layer neuron j at time $t + 1$.

$$W_j(t+1) = W_j(t) + \eta(t) \cdot h(t) \cdot (x - W_j(t)) \quad \text{(XIII)}$$

2.2.4. Training process

During the training process, weights are initialized, samples are randomly selected to calculate the BMU, and the BMU, along with its neighboring weights, are updated. Simultaneously, the neighborhood radius and learning rate decrease as the number of iterations increases.

2.3. ALO–SOM model recognition principle

The classification results of SOM networks are influenced by multiple network hyperparameters and must be controlled in combination with other methods to obtain more accurate and stable unsupervised clustering results.

To achieve this, the ALO algorithm, which mimics the antlion's strategy of setting traps to hunt ants, is introduced to optimize certain SOM hyperparameters (e.g., competition layer dimension and network training iterations), thereby developing a new model capable of adaptively training for earthquake and explosion recognition on the training dataset.

Figure 1 illustrates the process of the ALO algorithm optimizing the SOM neural network hyperparameters and performing pattern recognition. The ALO algorithm uses two hyperparameters from the SOM—the dimension of the competition layer and the number of network training iterations—as optimization variables. It employs the root mean squared error between the actual prediction result vector $\vec{R}$ and the theoretical category label vector $\vec{T}$ obtained from SOM recognition using the test set as the fitness function for ALO optimization (**Equation XIV**):

$$fitness = RMSE\left(\vec{R},\vec{T}\right) \tag{XIV}$$

Based on the training set, the optimal hyperparameter values that satisfy the iteration stopping criteria are obtained, and finally, the ALO–SOM recognition model is used to identify the test set.

3. CEEMDAN MDE feature extraction

An efficient and reasonable new neural network model does not necessarily guarantee high accuracy in effectively distinguishing between earthquakes and explosions; it also requires a reliable seismic waveform feature extraction process. In this section, we provide a detailed introduction to the basic concepts and computational process of CEEMDAN, which enables the extraction of seismic waveform features across multiple frequency scales, thereby enabling a more comprehensive and precise analysis of the time–frequency differences between earthquakes and explosions.

3.1. CEEMDAN

CEEMDAN is an advanced signal decomposition method based on EMD and EEMD techniques. It enhances signal decomposition by adding complementary pairs of adaptive white noise to the original signal, performing multiple EMD decompositions, and averaging the results. This process effectively minimizes parameter interference and suppresses mode aliasing by isolating residual components. CEEMDAN overcomes key limitations of earlier methods—including modal overlap, low reconstruction accuracy, reliance on fixed parameters, and low decomposition efficiency—thus significantly improving the reconstruction purity of IMFs. It is particularly suitable for analyzing non-linear and non-stationary signals, such as complex seismic data.

(a) Step 1

m pairs of positive and negative Gaussian white noises $\omega_i(t)(i = 1,2,\ldots,m)$ with zero mean and constant SD are added to the original signal $x(t)$, generating *m* synthetic noisy signals $X_i^1(t)$ based on **Equation XV**:

$$X_i^1(t) = x(t) + (-1)^q \cdot \beta \cdot \omega_i\left(t\right) \tag{XV}$$

where β is the noise coefficient related to the amplitude, and $q = 1,2$.

(b) Step 2

Empirical mode decomposition is applied to the noisy signals to obtain the first-order components. Each signal $X_i^1(t)$ is decomposed by EMD into an IMF component $IMF_i^1(t)$ and a residual component $r_i^1(t)$, as expressed in **Equation XVI**:

$$X_i^1\left(t\right) = IMF_i^1\left(t\right) + r_i^1\left(t\right) \tag{XVI}$$

The first-order IMFs $IMF_i^1(t)$ of all *m m* synthetic noisy signals $X_i^1(t)$ are calculated, and their arithmetic average is taken to obtain the first-order $IMF^1(t)$ $IMF^1(t)$ of the CEEMDAN algorithm. The relevant formulas are given in **Equations XVII and XVIII**:

$$IMF^1\left(t\right) = \frac{1}{m}\sum_{i=1}^{m} IMF_i^1\left(t\right) \tag{XVII}$$

$$r^1\left(t\right) = x\left(t\right) - IMF^1\left(t\right) \tag{XVIII}$$

(c) Step 3

Using a similar calculation strategy as in **Equations XV–XVIII**, the next-order component $IMF^{k-1}(t)$ is calculated step by step: for the residual $r^{k-1}(t)(k \geq 2)$ obtained in the previous step, positive and negative noise $(-1)^q \beta_{k-1} E_{k-1}(\omega_i[t])$ are added, respectively, to obtain *m* new signals $X_i^{k-1}(t)$, where β_{k-1} is the dynamically reduced noise coefficient, and $E_{k-1}(\cdot)$ is the residual after the $(k-1)$-th order EMD decomposition of the white noise $\omega_i(t)$. Performing EMD decomposition on each $X_i^{k-1}(t)$ yields *m* components $IMF_i^{k-1}(t)$, as given in **Equation XIX**:

$$X_i^{k-1}\left(t\right) = IMF_i^{k-1}\left(t\right) + r_i^{k-1}\left(t\right) \tag{XIX}$$

Taking the arithmetic average yields the $(k-1)$-th order component $IMF^{k-1}(t)$ of the CEEMDAN algorithm. The relevant formulas are given in **Equations XX and XXI**:

$$IMF^{k-1}\left(t\right) = \frac{1}{m}\sum_{i=1}^{m} IMF_i^{k-1}\left(t\right) \tag{XX}$$

$$r^{k-1}\left(t\right) = r^{k-2}\left(t\right) - IMF^{k-1}\left(t\right), k \geq 2 \tag{XXI}$$

(d) Step 4

After the iterative calculation is completed, the original signal is reconstructed. The iterative calculation from the previous step stops when the residual component becomes a monotonic function or when its extreme points are insufficient for further EMD decomposition. A total of $k-1$ CEEMDAN IMFs are obtained; the original signal $x(t)$ can be reconstructed by summing the $k-1$ IMFs and the final residual component $r^{k-1}(t)$ as follows (**Equation XXII**):

$$x(t) = r^{K-1}(t) + \sum_{k=2}^{K} IMF^{k-1}(t), \quad k = 2,...,K \tag{XXII}$$

The hyperparameters of the CEEMDAN algorithm are set as follows: the SD of white noise is 0.2, the number of noise additions is 24, and the maximum number of iterations allowed is 3,600. Figure 2 shows the CEEMDAN decomposition results of natural earthquake signals (left) and artificial blasting signals (right), where rows 1–12 correspond to the IMF_1–IMF_{12} components obtained by CEEMDAN decomposition. The waveform signal length is L = 4,000 and the components are arranged in descending order of frequency or energy size.

3.2. Calculation of MDE using CEEMDAN

DistEn is a parameter used in information theory to measure the uncertainty of data distribution or the complexity of a time series.[28,29] DistEn obtains the probability density function by directly calculating the Chebyshev distance and kernel density estimation between reconstructed vectors, thereby avoiding the problem of manually selecting the tolerance parameter r used in sample entropy. In addition, it has the advantages of being parameter-free and robust.

The original seismic signal is decomposed into several IMFs with monotonically decreasing frequencies and significant differences in energy distribution by using the adaptive noise CEEMDAN. By sequentially calculating the DistEn values of all IMF components obtained from decomposition (i.e., the DistEn of IMF_1–IMF_{12} shown in Figure 3), a one-dimensional vector that describes the different frequency distribution characteristics of the original signal is formed, referred to as MDE. This method can effectively extract multiscale pure characteristic parameters that characterize different source systems and enables robust identification of signals generated by different dynamic mechanisms. The horizontal axis of Figure 3 represents the sequence numbers of 414 earthquake and explosion waveforms, while the vertical axis shows the DistEn values of the IMF components obtained from CEEMDAN decomposition.

4. Data and experiments

In this study, we first organized the collected data and developed an experimental framework to rigorously evaluate the effectiveness and specific capabilities of the proposed method in distinguishing between earthquake and blasting events. A total of 414 sets of multi-source strong motion observation data were utilized, as follows:

(i) Earthquake case data publicly shared by the National Earthquake Data Center (data.earthquake.cn) and the Institute of Engineering Mechanics of the China Earthquake Administration: 2021 Jiangtianning MS 4.2 earthquake strong motion acceleration records (96 records); 2021 Jiangsu Dafeng MS5.0 earthquake strong motion acceleration records (117 records); and 2021 Yunnan Yangbi MS6.4 main shock aftershock sequence acceleration records (magnitude range MS2.9-3.9, 84 records).

(ii) Controllable artificial blasting test acceleration waveforms (117 records) provided by the Geotechnical Engineering Institute, China Institute of Water Resources and Hydropower Research (www.geoeng.iwhr.com).

All data pre-processing and numerical analyses were implemented on the MATLAB 2019a (The MathWorks, Inc., United States) computing platform. The formulas for accuracy, recall, and F1-score are as follows:

(i) Accuracy indicates the proportion of samples correctly predicted by the model to the total number of samples (**Equation XXIII**).

$$\text{Accuracy} = \frac{\text{TP} + \text{TN}}{\text{TP} + \text{TN} + \text{FP} + \text{FN}} \times 100\% \tag{XXIII}$$

(ii) Recall refers to the proportion of positive samples correctly identified by the model to all actual positive samples (**Equation XXIV**).

$$\text{Recall} = \frac{\text{TP}}{\text{TP} + \text{FN}} \times 100\% \tag{XXIV}$$

(iii) The F1-score is the harmonic mean of precision and recall and is an important indicator for measuring the overall performance of the model (**Equation XXV**).

$$\text{F1} - \text{score} = \frac{2 \times \text{Accuracy} \times \text{Recall}}{\text{Accuracy} + \text{Recall}} \times 100\% \tag{XXV}$$

In these formulas, TP indicates true positive, TN represents true negative, FP is false positive, and FN signifies false negative.

Considering that the randomness of the initial parameters of the neural network may cause fluctuations

in the prediction results and lead to potential large deviations, this study conducted a 100-cycle Monte Carlo test to systematically evaluate the effectiveness and robustness of the ALO–SOM model. By introducing key hyperparameter perturbations, the stability of the model's earthquake identification performance under parameter variations was tested. The training set and test set were strictly split in an 8:2 ratio (i.e., 331:83 samples). The statistical characteristics of the repeatability test results are presented in Figures 4 and 5, Table 1.

Figure 5 presents a box plot comparing the 100 identification results of the ALO–SOM and SOM models, which simultaneously illustrates the data dispersion and statistical characteristics of the multiple rounds of prediction results from the two neural network models. The upper and lower boundaries of the box in the figure represent the upper quartile (Q3) and lower quartile (Q1) of the parameter results, respectively. The solid line inside the box indicates the median of the parameter results. Data points marked with red triangles are identified as outliers in the box plot. The horizontal solid lines above and below the box represent the maximum and minimum values, respectively. The performance difference between the ALO–SOM and SOM models was analyzed using parameters, such as the mean, SD, range, CV, and interquartile range (IQR).

Based on Figure 5, the recognition curve of the SOM model exhibits irregular oscillations, with approximately 50% of the recognition results below 97%, and a small number even below 90%, indicating a degree of instability in earthquake and explosion recognition. The SOM model optimized by ALO demonstrates stronger adaptability to data features and can effectively utilize matching competition layer dimensions and training iterations to recognize earthquakes and explosions. The worst result is above 95%, and most recognition results exceed 99%. Its performance across multiple indicators—mean, SD, range, CV, and IQR (99.3373%, 1.1662, 4.8193, 0.0117, and 1.2048, respectively)—demonstrates stronger robustness and accuracy.

Figure 4 presents a box plot of the calculation results for the ALO-optimized SOM hyperparameter values across 100 identification sub-tests. The search domain was set to [1,10,] which illustrates both the data dispersion and statistical characteristics of the 100 optimization results for the two SOM hyperparameters. The upper and lower boundaries of the box in the figure represent the upper quartile (Q3) and lower quartile (Q1) of the parameter results, respectively. The solid line within the box represents the median of the parameter results. The horizontal solid lines above and below the box indicate the maximum and minimum values, respectively. As shown in Figure 4, the SOM competition layer dimension and SOM training iterations optimized by ALO exhibit a certain degree of randomness and are not consistently stable values. This variability is related to the random division of the training set and the early termination of ALO iterations.

Table 1 presents the statistical results of the 100 comparison tests between the ALO–SOM model and the traditional SOM model. The results indicate that the ALO–SOM model outperforms the SOM model in all indicators, exhibiting higher accuracy and stability. Specifically, the average accuracy of the ALO–SOM model over 100 prediction rounds was 99.3373%, significantly higher than that of the SOM model (96.5904%), suggesting that the ALO–SOM model can provide more accurate results in earthquake identification tasks, with an accuracy improvement of 2.7469%.

In addition, the SD of the 100-round prediction accuracy for the ALO–SOM model was 1.1662, significantly lower than that of the SOM model (SD = 1.9303), indicating that its prediction results exhibit lower variability and higher stability, making it suitable for processing earthquake monitoring data that requires highly reliable results. Furthermore, the IQR of the ALO–SOM model's 100-round prediction accuracy was 4.8193, which is also significantly smaller than that of the SOM model (IQR = 10.8434), further suggesting that the ALO–SOM model's prediction results are more concentrated and less influenced by extreme values, thereby demonstrating better robustness. The CV and IQR of the ALO–SOM model highlight its superiority in prediction result consistency, with a CV of 0.0117 for ALO–SOM and 0.0200 for SOM, and an IQR of 1.2048 for ALO–SOM and 2.4096 for SOM.

To evaluate the superior performance of the ALO–SOM model and the differences in performance between machine learning algorithms based on different principles, we introduced six classic models: linear discriminant analysis (LDA), decision tree, SVM, probabilistic LDA (PLDA), convolutional neural network (CNN), and AdaBoost ensemble learning. These models have distinct strengths and weaknesses. For example, SVM is effective in handling non-linear problems but is sensitive to noisy data and outliers; LDA is suitable for large-scale linear datasets but may encounter singularity issues in the inter-class covariance matrix; AdaBoost has moderate tolerance for noise and outliers but is prone to overfitting; and decision tree models are highly interpretable but are still prone to overfitting and sensitive to outliers. The parameters for this model comparison experiment were kept constant, with 100 consecutive recognition tests conducted using a fixed training-to-test set ratio of 8:2. The comparison results are presented in Table 2 and Figure 6.

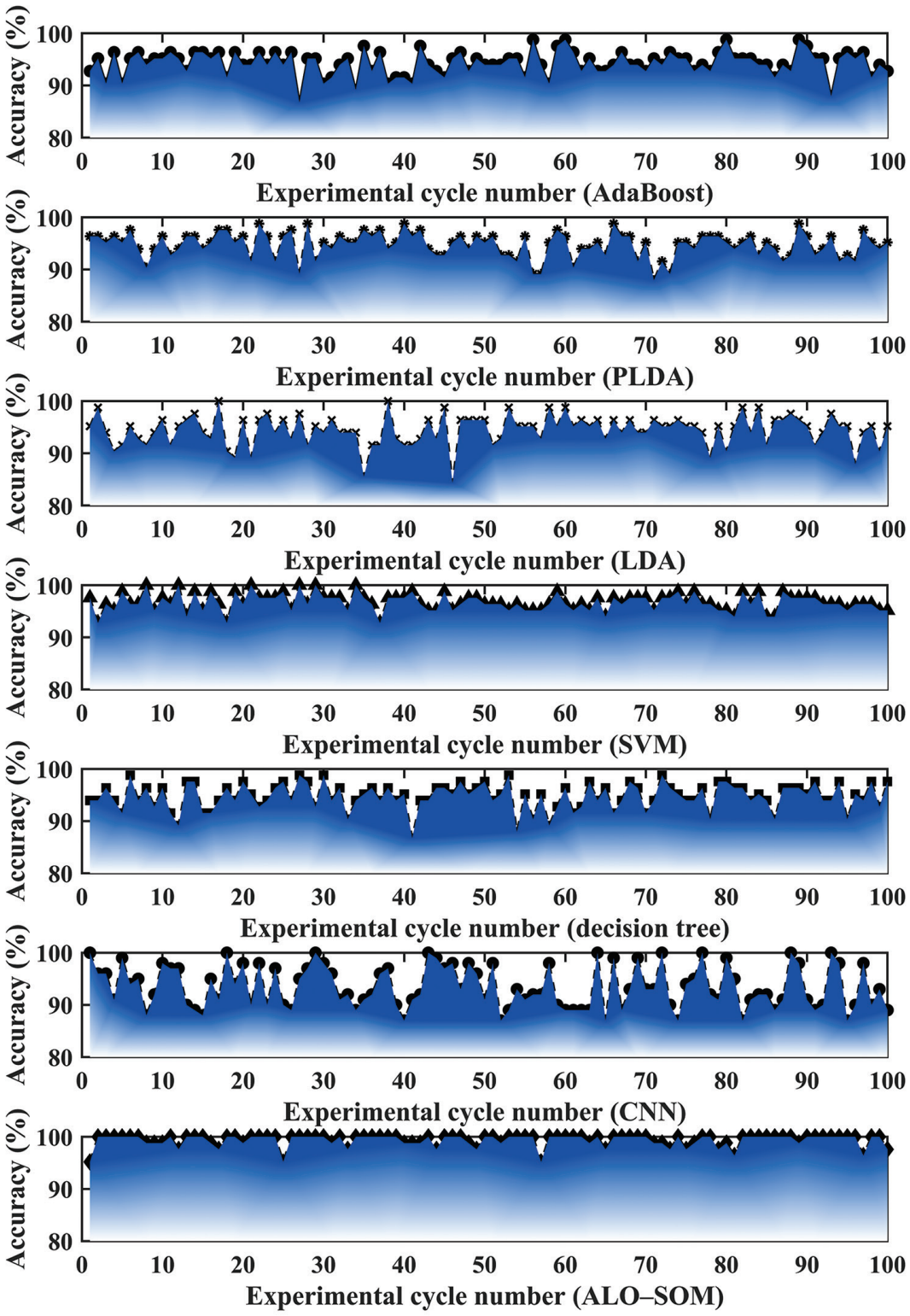

Figure 6. Comparison of seismic wave prediction performance across 100 rounds by six machine learning models.
Abbreviations: ALO: Ant Lion Optimization; CNN: Convolutional neural network; LDA: Linear discriminant analysis; PLDA: Probabilistic linear discriminant analysis; SOM: Self-organizing map; SVM: Support vector machine.

As shown in Figure 6 and Table 2, the earthquake and explosion signal recognition performance (in terms of accuracy, recall rate, and F1-score) of the ALO–SOM model was significantly better than that of classic machine learning models, including LDA, decision tree, SVM, PLDA, CNN, and AdaBoost, with all metrics exceeding 99%. This demonstrates that the model has potential applicability in small-sample earthquake event classification and offers room for further research and improvement.

To calculate the recognition accuracy of the ALO–SOM model for small-sample events, such as blast events, we employed MATLAB interpolation and resampling techniques to increase the number of blast signals from 117 to 351, while maintaining the number of natural signals at 297. The sampling rate remained at 200 Hz, resulting in a total of 648 signals used in the subsequent recognition experiments. The training-to-test set ratio was set to 8:2 (i.e., 518:130). The experimental results are illustrated in Figure 7.

Under resampling conditions, the average recognition accuracy of the ALO–SOM model over 100 prediction rounds was 99.2308%, with an SD of 0.6468, which was essentially equivalent to the recognition performance of the original experiment without resampling blast events. In addition, it was found that the mean recognition accuracy rates for both seismic and blast signals improved compared to previous results, reaching 99.5923% and 99.6385%, respectively. The SDs for accuracy rates were 0.5729 and 0.5295 for seismic and blast signals, respectively, indicating that the ALO–SOM model demonstrates good recognition performance for both seismic and blast signals in small-sample datasets.

5. Discussion

This study proposes a new hybrid model, combining CEEMDAN–MDE and ALO–SOM, for high-precision discrimination of seismic and blast signals. Experimental results showed that the model achieved excellent performance, with an accuracy of 99.337%, a recall of 99.148%, and an F1-score of 99.456%—significantly better than those of traditional machine learning methods, such as LDA, decision tree, SVM, PLDA, and AdaBoost. The combination of MDE feature extraction based on CEEMDAN and the SOM neural network optimized by ALO effectively addresses the problems of insufficient feature expression and insufficient model stability in seismic signal classification.

The practical significance of this study is that the CEEMDAN–MDE feature set provides a standardized framework for quantifying the complexity of seismic signals,

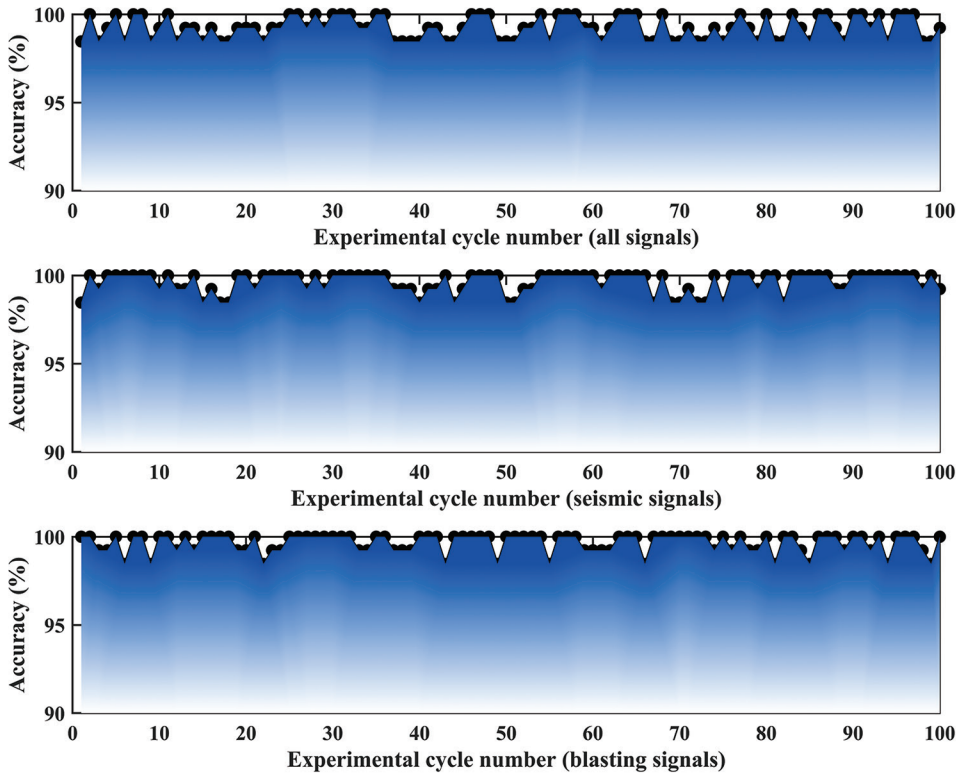

Figure 7. Seismic identification results of the Ant Lion Optimization–self-organizing map model under resampling conditions.

which can be extended to other waveform classification tasks (e.g., volcanic earthquakes, industrial vibrations). The stability and interpretability of the ALO–SOM model make it suitable for deployment in seismic monitoring systems, especially in scenarios requiring rapid discrimination between natural and man-made events (e.g., nuclear test monitoring, mine safety assessment). The high recall of the model (99.148%) is particularly important for reducing false negatives in early warning systems.

Despite the strengths of this study, several limitations remain. First, the dataset, although carefully curated, comprises 414 samples from specific regions (e.g., Jiangsu, Yunnan), which may limit the generalizability of the model in different geological environments. Second, environmental noise (e.g., wind, traffic) is not explicitly simulated, which may affect the model's performance in noisy, real-world environments. Third, the computational cost of CEEMDAN–MDE feature extraction and ALO optimization, while justified by improved accuracy, may hinder real-time applications on low-power edge devices. Finally, the model relies on all 12 initial functions (IMFs), and no feature selection was performed, which may introduce redundancy—methods, such as wrapper-based selection could simplify this process.

Future research should focus on: (i) expanding the dataset to cover global earthquake events and diverse noise conditions to enhance model robustness; (ii) exploring lightweight variants of CEEMDAN (e.g., online CEEMDAN) and entropy metrics (e.g., fuzzy entropy) to enable real-time deployment; (iii) integrating attention mechanisms or Transformer architectures to enhance feature learning; (iv) studying hybrid models that combine ALO–SOM with ensemble techniques (e.g., stacking) to address the class imbalance problem in rare event detection. In addition, applying this framework to other geophysical signal classification tasks (e.g., landslide vibration, structural health monitoring) would help verify its broader practicality.

In summary, the CEEMDAN–MDE–ALO–SOM model represents a significant advancement in the field of earthquake signal recognition, providing both theoretical innovation and practical value. Addressing its limitations through collaborative data sharing and algorithmic improvements will be key to advancing earthquake monitoring technology.

6. Conclusion

The accurate distinction between natural earthquake signals and artificial explosion signals is crucial to ensuring the reliability of earthquake early warning information release and advancing artificial intelligence-based seismology research. Based on small-sample data from multiple seismic stations across the country, this study extracted MDE features from the 12-dimensional CEEMDAN spectrum decomposition of normalized seismic wave signal, employed the SOM self-organizing feature mapping network as the basic learner, and combined the ALO algorithm to optimally tune its competition layer dimensions and training iterations, thereby improving the recognition accuracy and operational stability of the original model. Accordingly, the following conclusions are drawn:

(i) Compared with the standard SOM neural network model, LDA, decision tree, SVM, PLDA, AdaBoost ensemble learning, and other commonly used machine learning models, the ALO–SOM model achieved significantly higher earthquake and explosion recognition accuracy, with a recognition rate of 99.3373% and an SD of only 1.1662.

(ii) The multiscale spectrum feature set CEEMDAN–DisEn, which contains the IMF component DistEn values of different frequency bands, demonstrated a stronger capability for subdividing seismic wave features.

(iii) Several limitations remain in this study. First, a large amount of environmental noise may mask the effective components of seismic waves, thereby affecting the accuracy of waveform spectrum feature extraction. Second, this study used all 12-dimensional IMF components obtained by CEEMDAN decomposition for feature extraction without applying feature selection or high-dimensional data compression, which could reduce prediction efficiency and cause some loss of accuracy. If feature selection methods, such as filtering, encapsulation, and embedding, or dimension reduction methods—such as principal component analysis and low-variance filtering—were applied for feature processing, the accuracy of distinguishing between earthquakes and explosions could be further improved, while moderately reducing algorithm redundancy and iteration time. Therefore, future studies are encouraged to integrate principal component analysis to perform feature engineering compression on all IMF components from CEEMDAN, producing 2–3 new features that best represent the multiscale characteristics of seismic waveforms. This would reduce the complexity of the input matrix for the prediction model, thereby improving model training speed and prediction efficiency. Finally, due to the model's outstanding unsupervised clustering performance, it could be applied to the fault diagnosis of seismic instrument systems in the future, accurately distinguishing between data acquisition faults, power

supply faults, electromagnetic interference, and other abnormal signals, thus ensuring the effective recording and observation of environmental noise data and seismic event signals by seismic instruments.

Acknowledgments

We thank the Institute of Engineering Mechanics of China Earthquake Administration (National Earthquake Science Data Center) and the Institute of Geotechnical Engineering, China Institute of Water Resources and Hydropower Research, for providing the data support for this study.

Funding

This research was financially supported by Wuhan Gravitation and Solid Earth Tides, National Observation and Research Station Open Fund Project (No. WHYWZ202406, WHYWZ202208); the Scientific Research Fund of Institute of Seismology, CEA and National Institute of Natural Hazards, MEM (No. IS202236328, IS202436357); the Spark Program of Earthquake Technology of CEA (No. XH24025YC); the Earthquake Monitoring and Forecasting and Early Warning Tasks for 2025 (No. CEA-JCYJ-202502015); Chengdu Jincheng College Green Data Integration Intelligence Research and Innovation Project (No. 2025-2027); and the High-Quality Development Research Center Project in the Tuojiang River Basin (No. TJGZL2024-07).

Conflict of interest

The authors declare they have no competing interests.

Author contributions

Conceptualization: Cong Pang, Tianwen Zhao, Ailing Wang

Formal analysis: Cong Pang, Guoqing Chen, Tianwen Zhao, Ailing Wang

Investigation: Tianwen Zhao, Chawei Li, Ailing Wang

Methodology: Cong Pang, Tianwen Zhao, Guoqing Chen, Chawei Li

Writing – original draft: Cong Pang, Tianwen Zhao, Guoqing Chen, Ailing Wang

Writing – review & editing: Cong Pang, Tianwen Zhao, Guoqing Chen, Ailing Wang

Availability of data

This study integrates 1,000 sets of strong earthquake observation data and explosion data from regions in and around China, primarily sourced from publicly available earthquake case data provided by the National Earthquake Data Center (data.earthquake.cn), the Institute of Engineering Mechanics, China Earthquake Administration, and the China Institute of Water Resources and Hydropower Research.

References

1. Lythgoe K, Loasby A, Hidayat D, Wei S. Seismic event detection in urban Singapore using a nodal array and frequency domain array detector: Earthquakes, blasts, and thunder quakes. *Geophys J Int*. 2021;226(3):1542-1557.

   doi: 10.1093/gji/ggab135

2. Reynen A, Audet P. Supervised machine learning on a network scale: Application to seismic event classification and detection. *Geophys J Int*. 2017;210(3):1394-1409.

   doi: 10.1093/gji/ggx238

3. Abdalzaher MS, Krichen M, Moustafa SS, Alswailim M. Using Machine Learning for Earthquakes and Quarry Blasts Discrimination. In*: 20th ACS/IEEE International Conference on Computer Systems and Applications (AICCSA)*; 2023. p. 1-6.

   doi: 10.1109/AICCSA59173.2023.10479234

4. Zheng B, Huang H, Wang T, Feng Z, Wei C. Real-Time Classification Study of Natural Earthquake and Artificial Blasting Waveforms Based on QRCN. In: 6th *International Conference on Communications, Information System and Computer Engineering* (*CISCE*); 2024. p. 449-454.

   doi: 10.1109/cisce62493.2024.10653243

5. Liu J, Zheng SH, Kang Y, Chou YQ. The focal mechanism determinations of moderate-small earthquakes using the first motion and amplitude ratio of P and S wave. *Earthquake*. 2004;24(1):19-26.

6. Wang Y, Tang F, Jiang X. Seismogenic structure of the earthquake surface rupture zone along the Maisu fault. *Acta Seismol Sin*. 2024;46(5):751-766.

   doi: 10.11939/jass.20220225

7. Zhang H, Zhang R, Zhao YG. Novel approach for energy-spectrum-based probabilistic seismic hazard analysis in regions with limited strong earthquake data. *Earthq Spectra*. 2024;40(4):2692-2711.

   doi: 10.1177/87552930241263621

8. Liu W, Qian Y, Wei X, Song W, Chen X. A wavelet-domain seismic source inversion method for submarine earthquakes based on 3-D Green's functions. *IEEE Trans Geosci Remote Sens*. 2024;62:1-16.

   doi: 10.1109/TGRS.2024.3434388

9. Lin T, Cheng J, Chen Q, Cui S. Wavelet transform-based fuzzy clustering microseismic first-arrival picking method. *IEEE Access*. 2023;11:136978-136987.

   doi: 10.1109/ACCESS.2023.3338628

10. Chen C, Wang CH, Liu JY, *et al*. Identification of earthquake

signals from groundwater level records using the HHT method. *Geophys J Int*. 2010;180(3):1231-1241.

doi: 10.1111/j.1365-246X.2009.04473.x

11. Wang YH, Liang SF, Kuo TBJ, Lin YC. Software implementation of real-time EMD-based algorithm in embedded microprocessors for wearable devices. *IEEE Trans Instrum Meas*. 2024;73:1-10.

doi: 10.1109/TIM.2024.3450102

12. Chen T, Gao S, Zheng S, *et al*. EMD and VMD empowered deep learning for radio modulation recognition. *IEEE Trans Cogn Commun Netw*. 2023;9(1):43-57.

doi: 10.1109/TCCN.2022.3218694

13. Shen W, Ding H. Observation of spheroidal normal mode multiplets below 1 mHz using ensemble empirical mode decomposition. *Geophys J Int*. 2013;196(3):1631-1642.

doi: 10.1093/gji/ggt468

14. Zhou H, Jian X,Chen S, *et al*. Leakage current de-disturbance method for distribution network type surge arrester based on EEMD-SVD and low-rank RBF neural network. *IEEE Access.* 2024;12:52097-52109.

doi: 10.1109/access.2024.3387327

15. Wu J, Wang W, Shang T, Cao J. A novel series arc fault detection method based on CEEMDAN and IFAW-1DCNN. *IEEE Trans Dielectr Electr Insul*. 2024;31(2):1020-1029.

doi: 10.1109/TDEI.2024.3360222

16. Shi LF, Zhou W, Yan X, Shi Y. Novel step detection algorithm for smartphone indoor localization based on CEEMDAN-HT. *IEEE Trans Instrum Meas.* 2024;73:1-9.

doi: 10.1109/TIM.2024.3472810

17. Pradhan SK, Chakraborty B. State of health estimation of Li-ion batteries based on sample entropy and various regression techniques. *Ionics*. 2025;31(5):4209-4225.

doi: 10.1007/s11581-025-06213-4

18. Cheraghy M, Soltanpour M, Abdalla HB, Oveis AH. SVM-based factor graph design for max-SR problem of SCMA networks. *IEEE Commun Lett.* 2024;28(4):877-881.

doi: 10.1109/lcomm.2024.3366426

19. Ren K, Zou G, Zhang S, Peng S, Gong F, Liu Y. Fault identification and reliability evaluation using an SVM model based on 3-D seismic data volume. *Geophys J Int.* 2023;234(1):755-768.

doi: 10.1093/gji/ggad095

20. Zhao G, Huang H, Lu X. Discriminating Earthquakes and Explosion Events by Seismic Signals Basing on BP-Adaboost Classifier. In: *2nd IEEE International Conference on Computer Communications (ICCC)*; 2016. p. 1965-1969.

doi: 10.1109/CompComm.2016.7925045

21. Bicego M, Cicalese F, Mensi A. RatioRF: A novel measure for random forest clustering based on the Tversky's ratio model. *IEEE Trans Knowl Data Eng*. 2023;35(1):830-841.

doi: 10.1109/tkde.2021.3086147

22. Amos AJ, Lee K, Gupta TS, Malau-Aduli BS. Validating the knowledge represented by a self-organizing map with an expert-derived knowledge structure. *BMC Med Educ*. 2024;24(416):416.

doi: 10.1186/s12909-024-05352-y

23. Liu Z, Cao J, Lu Y, Zhou P, Hu J. A hierarchical clustering method of SOM based on DTW distance for variable-length seismic waveform. *IEEE Geosci Remote Sens Lett*. 2022;19:1-5.

doi: 10.1109/LGRS.2021.3105476

24. Liu Z, Cao J, Chen S, Lu Y, Tan F. Visualization analysis of seismic facies based on deep embedded SOM. *IEEE Geosci Remote Sens Lett*. 2021;18(8):1491-1495.

doi: 10.1109/lgrs.2020.3003585

25. Chen S, Liu Z, Zhou H, Wen X, Xue Y. Seismic facies visualization analysis method of SOM corrected by uniform manifold approximation and projection. *IEEE Geosci Remote Sens Lett*. 2023;20:1-5.

doi: 10.1109/LGRS.2023.3260105

26. Dhanaraj RK, Chandraprabha M. Ant lion optimization in deep neural network for forecasting the rice crop yield based on soil nutrients. *Prog Artif Intell*. 2025;14(1):101-116.

doi: 10.1007/s13748-024-00351-y

27. Altawil IA, Mahafzah KA, Almomani A. A grid connected hybrid renewable energy system for optimal energy management based on ant-lion optimization algorithm. *J Theor Appl Inf Technol*. 2023;101(1):114-122.

28. Udhayakumar R, Karmakar C, Li P, Wang X, Palaniswami M. Modified distribution entropy as a complexity measure of heart rate variability (HRV) signal. *Entropy*. 2020;22(10):1077.

doi: 10.3390/e22101077

29. Wang Z, Gong M, Li P, Gu J,Tian W. A hypervolume distribution entropy guided computation resource allocation mechanism for the multiobjective evolutionary algorithm based on decomposition. *Appl Soft Comput*. 2021;116:108297.

doi: 10.1016/j.asoc.2021.108297

30. Saini A, Rahi OP. Optimal power flow analysis including stochastic renewable energy sources using modified ant lion optimization algorithm. *Wind Eng*. 2023;47(5):947-972.

doi: 10.1177/0309524X231169295

31. Mirjalili SZ, Saremi S, Mirjalili SM. Designing evolutionary feedforward neural networks using social spider optimization algorithm. *Neural Comput Appl*. 2015;26(8):1919-1928.

doi: 10.1007/s00521-015-1847-6

ACCSCIENCE PUBLISHING

Journal of Seismic Exploration

ARTICLE

Seismic signal denoising using variational mode decomposition and a denoising convolutional neural network

Shengrong Zhang[1,2], Liang Zhang[1]*, and Xuesha Qin[3]

[1]The Key Laboratory of Advanced Manufacturing Technology of the Ministry of Education, Guizhou University, Guiyang, Guizhou, China

[2]School of Computer and Electronics Information, Guangxi University, Nanning, Guangxi, China

[3]China-ASEAN School of Economics, Guangxi University, Nanning, Guangxi, China

Abstract

Effectively recovering signals buried in noise remains a challenging topic in seismic data denoising. Many conventional methods often fail to accurately capture the characteristics of seismic signals. To address this issue, this study proposed an effective method called variational mode decomposition (VMD)–denoising convolutional neural network (DnCNN). The method first applies VMD to decompose the originally noisy signal into multiple intrinsic mode functions (IMFs) with band-pass characteristics, thereby achieving effective decoupling of different frequency components and noise separation. Selected IMFs are then combined into a multi-channel input and fed into the DnCNN for end-to-end modeling and denoising reconstruction. By decomposing the noisy signal into IMFs corresponding to specific frequency bands and learning them through DnCNN, the network can better extract features within each frequency band. Serving as a front-end filter, the VMD module enhances the network's ability to represent effective frequency components, suppresses high-frequency random noise, and improves the resolution of weak signals. Experimental results demonstrated that the proposed method effectively captures signal characteristics and recovers signals from both real and synthetic seismic data. In conclusion, the proposed VMD–DnCNN method provides a robust and efficient solution for seismic signal denoising.

Keywords: Variational mode decomposition; Denoising convolutional neural network; Intrinsic mode functions; Recover weak signals; Seismic denoising

***Corresponding author:**
Liang Zhang
(liangzhang@gzu.edu.cn)

Citation: Zhang S, Zhang L, Qin X. Seismic signal denoising using variational mode decomposition and a denoising convolutional neural network. *J Seismic Explor*. 2025;34(2):44-59.
doi: 10.36922/JSE025260030

Received: June 29, 2025

Revised: August 12, 2025

Accepted: August 13, 2025

Published online: September 4, 2025

1. Introduction

Seismic signals are often characterized by non-stationary properties and are susceptible to various external interferences during acquisition, such as complex mixed noise caused by exploration instruments, wind, and transportation activities.[1,2] These types of noise can significantly degrade the quality of subsequent imaging and interpretation processes. To better extract geological information from seismic data, it is crucial to effectively isolate signals from noise. Moreover, the accurate recovery of weak signals can further enhance geological exploration efforts.[3-5] Therefore, many researchers have investigated

effective seismic signal recovery under low signal-to-noise ratio (SNR) conditions.[6] Currently, denoising methods can be broadly categorized into four groups: Time–frequency analysis methods, decomposition-based methods, low-rank-based methods, and deep learning methods.

Time–frequency analysis methods aim to exploit the differences in time–frequency distributions between useful seismic reflections and noise. By applying time–frequency transformations, seismic data can be represented in a joint time–frequency domain, enabling the separation and suppression of noise from signal components. For example, the wavelet transform[7] achieves denoising by decomposing the signal into different frequency bands, retaining the dominant frequency components associated with the signal while removing high-frequency components typically attributed to noise. The short-time Fourier transform[8] utilizes its localized time–frequency resolution to expand non-stationary seismic signals in the time–frequency domain, allowing for clearer distinction between signal and noise. Likewise, the S-transform[9] constructs a two-dimensional time–frequency representation and leverages the seismic signal's concentration and continuity in local frequency content to facilitate signal–noise separation. However, these methods often suffer from difficulties in identifying optimal basis functions and are highly sensitive to thresholding strategies. The performance of these approaches is strongly dependent on the threshold level and the specific selection scheme, where improper thresholds may lead to significant degradation in denoising quality and signal preservation. These limitations are not unique to the aforementioned methods, but are also observed in other time–frequency analysis techniques, such as the seislet transform,[10] curvelet transform,[11] and contourlet transform.[12]

Decomposition-based methods aim to extract intrinsic structures from noisy signals by separating effective components from noise interference and subsequently reconstructing the denoised seismic signal. For example, empirical mode decomposition[13,14] is an adaptive and data-driven technique for processing non-stationary signals. It decomposes the original signal into a set of intrinsic mode functions (IMFs) with localized time-frequency characteristics. By analyzing the frequency and energy features of each component, noise-dominated modes can be identified and discarded, followed by signal reconstruction for denoising. Variational mode decomposition (VMD)[15] formulates a variational optimization problem to decompose the original signal into a set of band-limited sub-signals (mode components). Noise-dominated components are recognized and removed based on their frequency and energy characteristics, achieving efficient denoising. On the other hand, singular value decomposition[16] decomposes the seismic data matrix into ordered components according to their energy. Principal components represent the effective signal, while low-energy components correspond to noise, and denoising is performed through reconstruction. The major challenge of decomposition-based methods lies in the mode mixing phenomenon, where certain modes contain both noise and signal components, complicating their separation.

Low-rank-based methods exploit the strong structural properties of seismic noise signals in time and space domains. When arranged as matrices or tensors, seismic signals typically exhibit low-rank characteristics, whereas noise is random and high-rank. Low-rank decomposition techniques can therefore extract the structured signal components while suppressing high-rank noise. For example, principal component analysis[17] projects seismic data onto a set of principal components, retaining the first few components that contain the main information and discarding the subsequent minor components, thus achieving denoising. Cadzow filtering[18] constructs a Hankel matrix from the signal and iteratively applies singular value decomposition, low-rank approximation, and Hankel structure reconstruction to preserve the primary signal components while suppressing noise. Both methods treat the effective signal as a low-rank structure and extract meaningful cycles by reducing the rank. However, a notable limitation of these approaches is that their performance heavily depends on the prior assumptions regarding the rank.

Deep learning methods[19,20] essentially construct end-to-end mapping functions that automatically learn the relationship between noisy and clean signals, thereby achieving noise suppression and signal recovery. Previous studies have systematically demonstrated how neural networks can be applied to seismic signal denoising, successfully employing deep learning for this purpose.[21] For example, edge-feature-guided wavelet U-Net[22] integrates wavelet transforms to design dual decoders aimed at edge detection, capturing shape and edge information of effective signals. Other studies introduced the representation of seismic data in the time–frequency domain as input to neural networks,[23] enabling the model to learn the characteristics of seismic signals in the time–frequency space more effectively, and proposed an identification-based denoising approach.[24] Noise locations are first identified, and then the network performs targeted denoising, thereby more accurately removing noise while avoiding the inadvertent removal of useful signals. Some transformer-based methods innovatively combined sparse channel-wise attention transformers with diffusion models through a seismic prior extraction network, achieving efficient and high-quality seismic data interpolation.[25]

In addition, a transformer-based seismic data denoising model has been introduced, incorporating a novel self-supervised pretraining strategy to effectively capture long-range dependencies and improve noise attenuation while preserving weak signals.[5] To enhance seismic data denoising performance, most methods involve modifications to neural network architectures; however, these improvements often come at the cost of increased computational time.

In summary, traditional seismic denoising methods often suffer from limitations related to performance and parameter tuning. Whether it is time–frequency methods, decomposition-based methods, or low-rank methods, parameter adjustments are typically required according to the noise intensity. A common challenge lies in how to properly decompose the signal in a way that removes noise while preserving the useful signal. This leads to these methods lacking adaptability to varying noise levels. For deep learning methods, when noise levels are excessively high, it is often difficult to effectively capture the characteristics of seismic signals. The construction of end-to-end mappings can introduce bias, resulting in poor learning of weak signals and consequently unsatisfactory denoising performance. Therefore, effectively addressing the limitations of these approaches constitutes a major challenge in seismic signal processing and is the central focus of this study.

Decomposition-based and deep learning-based methods each have their advantages and drawbacks. Deep learning methods can effectively handle non-Gaussian and nonlinear noise, whereas decomposition-based methods rely primarily on frequency decomposition and are less capable of adapting to complex background noise. Furthermore, these approaches can identify low-amplitude reflections that decomposition methods may mistakenly remove as noise, especially for weak high-frequency reflections. However, deep learning implicitly models frequency information and lacks explicit frequency band control. In contrast, decomposition-based methods explicitly separate different frequency bands, facilitating the removal of band-specific noise and improving the preservation of waveform structures, particularly the low-frequency primary components.

Motivated by the strong learning capabilities of deep learning models and the intrinsic decomposition principles, this study proposed a VMD–denoising convolutional neural network (DnCNN) framework. This approach leverages the advantages of deep learning models to compensate for the shortcomings of traditional methods, while utilizing the strengths of decomposition models to complement deep learning models' limitations. VMD effectively decomposes seismic data to extract intrinsic features, enabling DnCNN[26] to learn the characteristics of different IMFs more effectively. Through training, DnCNN can mitigate the mode mixing problem inherent in VMD by continuously learning which IMFs are useful and which should be discarded. Experiments conducted on both synthetic and field seismic data demonstrated that this method not only effectively suppresses noise but also outperforms several traditional denoising techniques in terms of denoising performance.

2. Methods

In decomposition-based methods, mode mixing often occurs, resulting in decomposed modes that may contain noise components, which is unavoidable. Whether the decomposition extracts components from high frequency to low frequency, optimizes for band-limited signals so that each mode concentrates on a specific frequency band, or employs other decomposition techniques, it is essentially impossible to prevent noise from being introduced into the decomposed components. However, deep learning networks possess strong learning capabilities and can progressively distinguish between noise and useful signals through continuous training. Therefore, deep learning networks were combined with traditional methods to form a VMD–DnCNN denoising architecture.

Seismic signals are often represented as seismic profiles. Let the function $c(x, y)$ denotes the ideal noise-free signal and $n(x, y)$ represents the noise component, where x is the sampling time and y is the trace number. The observed noisy data can then be expressed as:

$$f(x,y) = c(x,y) + n(x,y) \tag{I}$$

The 2D VMD method was applied to decompose the noisy seismic data. The formulation of 2D VMD is as follows:

$$\min_{u_k,\omega_k} \sum_{k=1}^{K} \| \nabla \left(u_k(x,y) \cdot e^{-j\omega_k x} \right) \|_2^2, \; s.t. \sum_{k=1}^{K} u_k(x,y) = f(x,y) \tag{II}$$

$$f(x,y) = \sum_{k=1}^{3} u_k(x,y) \tag{III}$$

where, $u_k(x, y)$ denotes the K decomposed mode, ω_k is its center frequency along the x direction, and ∇ represents the two-dimensional gradient operator, which measures the smoothness or bandwidth of the mode in the frequency domain. The term $e^{-j\omega_k x}$ performs a frequency shift of the mode to concentrate it around the low-frequency baseband, facilitating a unified calculation of the mode's bandwidth.

After decomposing the signal into three modes based on bandwidth, these modes were combined with the

original signal as a four-channel data input to the network, allowing the deep learning model to learn the process of reconstructing the original signal from the three modes during training. By decomposing the data through VMD, different band-limited signal components were formed, significantly reducing the learning burden on the deep learning network. Compared to the original single-channel structure, where only noisy data are input to the network, this approach alleviates the heavy learning load and makes it easier for the network to capture features of both the seismic signal and noise.

When inputting the decomposed modes into the network, the model first learns the characteristics of different frequency bands. Furthermore, since the primary noise frequency bands have already been separated through decomposition, the network can more readily identify the main noise components during training. Even when non-noise dominant frequency bands are mixed with some noise, the network can leverage the features learned from the noise-dominant bands to recognize and denoise these components effectively. Moreover, effective signal information may also be present within the primary noise frequency bands. In this case, the useful signal features learned from the non-noise-dominant bands help the network capture and preserve valid signal components within the noise-dominant bands.

As a denoising network, DnCNN has been widely used for processing seismic signals. The architecture of DnCNN is illustrated in Figure 1. The network first passes the input through a convolutional layer, followed by a rectified linear unit (ReLU) activation function. Sixty-four convolutional kernels are used to extract preliminary low-level seismic features, including local waveform shapes, edges, and frequency components. The ReLU activation enhances the nonlinear representation capability, helping to distinguish seismic signal structures from high-frequency noise. The middle part of the network consists of 18 repeated blocks, each comprising a convolutional layer, batch normalization, and a ReLU activation. Batch normalization balances feature distributions across different batches, suppressing outliers. Through these 18 repeated operations, the network progressively extracts abstract seismic features, enabling it to ignore unstructured noise while preserving waveforms with reflective patterns. Finally, the output passes through a convolutional layer that compresses the 64 deep feature channels back to the original channel number, yielding the final denoised result.

The input structure of DnCNN was modified to better enable it to learn seismic signal information. By applying VMD to decompose noisy signals, the noise is separated into three modal components: High-frequency IMF, mid-frequency IMF, and low-frequency IMF. These three modes approximately correspond to high-, mid-, and low-frequency seismic phases and noise structures, facilitating the network's ability to distinguish and process noise in different frequency bands. Each of the three IMFs from VMD concentrates around a certain center frequency, which is dynamically adjusted during iterations to ensure each mode focuses on a specific frequency band.

In practice, IMF1 captures high-frequency details, often containing seismic noise and sharp reflections; IMF2 captures mid-frequency seismic phases, which include seismic signals but may also contain noise; IMF3 corresponds to low-frequency main structures, encompassing the primary seismic phases and reflection interfaces. Thus, decomposing the seismic signal into these three frequency bands effectively separates high-frequency disturbances, mid-frequency seismic phases, and low-frequency structural components.

The overall denoising process is illustrated in Figure 2. The VMD–DnCNN denoising procedure consists of two steps: The first step is model training, and the second step is seismic data denoising. In the first step, the selected synthetic data are segmented by time windows, followed by data selection using a Monte Carlo strategy. This produces the training labels for the network. Gaussian noise is then added to the labels to generate the noisy samples. These samples are decomposed using 2D VMD into three IMFs, which serve as the channels of the input samples. Subsequently, the time-domain channels of the labels are concatenated with the IMF channels of the

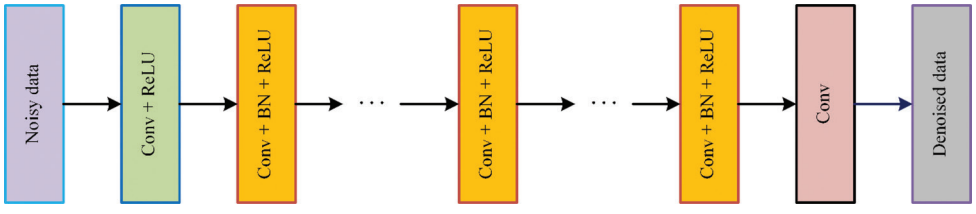

Figure 1. Structure of a denoising convolutional neural network.
Abbreviations: BN: Batch normalization; Conv: Convolutional layer; ReLU: Rectified linear unit.

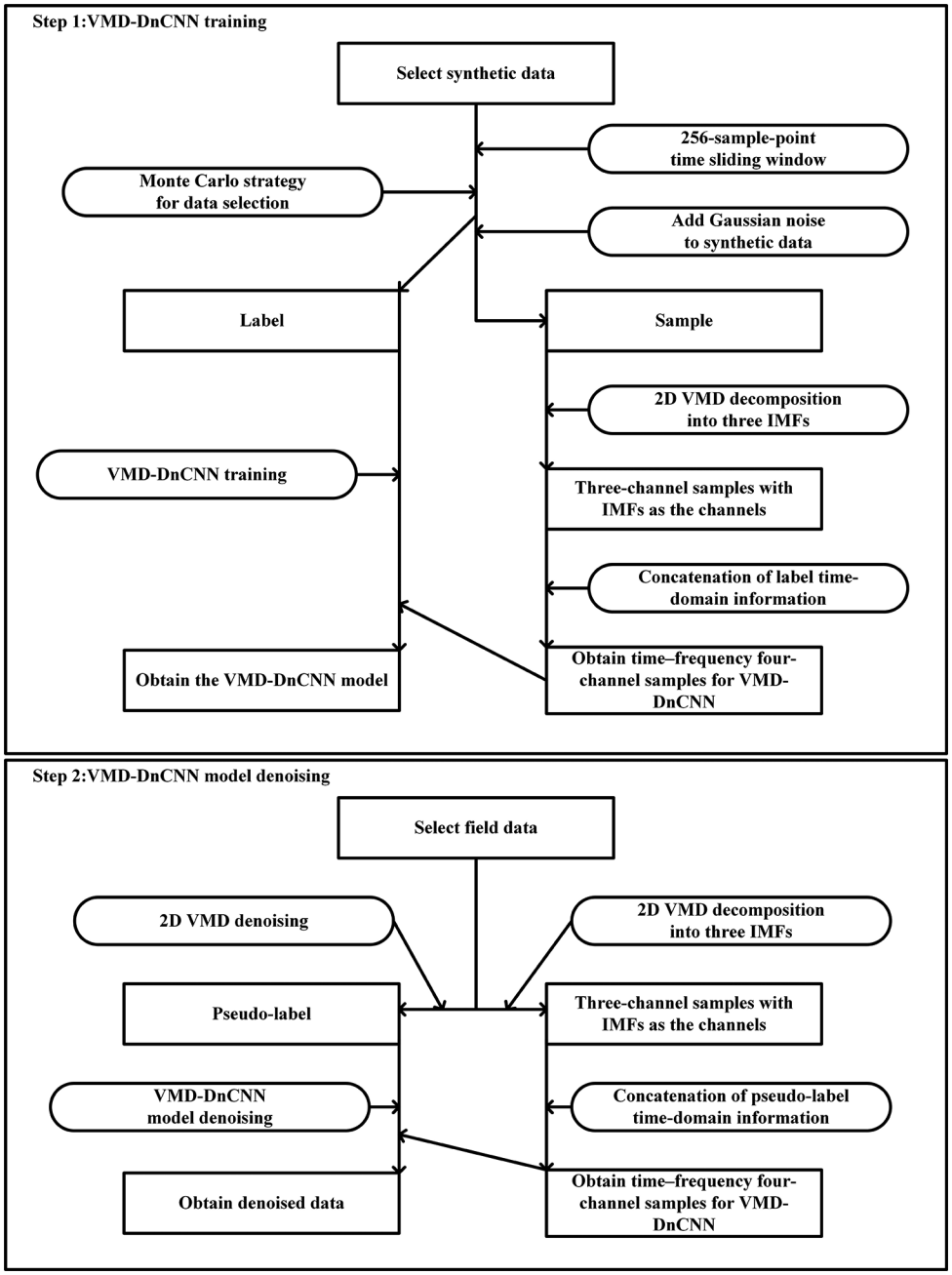

Figure 2. Main workflow of the proposed method.
Abbreviations: DnCNN: Denoising convolutional neural network; IMF: Intrinsic mode function; VMD: Variational mode decomposition.

samples to form the final time–frequency training samples required by VMD–DnCNN. By training the network with these labels and samples, the final model is obtained. In the second step, the seismic data to be denoised are first processed by 2D VMD to obtain pseudo-labels and seismic data decomposed into three IMF modes. The pseudo-label's time-domain data and the three IMF modes are combined to form a four-channel seismic input. Finally, these data are denoised by the trained VMD–DnCNN model.

3. Network training

The performance of neural network models is highly dependent on the quality of the training dataset; therefore, constructing a high-quality dataset and applying proper preprocessing are particularly critical. Given that the recordings before the onset of direct waves primarily consist of background noise without useful seismic information, this study removed certain non-informative data during

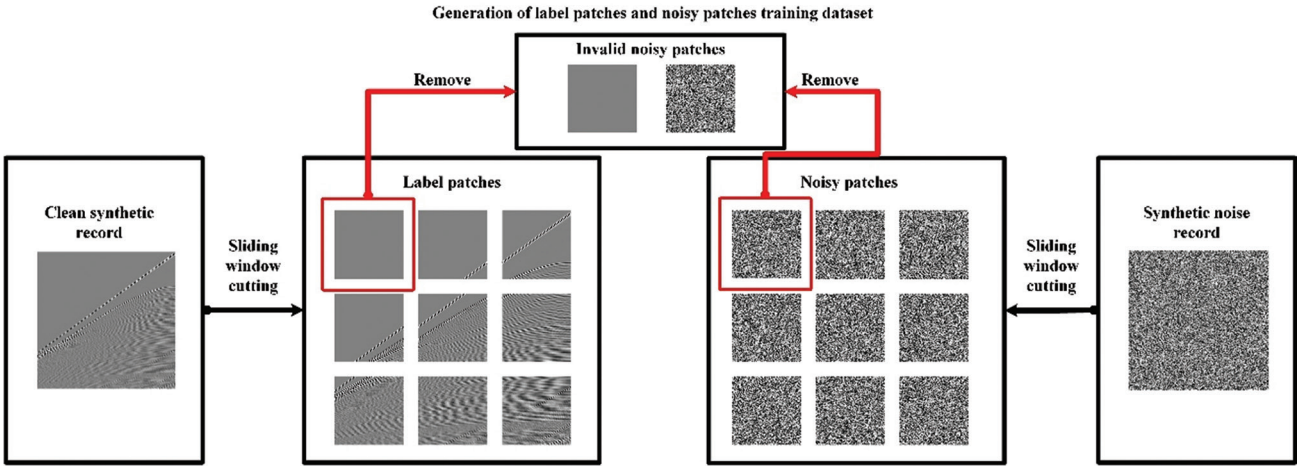

Figure 3. Training dataset generation process.

the preprocessing stage to enhance training efficiency. The overall data generation process is illustrated in Figure 3. A Monte Carlo strategy[27] was adopted to eliminate invalid synthetic data, incorporating non-zero label filtering and effective fluctuation filtering mechanisms. Specifically, silent segments before the arrival of direct waves, smooth sections, and other training-irrelevant samples were excluded. Samples with zero-valued amplitudes were directly discarded, and samples with a standard deviation $<10^{-3}$ were also removed. After filtering, the data underwent Max–Abs normalization to standardize the seismic signal amplitude range to the interval [−1,1]. This normalization accelerates model convergence during training and ensures amplitude consistency across different traces and samples, thereby reducing model bias. The training parameters for all models are listed in Table 1. All models used the ADAM optimizer.[28] The sample length was set to 256 points, with one sample selected every 128 points. When the remaining trace length was less than 256 points, it was padded forward to meet the required length. The initial learning rate was set to 10^{-4} and decayed by a factor of 10 every 40 epochs. The total number of training epochs was set to 200.

The synthetic seismic data used for training was derived from the 2007 British Petroleum (BP) Anisotropic Velocity Benchmark, a two-dimensional synthetic dataset released by BP. The dataset consists of 1,641 shot gathers, each containing 800 seismic traces. Each trace has 1,151 sampling points, with a sampling rate of 125 Hz and a sampling interval of 8 ms, resulting in a trace duration of 9.208 s. Due to the similarity between adjacent shot gathers, a subset of 20 gathers was selected for training by sampling five consecutive shots every 500 gathers. Specifically, the selected training gathers were 1–5, 501–505, 1,001–1,005, and 1,501–1,505. Shot gathers 10, 510, 1,010, and 1,510 were used for denoising evaluation. This sampling strategy,

Table 1. Training parameters of convolutional neural network-based methods

Hyperparameter	DnCNN	U-Net	VMD–DnCNN
Optimizer	ADAM	ADAM	ADAM
Patch size	256	256	256
Batch size	100	100	100
Epoch	200	200	200
Learning rate range	$[10^{-4}, 10^{-7}]$	$[10^{-4}, 10^{-7}]$	$[10^{-4}, 10^{-7}]$
Input channels	1	1	4

Abbreviations: DnCNN: Denoising convolutional neural network; VMD: Variational mode decomposition.

which spans different and dispersed seismic environments, facilitates the model to learn more representative and generalizable feature representations. Gaussian noise with a mean of 0 and a standard deviation of 0.3921 was added to the synthetic data to simulate noisy conditions. According to the characteristics of the Gaussian distribution, 99.7% of the SNR values of the added noise lie within the range [−3,3]. A total of 98,900 samples were generated from the 20 shot gathers. For all models, 80% of the samples were used for training and the remaining 20% for validation.

4. Synthetic experiment

In this section, the denoising performance of the proposed VMD–DnCNN model was evaluated using synthetic seismic data. As shown in Figure 4, Gaussian noise was added to shot gathers 10, 510, 1,010, and 1,510 to achieve SNRs of 6 dB, 0 dB, −5 dB, and −10 dB, respectively. To better assess the denoising effectiveness of VMD–DnCNN, comparative analyses were conducted with several typical seismic denoising methods, including both conventional and deep learning-based approaches. It was observed that when the noise level corresponded to an SNR of 6 dB, some

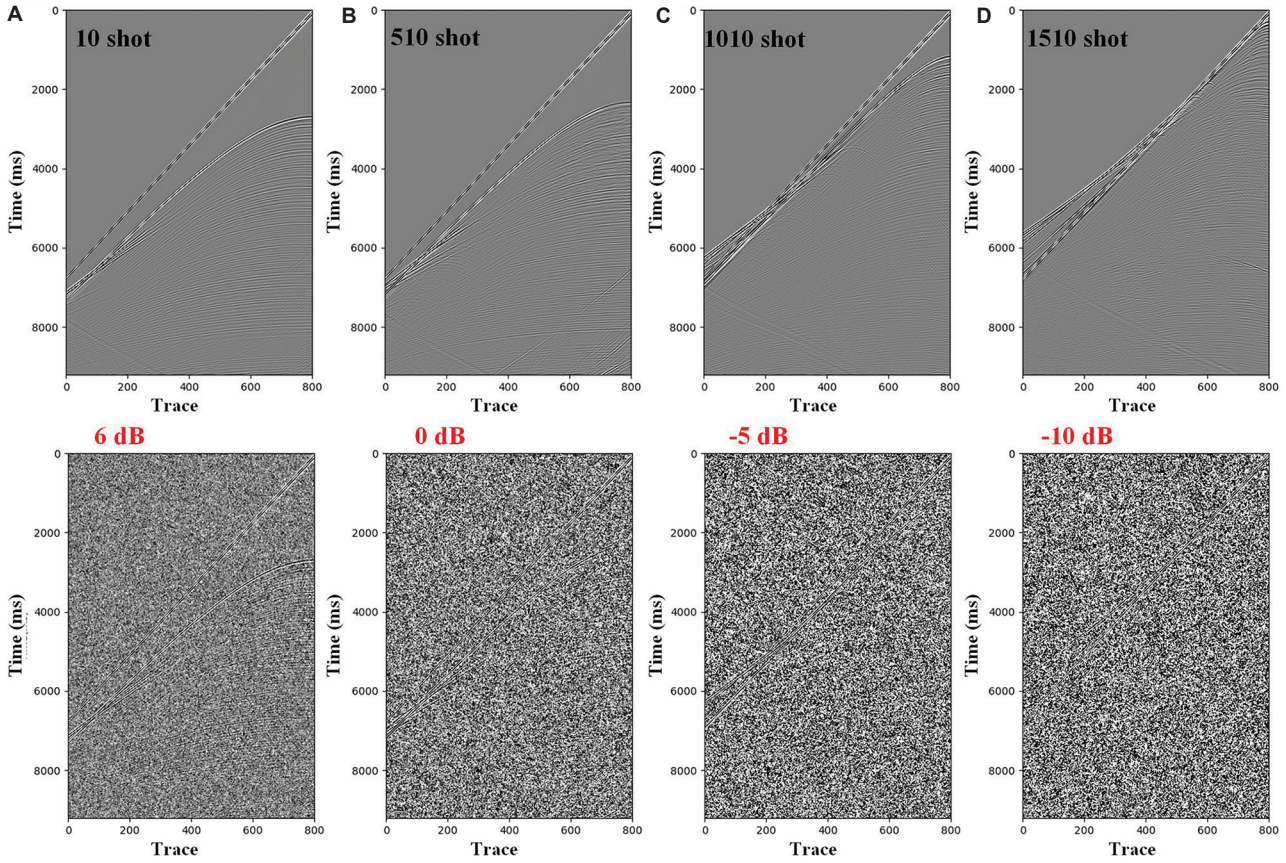

Figure 4. Noise-free data and the corresponding data with added Gaussian noise under varying conditions: (A) 6 dB, (B) 0 dB, (C) −5 dB, and (D) −10 dB.

seismic reflections were still barely visible. However, as the noise increased to 0 dB, most of the seismic signals were overwhelmed by noise, and only a small portion remained observable. At −5 dB, only the strong direct wave energy was distinguishable. When the noise level reached −10 dB, almost no valid seismic information was visually identified.

To evaluate the denoising performance of the proposed VMD–DnCNN model, it was compared with several widely used seismic denoising methods, including traditional techniques, such as the wavelet transform and VMD, as well as deep learning-based approaches, such as the DnCNN and U-Net model.[29] For parameter settings, the number of IMFs in the VMD was set to three, and a six-level Daubechies-4 (db4) wavelet was used for the wavelet transform. Thresholds in both the VMD and wavelet methods were adaptively adjusted based on the complexity of the noise in the seismic data. To ensure experimental fairness, all denoising methods were implemented and tested on an Nvidia GeForce RTX 4060 Ti GPU with 16 GB of video memory. In addition, to quantitatively assess the denoising performance of each method, four commonly used evaluation metrics for seismic signal quality were adopted: SNR, root mean square error (RMSE), peak SNR (PSNR), and structural similarity index measure (SSIM). The specific formulations of these two metrics are defined as follows:

$$SNR = 10\log_{10}\left(\frac{\sum_{i=1}^{N}\sum_{j=1}^{M}\left(X(i,j)-\bar{X}\right)^2}{\sum_{i=1}^{N}\sum_{j=1}^{M}\left(\hat{Y}(i,j)-X(i,j)\right)^2}\right) \quad \text{(IV)}$$

$$RMSE = \sqrt{\frac{1}{NM}\sum_{i=1}^{N}\sum_{j=1}^{M}\left(\hat{Y}(i,j)-X(i,j)\right)^2} \quad \text{(V)}$$

$$SSIM = \frac{\left(2\mu_X\mu_Y + C_1\right)\left(2\sigma_{XY} + C_2\right)}{\left(\mu_X^2 + \mu_Y^2 + C_1\right)\left(\sigma_X^2 + \sigma_Y^2 + C_2\right)} \quad \text{(VI)}$$

$$PSNR = 10\log_{10}\left(\frac{MAX_X^2}{MSE}\right) \quad \text{(VII)}$$

where X represents the original seismic signal; $\hat{Y}$ represents either the noisy seismic data or the denoised seismic data, which are used to calculate the SNR and

RMSE for the original signal or the denoised result, respectively; M and N represent the number of receivers (traces) and the number of sampling points per receiver, respectively; μ_X and μ_Y are the mean amplitudes of X and Y, respectively; σ_X^2 and σ_Y^2 are the variances; σ_{XY} is the covariance between X and Y; the constants C_1 and C_2 are small positive numbers introduced to avoid division by zero; MAX_X^2 is the squared maximum amplitude of the reference signal; and MSE is the mean squared error between X and Y. The SSIM ranges from −1 to 1, with higher values indicating greater structural similarity between the two signals. The PSNR is expressed in decibels (dB), and higher values indicate better reconstruction quality with smaller differences from the reference signal.

A comparative analysis of denoising performance was conducted using the synthetic seismic data with added Gaussian noise (Figure 4). The denoising results of various methods are presented under different SNRs. To better illustrate the robustness of each method under varying noise levels, a performance comparison curve was additionally generated by adding Gaussian noise ranging from −10 dB to 6 dB in 1 dB increments to shot gather 1,510. This allows for the evaluation of how effectively each method performs against different noise intensities.

First, the visual denoising results of each method across different synthetic shot gathers were examined (Figure 5). When the noise level was 0 dB, traditional methods such as the wavelet and VMD models left noticeable background noise, and much of the noise remained entangled with the seismic signals. In contrast, deep learning methods like DnCNN and U-Net effectively suppressed background noise, although some seismic signals were inadvertently removed. Nevertheless, continuous signals across traces were better preserved. At −5 dB and −10 dB noise levels, the VMD method showed even more background noise residue, while the wavelet method exhibited increasingly severe artifacts. Under these conditions, DnCNN and U-Net also struggled to remove background noise effectively, and the retained signals were heavily contaminated by residual noise. In particular, at −10 dB, it became nearly impossible to identify any valid seismic information using these methods. In contrast, the VMD–DnCNN model demonstrated superior denoising performance. At 0 dB, although some background noise remained, it preserved more continuous and weak signals than other methods, maintaining better signal continuity. At −5 dB, it successfully removed most background noise while retaining the underlying seismic signals, achieving a near-complete recovery. Even at −10 dB, the VMD–DnCNN model was still capable of recovering meaningful signals; although some noise remained, the overall clarity of the signal was significantly better than with other methods. From this comparison, it is evident that VMD–DnCNN consistently outperformed other methods under both strong and weak noise conditions. Notably, in scenarios with severe noise contamination where other methods failed to recover seismic signals effectively, VMD–DnCNN retained finer details of the signal. Within the red rectangles in Figure 5, it can be seen that both the strong direct arrivals and the weaker reflections following the direct waves were better restored using VMD–DnCNN compared to other methods. Even under strong noise conditions, the proposed method was able to improve SNR to over 20 dB, whereas the performance of other methods—especially deep learning models—declined under such noisy scenarios. As shown in Table 2, the quantitative results also confirm that VMD–DnCNN achieved the highest improvements in both SNR and RMSE metrics compared to the other benchmark methods.

The importance of computational efficiency in seismic signal processing should not be overstated. Therefore, the computational performance of different denoising methods was analyzed by evaluating their performance under various noise levels. The SNR improvements achieved by each method across different noise intensities are illustrated in Figure 6, and the detailed performance metrics are summarized in Table 3. All methods were evaluated under identical denoising environments with consistent hyperparameter settings, including the number of training epochs, sample length, and learning rate. The training times required for VMD–DnCNN, DnCNN, and U-Net were 0.504 h, 0.498 h, and 2.144 h, respectively, while the traditional methods did not require any pretraining. In terms of average inference time per denoising task, the VMD–DnCNN, DnCNN, U-Net, VMD, and wavelet models required 2.178 s, 2.1012 s, 3.343 s, 66.26 s, and 1.291 s, respectively. Their corresponding average SNR improvements were 29.05 dB, 11.53 dB, 12.83 dB, 9.34 dB, and 8.95 dB. Both VMD–DnCNN and DnCNN consisted of 20 convolutional layers, while U-Net contained 19 convolutional layers along with four downsampling and four upsampling operations. Although U-Net slightly outperformed DnCNN in terms of denoising results, it required nearly four times the training time of DnCNN. While VMD achieved slightly better denoising results than the wavelet method, its time and memory consumption were significantly higher compared to the other methods, making it less practical for large-scale applications. Furthermore, DnCNN and VMD–DnCNN exhibited similar inference speeds and were slightly faster than U-Net. Although their inference times were longer than those of the wavelet method, they remained within

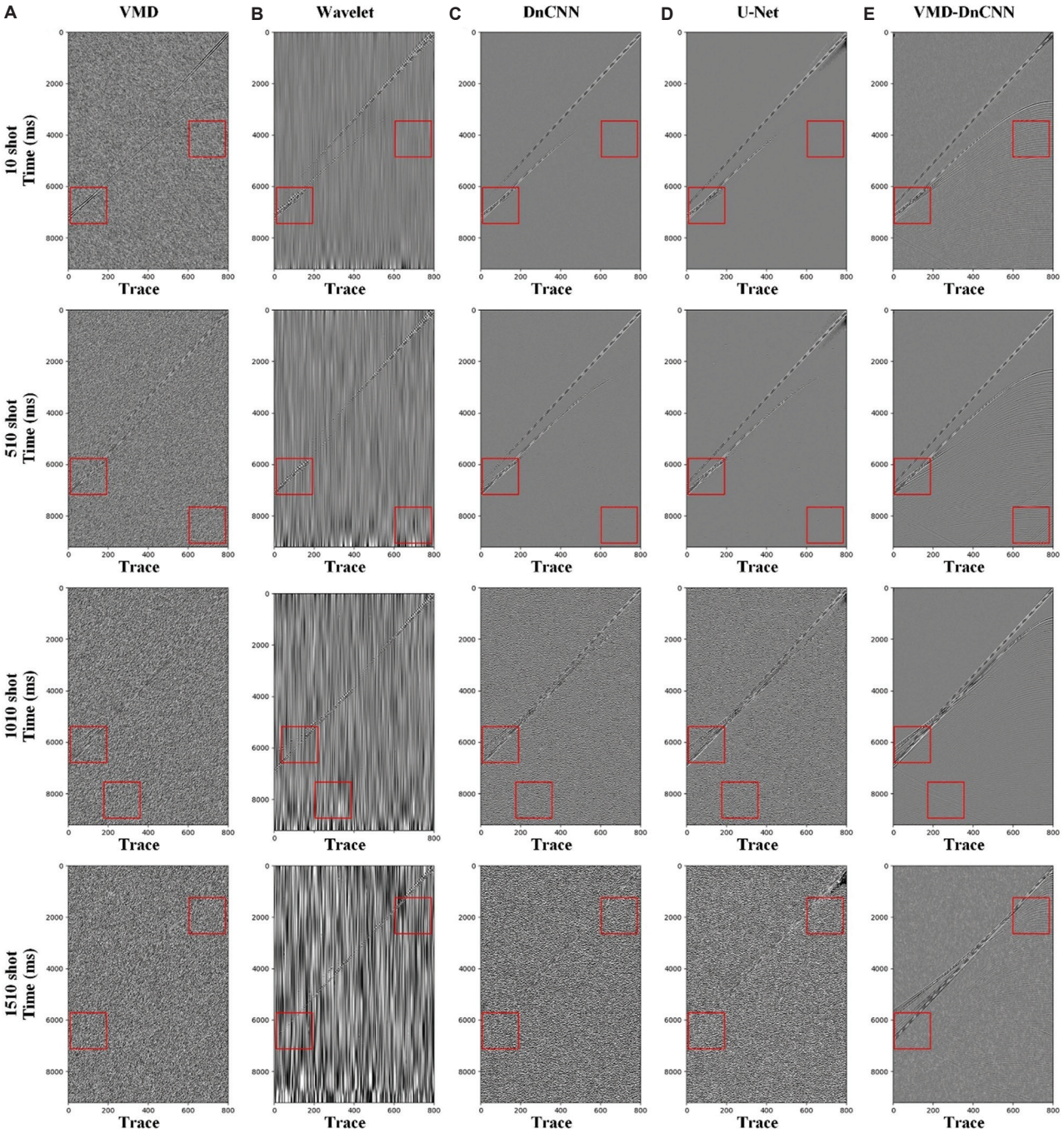

Figure 5. Denoising performance of different methods under different SNR conditions. Panels A–F display, from top to bottom, the denoised results corresponding to varying SNR levels for each respective method: (A) VMD, (B) wavelet, (C) DnCNN, (D) U-Net, and (E) VMD–DnCNN.
Abbreviations: DnCNN: Denoising convolutional neural network; SNR: Signal-to-noise ratio; VMD: Variational mode decomposition.

an acceptable range for practical use. Although deep learning methods required a one-time model pretraining phase, the training time was relatively acceptable. Once trained, the model could be reused without retraining, making the cost of pretraining negligible in the long term.

The robustness of each method across 17 different SNR levels was also analyzed using the performance curves, as shown in Figure 6. While all methods demonstrated a generally linear increase in SNR with decreasing noise, VMD–DnCNN achieved optimal denoising performance within the noise levels that were close to those used during

training. Even outside that range, although it did not always yield the highest SNR, it still consistently outperformed the other methods in denoising effectiveness. This phenomenon occurs because, outside the training interval, the frequencies of the high-, mid-, and low-frequency modes decomposed by 2D-VMD vary in response to differing noise intensities. Consequently, the network applies denoising based on signal feature frequencies learned during training, which may not accurately correspond to the characteristics of the input data.

Table 2. Result of processing at different SNRs by deep learning methods

Noisy record (dB)	Parameter	VMD	Wavelet	DnCNN	U-Net	VMD–DnCNN
6	SNR	12.40	12.87	19.45	19.77	23.07
	RMSE	0.6166	0.5842	0.2736	0.2639	0.1806
	PSNR	54.54	55.22	61.73	62.32	65.41
	SSIM	0.9992	0.9990	0.9998	0.9998	0.9999
0	SNR	7.85	9.14	17.90	18.15	27.03
	RMSE	1.0524	0.9072	0.3307	0.3216	0.1156
	PSNR	51.28	51.40	60.08	48.38	69.29
	SSIM	0.9981	0.9977	0.9997	0.9943	0.9999
−5	SNR	5.67	5.23	4.19	5.81	24.95
	RMSE	1.4332	1.5068	1.6990	1.4099	0.1556
	PSNR	47.87	46.99	45.76	48.38	66.71
	SSIM	0.9944	0.9939	0.9920	0.9943	0.9999
−10	SNR	0.80	2.25	−5.73	−3.47	23.23
	RMSE	2.8440	2.4054	6.0296	4.6496	0.2148
	PSNR	42.05	42.93	35.39	37.23	63.91
	SSIM	0.9817	0.9851	0.9173	0.9238	0.9998

Abbreviations: DnCNN: Denoising convolutional neural network; PSNR: Peak signal-to-noise ratio; RMSE: Root mean square error; SNR: Signal-to-noise ratio; SSIM: Structural similarity index measure; VMD: Variational mode decomposition.

As a frequency-domain analysis can better highlight seismic signal characteristics, this section further analyzes the denoising results using frequency–wavenumber (F–K) spectra, as shown in Figure 7. The denoising results of shot gather 510 were used as an example for detailed analysis. As shown in Figure 7A, the left panel shows the noise-free data, while the right panel demonstrates the data after adding Gaussian noise. Figure 7B–F displays the denoised results from different methods on the left, and the corresponding removed noise components on the right. As shown in Figure 7A, the dominant frequency of the original seismic signal lay in the range from 20–50 Hz. After adding noise, the frequency content shifted significantly into the 70–80 Hz range, completely overwhelming the original signal. By examining the denoising results, both the VMD and wavelet methods were found to remove portions of the strong direct wave signals. Specifically, VMD tended to misclassify parts of the original signal as noise, and its output was centered around 50 Hz. The wavelet method partially restored the original 20–50 Hz range in some regions, but also retained components in the higher-frequency band, indicating inconsistency in noise suppression. Among deep learning-based approaches, both U-Net and DnCNN exhibited better overall denoising performance. However, they tended to suppress certain high- and low-frequency components

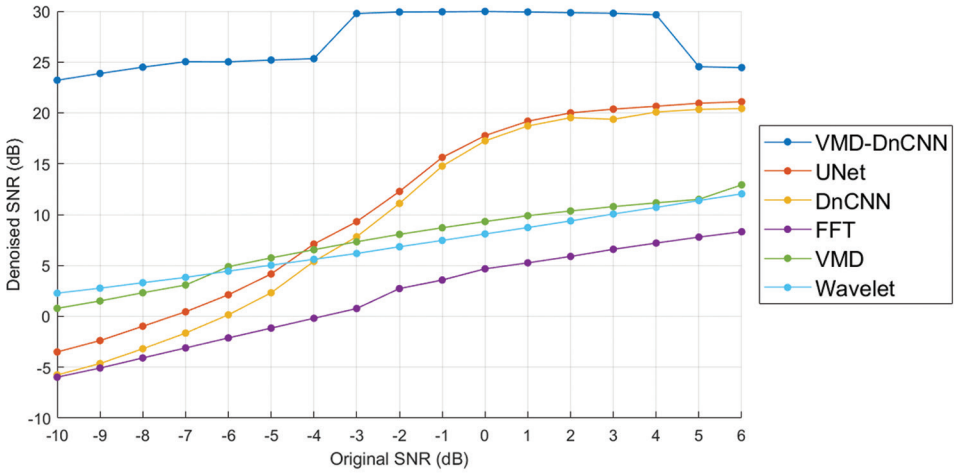

Figure 6. Denoising performance curves of the VMD, wavelet, DnCNN, U-Net, FFT, and VMD–DnCNN methods under different SNR conditions. Abbreviations: DnCNN: Denoising convolutional neural network; FFT: Fast Fourier transform; SNR: Signal-to-noise ratio; VMD: Variational mode decomposition.

Table 3. Computer performance analysis

Hyperparameter	VMD	Wavelet	DnCNN	U-Net	VMD–DnCNN
Average processing time (s)	66.260	1.291	2.012	3.343	2.178
Training time (h)	0	0	0.498	2.144	0.501
Average improved SNR (dB)	9.34	8.95	11.53	12.83	29.05
Memory cost (MB)	125.73	7.63	0.89	22.52	0.89

Abbreviations: DnCNN: Denoising convolutional neural network; SNR: Signal-to-noise ratio; VMD: Variational mode decomposition.

of the original signal, resulting in the recovered signals being mainly concentrated around the 30–40 Hz range. In contrast, the VMD–DnCNN method demonstrated superior performance by preserving both high- and low-frequency information. Within the red rectangular regions in Figure 7, VMD–DnCNN was observed to more effectively restore the seismic signal in areas with wider frequency separation, retaining more detailed seismic features. Overall, the VMD–DnCNN method demonstrated superior capability in restoring the signal's frequency content to its original distribution, thus offering

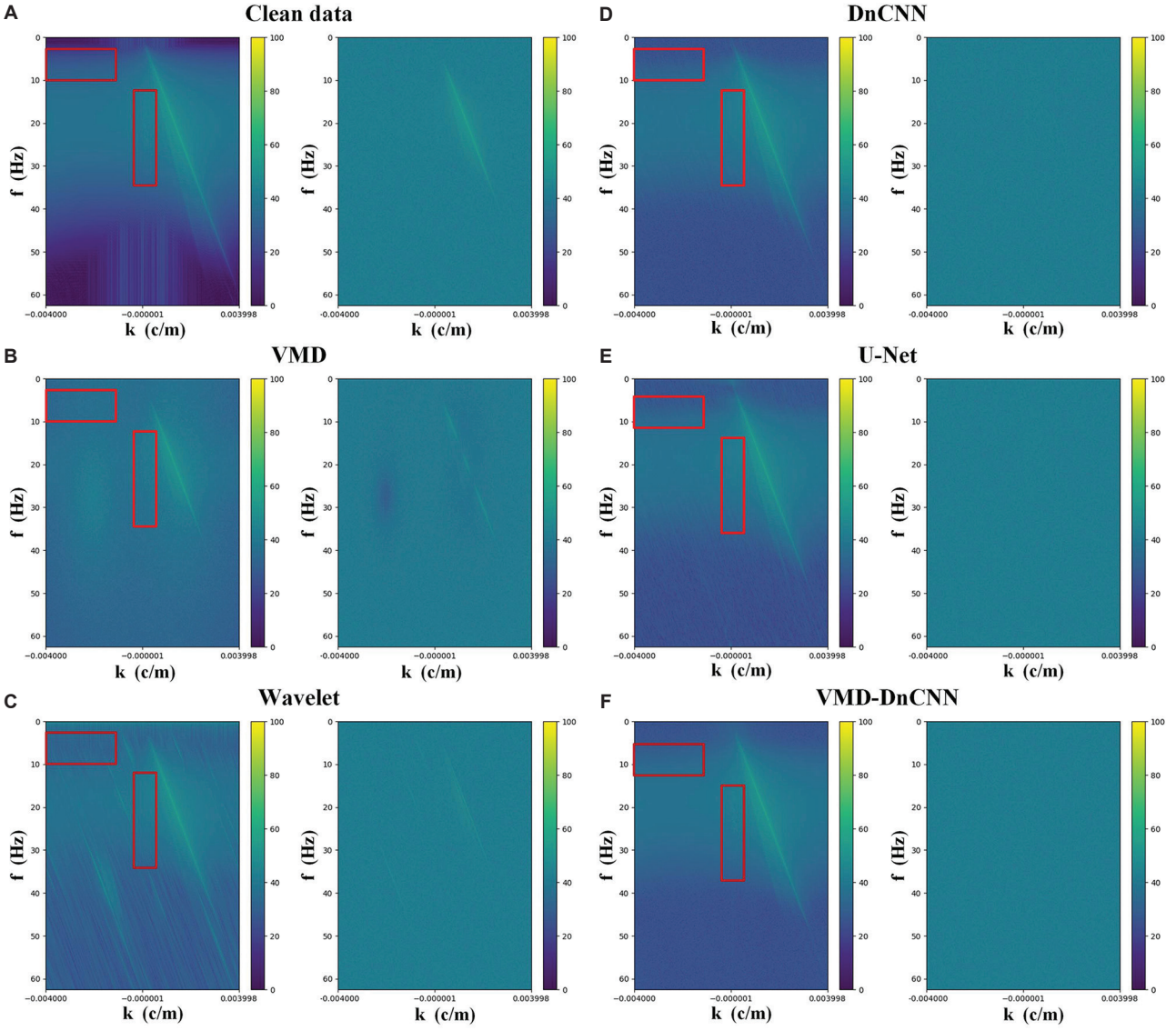

Figure 7. Frequency–wavenumber (F–K) spectrum analysis of noisy shot gathers 510 under different denoising methods: (A) clean F–K spectra, (B) VMD, (C) wavelet, (D) DnCNN, (E) U-Net, and (F) VMD–DnCNN.
Abbreviations: DnCNN: Denoising convolutional neural network; VMD: Variational mode decomposition.

a more accurate and comprehensive reconstruction in the frequency domain.

Subsequently, how the VMD–DnCNN network learns seismic signal features was analyzed by examining feature activation heatmaps at different network layers. The denoising results of shot 1,510 were used as the case study. As illustrated in Figure 8, the heatmaps correspond to the 1st, 4th, 10th, and 16th layers of the network, displayed from left to right. It can be observed that the network predominantly focused on low-frequency components of the seismic signals, with these features being highlighted from the initial layer, albeit in a relatively simplistic form. By the fourth layer, the network began to learn features at even lower frequencies while simultaneously capturing high-frequency components associated with direct arrivals. At the 10th layer, the features remained primarily low-frequency; however, by the 16th layer, the learned features shifted toward higher frequencies, incorporating both low- and high-frequency information. Given that seismic signals primarily consisted of low-frequency components, decomposing the signals into low-, mid-, and high-frequency bands through 2D VMD facilitated more effective feature learning by the network, surpassing the limitations of single time-domain feature extraction.

5. Field data experiment

In this section, the denoising performance of the proposed VMD–DnCNN model was evaluated using real seismic data, specifically marine seismic records. The real seismic data used in this experiment are shown in Figure 9A. By processing the field data, the effectiveness of VMD–DnCNN was demonstrated in real-world scenarios. For comparative analysis, the same baseline methods used in the synthetic data experiments were adopted. The real marine dataset used for evaluation was the 2D Mobil AVO Viking Graben Line 12 dataset. This dataset consists of 1,011 shot gathers, each containing approximately 119 seismic traces with 1,500 sampling points per trace. The sampling interval is 4,000 μs (i.e., 250 Hz sampling rate), resulting in a trace duration of 6 s. Shot gather 1 was selected for denoising analysis in this study. The denoising results of different methods applied to the real marine seismic data are shown in Figure 9.

Among the traditional methods, VMD effectively removed a significant amount of background noise and successfully separated weak signals from noise; however, some residual artifacts remained, and small portions of continuous strong signals were mistakenly removed as noise. Overall, the performance was relatively good. The wavelet method, on the other hand, tended to remove weak signals during denoising, produce residual artifacts around continuous strong signals, and leave some noise behind. For deep learning methods, both DnCNN and U-Net successfully suppressed background noise. However, the denoising effect of U-Net was inferior to that of DnCNN, as U-Net did not preserve weak signals well and exhibited residual artifacts in regions of continuous strong signals. In contrast, DnCNN showed relatively better overall denoising performance. Although some continuous strong signals were erroneously treated as noise, the continuity of the signals was largely preserved. In terms of weak signal processing, while residual noise still existed, a portion of the weak signals was retained, resulting in comparatively good denoising performance. In the case of VMD–DnCNN, although residual artifacts and incomplete removal of background noise remained, the method achieved a clear separation between weak signals

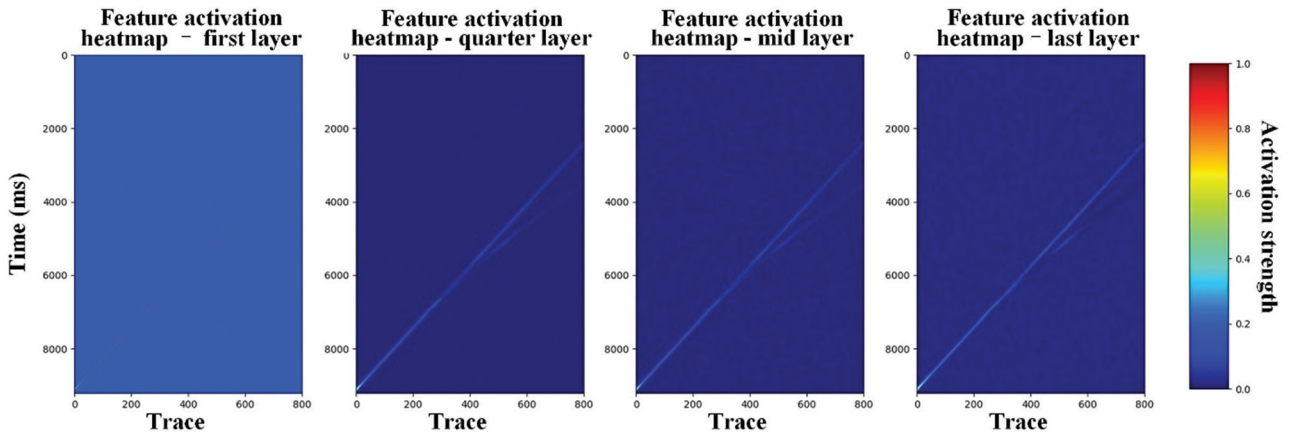

Figure 8. The VMD–DnCNN feature activation heatmap.
Abbreviation: Variational mode decomposition–denoising convolutional neural network.

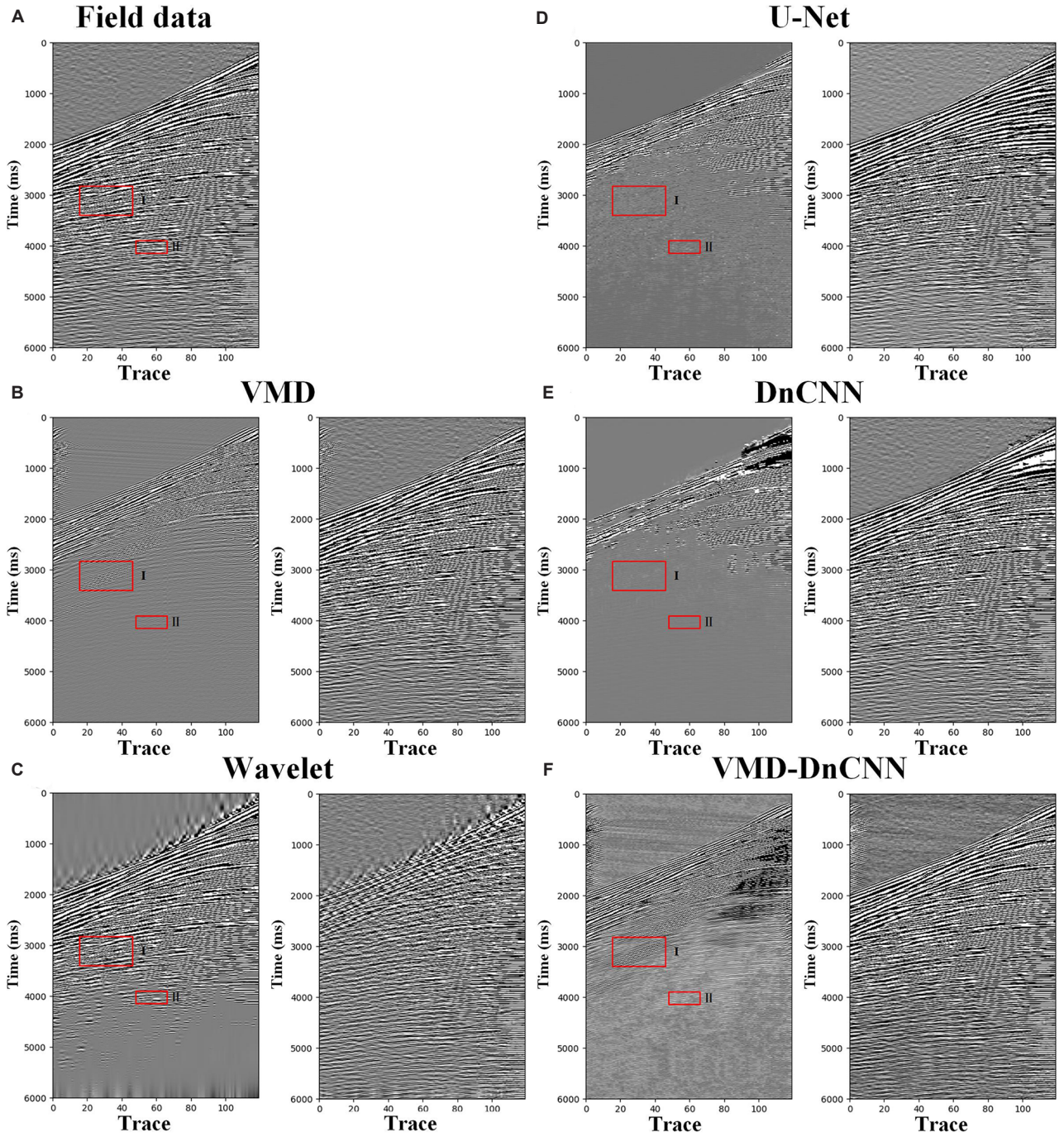

Figure 9. Denoising results on real marine seismic data by different methods: (A) noisy data, (B) VMD, (C) wavelet, (D) DnCNN, (E) U-Net, and (F) VMD–DnCNN.
Abbreviations: DnCNN: Denoising convolutional neural network; VMD: Variational mode decomposition.

and noise while preserving more weak signals overall. By examining the red-highlighted regions of the denoised results in Figure 10, as shown in the enlarged views of areas I and II, the VMD and wavelet methods left most of the noise residuals; U-Net recovered only a small fraction of the signals; DnCNN recovered some components, but with residual noise; and VMD recovered signals well. However, when these results were compared to VMD–DnCNN, the recovered signals by VMD–DnCNN were noticeably clearer.

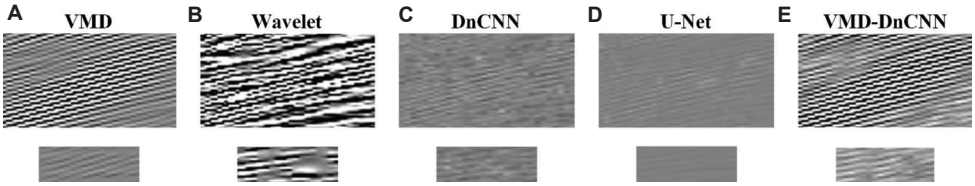

Figure 10. Crimson rectangular areas in Figure 9. From top to bottom are the zoomed-in views of regions I and II from different methods: (A) VMD, (B) wavelet, (C) DnCNN, (D) U-Net, and (E) VMD–DnCNN.
Abbreviations: DnCNN: Denoising convolutional neural network; VMD: Variational mode decomposition.

6. Conclusion

Traditional decomposition methods for seismic signal processing often suffer from the problem of mode mixing, making them difficult to completely prevent noise components from being incorporated into each mode, thereby reducing denoising accuracy. To address this issue, this study proposed a novel seismic signal denoising method that combines VMD with DnCNN—referred to as VMD–DnCNN. Seismic signals are primarily low-frequency, while noise is concentrated in high-frequency bands. Therefore, decomposition through VMD enables the network model to learn the characteristics of both seismic signals and noise more effectively. This method first applies VMD to decompose the noisy signal into three frequency-specific modes, corresponding to high-frequency noise, mid-frequency seismic phases, and low-frequency structural components. These modes, together with the original noisy signal, are used to construct a four-channel input, providing the deep learning network with clearer and more distinguishable frequency information. With this decomposition, the network not only learns to differentiate between effective signal and noise features across frequency bands but also leverages the complementary characteristics of different modes to better detect and preserve weak signals, especially under high-noise conditions. By adapting the DnCNN architecture and expanding the input channels, the VMD–DnCNN model is capable of extracting deep semantic features from seismic data while integrating both time-domain and frequency-domain information. This significantly enhances the model's denoising performance and generalization ability. Experimental results demonstrate that the proposed method outperforms both traditional and standalone deep learning approaches under various noise levels, and it remains effective in preserving fine signal structures even under low SNR conditions.

Despite its clear advantages in denoising accuracy and robustness, the VMD–DnCNN method has certain limitations in practical applications. First, it relies on a pre-decomposition step, where VMD must be applied to the input signal before feeding data into the network. This preprocessing not only increases the overall computational cost and complexity of the workflow but also makes performance highly sensitive to the VMD parameter settings. Inaccurate parameter choices may lead to suboptimal mode separation, which can adversely affect network learning. Second, as a variational optimization technique, VMD is computationally intensive—especially when dealing with large-scale 2D seismic data—and may significantly increase resource consumption. Moreover, mode mixing remains present to some extent, with noise potentially remaining in effective modes, interfering with the network's learning process. Therefore, future research can explore learnable decomposition mechanisms or end-to-end jointly optimized frameworks that integrate decomposition and network training in a unified architecture, further enhancing the automation and adaptability of seismic denoising.

Acknowledgments

All seismic datasets used in this study are sourced from the open-access resources released by the Society of Exploration Geophysicists (SEG). The authors would like to express their sincere gratitude to BP Exploration Operation Company for providing the high-quality seismic dataset, 2007 BP Anisotropic Velocity Benchmark dataset, to the geophysical research community.

Funding

This work was supported in part by the Deep Earth Probe and Mineral Resources Exploration-National Science and Technology Major Project (grant no.: 2024ZD1002202), in part by the Guizhou Provincial Basic Research Program (Natural Science) (grant no.: QianKeHeJiChu-K[2024] YiBan013), in part by the Guizhou University Basic Research Project (grant no.: GuiDaJiChu[2023]44), and in part by the Guizhou University Talent Introduction Research Project (grant no.: GuiDaRenJiHeZi[2023]10).

Conflict of interest

The authors have approved the submission and declare no conflicts of interest.

Author contributions

Conceptualization: Liang Zhang, Shengrong Zhang
Formal analysis: Xuesha Qin
Investigation: Liang Zhang, Shengrong Zhang
Methodology: Liang Zhang, Shengrong Zhang
Visualization: Xuesha Qin
Writing–original draft: Shengrong Zhang
Writing–review & editing: Liang Zhang, Xuesha Qin

Availability of data

All seismic datasets used in this study are sourced from the open-access resources released by the Society of Exploration Geophysicists (SEG; https://wiki.seg.org/wiki/2007_BP_Anisotropic_Velocity_Benchmark and https://wiki.seg.org/wiki/Mobil_AVO_viking_graben_line_12). The innovative code presented in this paper has been made open source. Interested researchers may download it directly from: https://github.com/zsr981103/VMD-DnCNN.git

References

1. Zhong T, Li F, Zhang R, Dong X, Lu S. Multiscale residual pyramid network for seismic background noise attenuation. *IEEE Trans Geosci Remote Sens*. 2022;60:1-14.

   doi: 10.1109/tgrs.2022.3217887

2. Dong X, Lin J, Lu S, Wang H, Li Y. Multiscale spatial attention network for seismic data denoising. *IEEE Trans Geosci Remote Sens*. 2022;60:1-17.

   doi: 10.1109/tgrs.2022.3178212

3. Cooper HW, Cook RE. Seismic data gathering. *Proc IEEE*. 1984;72:1266-1275.

   doi: 10.1109/PROC.1984.13016

4. Spikes KT, Tisato N, Hess TE, Holt JW. Comparison of geophone and surface-deployed distributed acoustic sensing seismic data. *Geophysics*. 2019;84:A25-A29.

   doi: 10.1190/geo2018-0528.1

5. Wang X, Ma J, Dong X, Cheng M. HCVT-Net: A hybrid CNN-transformer network for self-supervised 3D seismic data interpolation. *J Appl Geophys*. 2025;242:105873.

   doi: 10.1016/j.jappgeo.2025.105873

6. Dong X, Cheng M, Wang H, Li G, Lin J, Lu S. A potential solution to insufficient target-domain noise data: Transfer learning and noise modeling. *IEEE Trans Geosci Remote Sens*. 2023;61:1-15.

   doi: 10.1109/tgrs.2023.3300697

7. Anvari R, Siahsar MAN, Gholtashi S, Kahoo AR, Mohammadi M. Seismic random noise attenuation using synchrosqueezed wavelet transform and low-rank signal matrix approximation. *IEEE Trans Geosci Remote Sens*. 2017;55:6574-6581.

   doi: 10.1109/tgrs.2017.2730228

8. Mousavi SM, Langston CA. Automatic noise-removal/signal-removal based on general cross-validation thresholding in synchrosqueezed domain and its application on earthquake data. *Geophysics*. 2017;82:V211-V227.

   doi: 10.1190/geo2016-0433.1

9. Liu N, Gao J, Zhang B, Wang Q, Jiang X. Self-adaptive generalized S-transform and its application in seismic time-frequency analysis. *IEEE Trans Geosci Remote Sens*. 2019;57:7849-7859.

   doi: 10.1109/tgrs.2019.2916792

10. Neelamani R, Baumstein AI, Gillard DG, Hadidi MT, Soroka WL. Coherent and random noise attenuation using the curvelet transform. *Leading Edge*. 2008;27:240-248.

    doi: 10.1190/1.2840373

11. Starck JL, Candès EJ, Donoho DL. The curvelet transform for image denoising. *IEEE Trans Image Process*. 2002;11:670-684.

    doi: 10.1109/tip.2002.1014998

12. Do MN, Vetterli M. The contourlet transform: An efficient directional multiresolution image representation. *IEEE Trans Image Process*. 2005;14:2091-2106.

    doi: 10.1109/tip.2005.859376

13. Yu S, Ma J. Complex variational mode decomposition for slope-preserving denoising. *IEEE Trans Geosci Remote Sens*. 2017;56:586-597.

    doi: 10.1109/tgrs.2017.2751642

14. Bekara M, Van der Baan M. Random and coherent noise attenuation by empirical mode decomposition. *Geophysics*. 2009;74:V89-V98.

    doi: 10.1190/1.3157244

15. Liu N, Li F, Wang D, Gao J, Xu Z. Ground-roll separation and attenuation using curvelet-based multichannel variational mode decomposition. *IEEE Trans Geosci Remote Sens*. 2021;60:1-14.

    doi: 10.1109/tgrs.2021.3054749

16. Bekara M, Van der Baan M. Local singular value decomposition for signal enhancement of seismic data. *Geophysics*. 2007;72:V59-V65.

    doi: 10.1190/1.2435967

17. Dong X, Zhong T, Li Y. New suppression technology for low-frequency noise in desert region: The improved robust principal component analysis based on prediction of neural network. *IEEE Trans Geosci Remote Sens*. 2020;58:4680-4690.

    doi: 10.1109/tgrs.2020.2966054

18. Trickett S. F-xy cadzow noise suppression. In: *SEG Technical Program Expanded Abstracts*. United States: Society of

Exploration Geophysicists; 2008. p. 2586-2590.

doi: 10.1190/1.3063880

19. Goodfellow I, Bengio Y, Courville A. *Deep Learning*. Vol 1. Cambridge: MIT Press; 2016.

20. LeCun Y, Bengio Y, Hinton G. Deep learning. *Nature*. 2015;521:436-444.

doi: 10.1038/nature14539

21. Yu S, Ma J, Wang W. Deep learning for denoising. *Geophysics*. 2019;84:V333-V350.

doi: 10.1190/geo2018-0668.1

22. Wang X, Ma J, Dong X, Zhong T, Dong S. EFGW-UNet: A deep-learning-based approach for weak signal recovery in seismic data. *IEEE Trans Geosci Remote Sens*. 2024;62:1-3.

doi: 10.1109/tgrs.2024.3398590

23. Zhu W, Mousavi SM, Beroza GC. Seismic signal denoising and decomposition using deep neural networks. *IEEE Trans Geosci Remote Sens*. 2019;57:9476-9488.

doi: 10.1109/TGRS.2019.2926772

24. Zhang L, Li G, Chen H, *et al*. Identification and suppression of multicomponent noise in audio magnetotelluric data based on convolutional block attention module. *IEEE Trans Geosci Remote Sens*. 2024;62:5905515.

doi: 10.1109/tgrs.2024.3361942

25. Wei X, Zhang C, Jiang B, *et al*. *Efficient Seismic Data Interpolation Via Sparse Attention Transformer and Diffusion Model*. [arXiv Preprint]; 2025.

doi: 10.48550/arxiv.2506.07923

26. Zhang K, Zuo W, Chen Y, Meng D, Zhang L. Beyond a Gaussian denoiser: Residual learning of deep CNN for image denoising. *IEEE Trans Image Process*. 2017;26:3142-3155.

doi: 10.1109/TIP.2017.2662206

27. Yu S, Ma J, Osher S. Monte Carlo data-driven tight frame for seismic data recovery. *Geophysics*. 2016;81:V327-V340.

doi: 10.1190/geo2015-0343.1

28. Kingma DP, Ba J. *Adam: A Method for Stochastic Optimization*. [arXiv preprint]; 2014.

doi: 10.48550/arXiv.1412.6980

29. Ronneberger O, Fischer P, Brox T. U-Net: Convolutional Networks for Biomedical Image Segmentation. In: *Medical Image Computing and Computer-Assisted Intervention - MICCAI 2015: 18th International Conference, Munich, Germany, Proceedings, Part III*. Vol 18. Springer; 2015. p. 234-241.

doi: 10.1007/978-3-319-24574-4_28

ACCSCIENCE PUBLISHING

Journal of Seismic Exploration

ARTICLE

Microseismic event locations using grid-searching method and Newton–Raphson-based optimizer

Shaohui Zhou[1], Tianqi Jiang[2]*, Junhao Qu[1], Peng Lin[2], Yu Wang[1], and Yajun Li[1]

[1]Shandong Earthquake Agency, Jinan, Shandong, China

[2]State Key Laboratory for Fine Exploration and Intelligent Development of Coal Research, China University of Mining and Technology-Beijing, Beijing, China

(This article belongs to the *Special Issue: Advanced Artificial Intelligence Theories and Methods for Seismic Exploration*)

Abstract

Microseismic event location plays a pivotal role in industrial applications, such as coal mining and hydraulic fracturing, by revealing subsurface fracture dynamics through the spatiotemporal analysis of seismic events. As a cornerstone of microseismic monitoring, accurate event localization enables critical insights into underground structural integrity. Traditional arrival-time-based methods employ optimization algorithms to minimize residuals between observed and theoretical arrival times. While this classical approach has proven effective, its accuracy is often compromised by two key limitations: suboptimal initial iteration values and inaccuracies in velocity parameter estimation. To address these challenges, we propose an innovative localization method integrating a grid-searching strategy with a Newton–Raphson-based optimizer. Our approach begins by generating initial iterative vectors—comprising event coordinates and velocity parameters—through a systematic grid-searching technique. Subsequently, the Newton–Raphson optimizer refines these estimates within a four-dimensional search space to achieve high-precision inversion results. The efficacy of the proposed method was rigorously evaluated using both synthetic and field datasets, with comparative analyses conducted against four established localization techniques. Experimental results demonstrate that our method significantly enhances localization accuracy and robustness, reliably inverting both event locations and velocity parameters. These findings provide a valuable technical reference for advancing microseismic monitoring systems, offering improved precision in industrial applications.

Keywords: Microseismic event location; Grid-searching method; Newton–Raphson-based optimizer

***Corresponding author:**
Tianqi Jiang
(jiang_tianqi0623@163.com)

Citation: Zhou S, Jiang T, Qu J, Lin P, Wang Y, Li Y. Microseismic event locations using grid-searching method and Newton–Raphson-based optimizer. *J Seismic Explor*. 2025;34(2):60-71.
doi: 10.36922/JSE025320052

Received: August 04, 2025

Revised: August 22, 2025

Accepted: September 02, 2025

Published online: September 11, 2025

1. Introduction

Microseismic monitoring has gained significant attention across multiple disciplines including mining engineering,[1] carbon capture and utilization,[2] volcanic activity

monitoring,[3] and hydrocarbon reservoir characterization.[4] The accuracy and reliability of microseismic event localization are paramount in these applications, as the methodology must maintain robustness and stability when processing potentially noise-contaminated datasets.

Current localization approaches typically utilize the residuals between theoretical and observed P-wave arrival times as the primary criterion for evaluating inversion quality. The standard workflow involves: (i) identifying actual P-wave arrivals from recorded waveforms, (ii) implementing optimization algorithms to iteratively determine the spatial coordinates that minimize the discrepancy between calculated and observed travel times.

Time-based localization methods, which rely on arrival time picking, ray tracing, primarily originate from the classical Geiger algorithm.[5] These methods determine the source location by identifying the spatial coordinates that minimize the residuals between observed first-arrival times and theoretical travel times.[6,7] However, the accuracy of such localization results is fundamentally constrained by inherent limitations in velocity model accuracy,[8-11] often leading to suboptimal positioning performance. To address these challenges, recent research efforts have focused on two key aspects: (1) developing enhanced optimization algorithms[12,13] and (2) optimizing sensor array configurations.[14-17]

The integration of multiple optimization methods has proven to be an effective strategy for enhancing the accuracy of microseismic event localization. Several hybrid approaches have demonstrated promising results: Jiang and Pei.[18] developed a combined grid search and Newton–Raphson iteration method; Lü *et al.*[19] implemented a hybrid algorithm incorporating simulated annealing with the simplex method; and Luo *et al.*[20] proposed a novel approach utilizing seagull optimization combined with quantile difference analysis. These hybrid methods have shown significant improvements in localization accuracy compared to conventional single-algorithm approaches.

However, the velocity model remains a critical factor affecting localization precision. Dong *et al.*[21] addressed this challenge by developing a velocity-independent localization method that eliminates the need for pre-measured velocity parameters. While this approach effectively mitigates velocity related errors, it inherently lacks the capability to simultaneously invert for velocity parameters during the localization process.

We present a novel microseismic event localization method that combines the grid searching rule with a Newton-Raphson-based optimizer (GNRBO). Unlike conventional Newton-Raphson implementations that employ random initial assignments, our approach systematically generates initial iterative vectors (comprising both event coordinates and velocity parameters) through comprehensive grid sampling. The Newton-Raphson optimizer then refines these estimates within a four-dimensional parameter space, simultaneously solving for both the microseismic source location and the average velocity model.

To evaluate the method's performance, we conducted extensive testing using both synthetic and field datasets, assessing the algorithm's accuracy and stability under various conditions. For comparative analysis, we implemented three established optimization techniques: the Hooke-Jeeves (H-J) direct search method, Genetic Algorithm (GA), and Particle Swarm Optimization (PSO). Results demonstrate that our proposed GNRBO method outperforms these benchmark approaches in both localization accuracy and computational stability.

2. Methods

2.1. Target function

Time-based microseismic localization methods utilize the minimization of residuals between theoretical and observed arrival times as their fundamental principle. Through optimization algorithms, these methods systematically search the potential source space to identify spatial coordinates where the travel-time residuals satisfy predetermined convergence criteria. The source location is considered accurately determined when the minimized residuals achieve the required inversion precision threshold.

The theoretical arrival time of microseismic waves at geophones can be expressed as a function of three key parameters as follows: (1) the spatial coordinates of the seismic source, (2) the receiver positions, and (3) the velocity model of underground wave propagation. This fundamental relationship forms the basis for time-based localization methods and can be mathematically described as follows:

$$T_P^i\left(x_0, y_0, z_0, v_0, T_0\right) = T_0 + t_P^i\left(x_0, y_0, z_0, v_0\right) \quad \text{(I)}$$

Where T_P^i denotes the observed P-wave arrival time at the i-th receiver (**Equation I**), and T_0 represents the origin time of the event.

t_P^i (**Equation II**) corresponds to the theoretical P-travel time from the location (x_0, y_0, z_0) to the i-th receiver at (X_i, Y_i, Z_i) and the velocity parameter is v_0:

$$t_P^i = \sqrt{\frac{\left(X_i - x_0\right)^2 + \left(Y_i - y_0\right)^2 + \left(Z_i - z_0\right)^2}{v_0}} \quad \text{(II)}$$

After eliminating the origin time T_0, the inversion problem reduces to four unknown parameters in the objective function $R(x,y,z,v)$, namely the source coordinates $R(x,y,z)$ and the effective P-wave velocity (v_0). This function quantifies the travel-time residuals between observed and theoretical arrivals as follows:

$$R\left(x,y,z,v\right) = \sqrt{\frac{1}{N}\sum_{i=1}^{N}\left(T_p^i\left(x,y,z,v\right) - T_p^i\left(x_0,y_0,z_0,v_0\right)\right)^2} \quad \text{(III)}$$

$T_p^i\left(x,y,z,v\right)$ is the theoretical P-arrival time:

$$T_p^i\left(x,y,z,v\right) = \hat{T}_0 + t_P^i\left(x,y,z,v\right) \quad \text{(IV)}$$

$\hat{T}_0$ is the estimate of the origin time of the event:

$$\hat{T}_0 = \frac{1}{N}\sum_{i=1}^{N}\left(T_p^i\left(x_0,y_0,z_0,v_0\right) - t_P^i\left(x,y,z,v\right)\right) \quad \text{(V)}$$

According to **Equation III**, when the inversion unknowns approach the true value, the target function value is smaller. Inversions based on the location and velocity of the microseismic event are process in which the optimization algorithm is used to solve the unknowns of the target function, so that the target function tends to 0 and achieves the global optimum.

As shown in **Equation III**, the objective function exhibits an inverse relationship with parameter accuracy, achieving its minimum value when the inverted parameters converge to their true values. The inversion process for microseismic event location and velocity determination constitutes an optimization problem where the algorithm iteratively adjusts the unknown parameters (x,y,z,v) to the minimization of the objective function toward zero.

2.2. Grid-searching method

The grid-search method systematically discretizes the parameter space to generate initial candidate solutions and establishes a set of potential solutions through a rough spatial sampling for the subsequent Newton-Raphson optimization. The searching rule is defined as:

$$\begin{cases} x_i = x_{min} + i\Delta x, & \left(i = 0,1,...,nx\right) \\ y_j = y_{min} + j\Delta y, & \left(j = 0,1,...,ny\right) \\ z_k = z_{min} + k\Delta z, & \left(k = 0,1,...,nz\right) \\ v_l = v_{min} + l\Delta v, & \left(l = 0,1,...,nv\right) \end{cases} \quad \text{(VI)}$$

Where (x_{min}, y_{min}, z_{min}, v_{min}) is the lower bounds in the searching space and (Δx, Δy, Δz, Δv) specifying the discrete interval between adjacent grid points along each axis. nx, ny, nz and nv are sampling numbers in each axis.

We define the swarms in the searching space as:

$$X_{n(i,j,k,l)} = \left(x_i, y_j, z_k, v_l\right) \quad \text{(VII)}$$

According to **Equation VII**, there are $N = nx \times ny \times nz \times nv$ vectors (swarms in the searching space). The initial iteration vectors then are used for Newton-Raphson searching rule in the next section.

2.3. Newton-Raphson searching rule

The Newton-Raphson searching rule is:

$$NRSR = randn \times \frac{\left(X_w - X_b\right) \times \Delta x}{2 \times \left(X_w + X_b - 2 \times X_n\right)} \quad \text{(VIII)}$$

randn is a normally distributed random number with zero mean, and unit variance; X_w is the worst performing solution vector (maximum objective function value); X_b is the best performing solution vector (minimum objective function value); X_n is the n-th generation of the searching swarm population.

The iteration rule is:

$$X_n^{IT+1} = X_n^{IT} - NRSR \quad \text{(IX)}$$

X_n^{IT} represents the n-th generation of the swarm population.

According to Sowmya *et al.*,[22] the iteration rule can be optimized further as:

$$\begin{cases} NRSR = randn \times \dfrac{\left(y_w - y_b\right) \times \Delta x}{2 \times \left(y_w + y_b - 2 \times X_n\right)} \\ y_w = r_1 \times \left(Mean\left(Z_{N+1} + x_n\right) + r_1 \times \Delta x\right) \\ y_b = r_1 \times \left(Mean\left(Z_{N+1} + x_n\right) - r_1 \times \Delta x\right) \\ Z_{n+1} = x_n - randn \times \dfrac{\left(X_w - X_b\right) \times \Delta x}{2 \times \left(X_w + X_b - 2 \times X_n\right)} \\ \Delta x = rand\left(1, dim\right) \times \left|X_n - X_n^{IT}\right| \end{cases} \quad \text{(X)}$$

Where r_1 denotes a uniformly distributed random variable on the interval (0,1), and *rand*(*1*, *dim*) represents a *dim*-dimensional random vector with components independently drawn from U(0,1). The updated iterative scheme is then given by:

$$\begin{cases} X_n^{IT+1} = r_2 \times \left(r_2 \times X1_n^{IT} + \left(1 - r_2\right) \times X2_n^{IT} + \right) + \left(1 - r_2 \times X3_n^{IT}\right) \\ X1_n^{IT} = X_n^{IT} - NRSR + \rho \\ X2_n^{IT} = X_b - NRSR + \rho \\ X3_n^{IT} = X_n^{IT} - \delta \times \left(X2_n^{IT} - X1_n^{IT} \right) \\ \rho = a \times \left(X_b - X_n^{IT} \right) + b \times \left(X_{t1}^{IT} - X_{t2}^{IT} \right) \\ \delta = \left(1 - \left(\dfrac{2 \times IT}{MAX\_IT} \right) \right)^5 \end{cases} \quad \text{(XI)}$$

Where a and b are random values in (0,1), $t1$ and $t2$ are random integers in the range of the number of iteration vector N. MAX_IT is the maximum generation number of the searching swarm population.

To enhance the robustness of the optimization process and prevent premature convergence to local optima, a Trap Avoidance Operator (TAO) is considered to dynamically evaluate and adjust the iteration vectors. This mechanism operates as follows:

$$\begin{cases} X_{TAO}^{IT} = X_n^{IT+1} + \theta_1 \times \left(\mu_1 \times X_b - \mu_2 \times X_n^{IT} \right) + \theta_2 \times \delta \times \\ \left(\mu_1 \times mean\left(X^{IT} - \mu_2 \times X_n^{IT} \right) \right), \mu_1 < 0.5 \\ X_{TAO}^{IT} = X_b + \theta_1 \times \left(\mu_1 \times X_b - \mu_2 \times X_n^{IT} \right) + \theta_2 \times \delta \times \\ \left(\mu_1 \times mean\left(X^{IT} - \mu_2 \times X_n^{IT} \right) \right), \mu_1 \geq 0.5 \end{cases} \quad \text{(XII)}$$

Where θ_1 is a random value in (−1,1), θ_2 is a random value in (−0.5,0.5), while μ_1 and μ_2 are represented by:

$$\begin{cases} \mu_1 = \beta \times 3 \times rand + \left(1 - \beta\right) \\ \mu_2 = \beta \times rand + \left(1 - \beta\right) \end{cases} \quad \text{(XIII)}$$

During the iteration, if the random number is less than the decision factor (DF, which is 0.6 in this paper), the particles are updated so that:

$$X_n^{IT+1} = X_{TAO}^{IT} \quad \text{(XIV)}$$

According to Sowmya *et al.*,[22] β denotes a binary number, either 1 or 0. If the value of a random value between 0 and 1 is ≥0.5, then the value of β is 0; otherwise, the value is 1. We assume that the optimization algorithm obtains the best performing solution when the iteration process is finished. Figure 1 illustrates the workflow of the proposed approach to visualize the key steps.

3. Synthetic data tests

The numerical simulation establishes a three-dimensional monitoring volume spanning *1000m* (*x-axis*) × *1000m* (*y-axis*) × *500m* (*z-axis*). The sensor network consists of eight seismic receivers (blue rectangular markers) deployed underground, while 10 synthetic microseismic sources (red spherical markers) are distributed throughout the volume to test localization performance (Figure 2).

The coordinates of the sensors and events, along with the average velocity of the monitoring area and the origin times of events, are presented in Tables 1 and 2.

To evaluate the performance of the proposed method in terms of positioning accuracy and convergence stability, we conducted tests using simulated P-wave travel times. For comparison, three established algorithms—the H-J

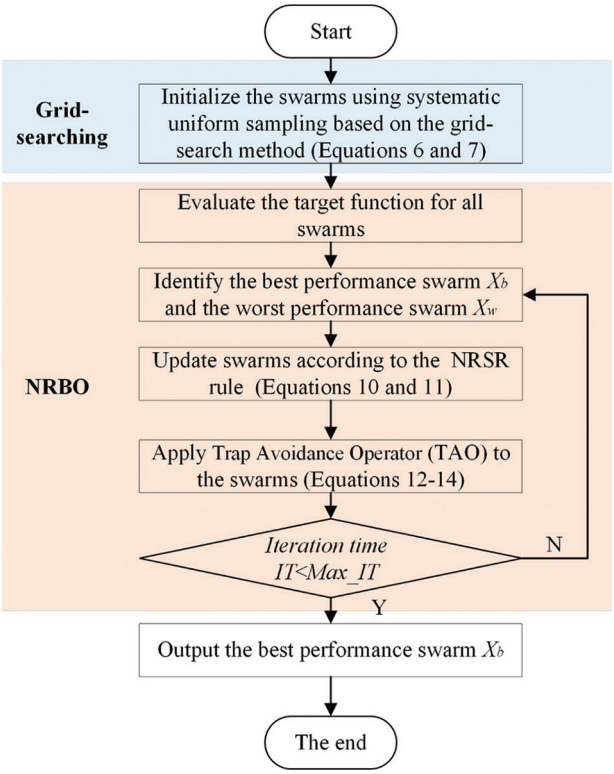

Figure 1. The flowchart of the proposed method. Abbreviations: NRBO: Newton–Raphson-based optimizer; NRSR: Newton–Raphson Search Rule.

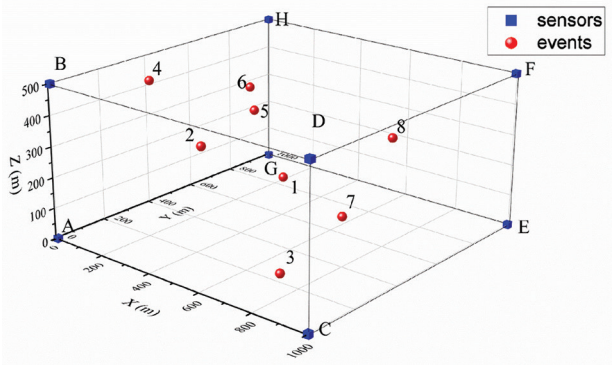

Figure 2. Sensor arrays and distribution of microseismic events.

algorithm, GA, PSO, and NRB)—were selected and benchmarked against the proposed approach.

3.1. Inversion results analysis on a single event

To evaluate the localization performance, synthetic P-wave arrival times were used, with each positioning method tested 10 times under identical conditions. For the H-J algorithm, 10 random initial values were generated per trial to assess robustness. The iteration parameters for the GA, PSO, NRBO, and the proposed method are detailed in Table 3.

Table 1. Coordinates of sensors in the monitoring area

Sensor	Coordinates of the sensors (m)		
	X	Y	Z
A	0	0	0
B	0	0	500
C	1000	0	0
D	1000	0	500
E	1000	1000	0
F	1000	1000	500
G	0	1000	0
H	0	1000	500

Table 2. Microseismic event locations and average velocities

Event	Event locations (m)			Velocity model (m/ms)	Origin time (ms)
	X	Y	Z	V	T_0
1	409	595	132	5	200
2	263	603	401	5	200
3	712	222	15	4.5	300
4	118	297	465	4.5	300
5	439	186	354	5.2	400
6	381	489	377	5.2	400
7	765	445	138	4.8	500
8	796	646	339	4.8	500

As shown in Table 4, the location errors and velocity inversion errors were evaluated based on the residual values of the objective function for each method. The results demonstrate that the PSO, NRBO, and the proposed method achieve higher positioning accuracy compared to the H-J algorithm and GA. The inversion results reveal that although the H-J algorithm converges close to the actual source location and approximates the average velocity in most cases, its solution often fails to reach the global optimum due to sensitivity to initial values, so the H-J method's positioning accuracy is significantly influenced by the selection of initial iteration points.

Furthermore, we observed that GNRBO achieves the same localization accuracy as NRBO. The proposed method employs a grid-search strategy for initial vector assignment instead of the random initialization used in NRBO. This approach is motivated by the fact that completely random initialization may concentrate all initial individuals in an unfavorable region of the search space. If this region is distant from the global optimum, the algorithm would require more time to explore other promising areas. In contrast, grid search ensures a uniform distribution of the initial population across the entire search space. As a result, GNRBO maintains the location accuracy of NRBO while mitigating the effects of random vector initialization. Given the near-identical characteristics of the two methods, the remainder of this paper discusses the performance of GNRBO only.

To evaluate the inversion accuracy and stability of the four comparison methods, we analyzed the residual curves of their objective functions (Figure 3). The results demonstrate that both the PSO method and the proposed method achieve superior localization accuracy compared to the other two approaches. Furthermore, both the H-J algorithm and PSO demonstrate susceptibility to local optima convergence. While the GA avoids this pitfall, its overall convergence performance remains suboptimal. Consequently, all three methods exhibit large standard deviations in their inversion results, indicating unsatisfactory stability in solution quality. As

Table 3. Iteration parameters of three algorithms for comparison

Method	The range of the searching spaces				Numbers of iteration vectors	Maximum number of iterations
	X (m)	Y (m)	Z (m)	Velocity (m/ms)		
GA	[0,1000]	[0,1000]	[0,500]	[3,7]	1000	500
PSO	[0,1300]	[0,1300]	[0,700]	[2,7]	144	500
NRBO	[0,1300]	[0,1300]	[0,700]	[2,7]	144	500
GNRBO	[−100,1300]	[−100,1300]	[−200,700]	[2,7]	144 (nx=ny=4; nz=nv=3)	500

Abbreviations: GA: Genetic Algorithm; GNRBO: Grid searching rule with an NRBO; PSO: Particle Swarm Optimization; NRBO: Newton-Raphson-based optimizer.

Table 4. Inversion results of each algorithm for No. 3 event

Method	No.	Inversion results				
		Values of target functions	Errors on X-axis (m)	Errors on Y-axis (m)	Errors on Z-axis (m)	Velocity error (m/ms)
H-J	1	1.1869	195.8000	91.4000	56.4000	1.6800
	2–3	8.2000×10^{-03}	5.9380×10^{-01}	8.3750×10^{-01}	5.9380×10^{-01}	1.2500×10^{-02}
	4–10	5.2000×10^{-03}	3.7190×10^{-01}	5.2500×10^{-01}	3.7190×10^{-01}	7.8000×10^{-03}
GA	1	5.1360×10^{-01}	8.4152	1.2599	2.6763	1.3820×10^{-01}
	2	2.2280×10^{-01}	14.3609	22.7735	15.0000	3.0720×10^{-01}
	3	2.3600×10^{-01}	16.4304	24.4575	15.0000	3.4540×10^{-01}
	4	2.4420×10^{-01}	2.6870	12.3826	6.6679	1.3020×10^{-01}
	5	3.9530×10^{-01}	13.0293	27.4312	15.0000	2.8820×10^{-01}
	6	1.7180×10^{-01}	10.1305	10.5638	7.8552	1.9130×10^{-01}
	7	2.0160×10^{-01}	13.8512	17.0293	11.3937	2.7560×10^{-01}
	8	4.9790×10^{-01}	24.8079	42.9948	15.0000	5.6530×10^{-01}
	9	4.9280×10^{-01}	10.9521	2.8080×10^{-01}	5.3883	8.1000×10^{-02}
	10	7.9480×10^{-01}	38.7396	64.3853	15.0000	8.5510×10^{-01}
PSO	1	1.7880×10^{-01}	11.2537	−15.7844	−15.0000	2.3200×10^{-01}
	2	8.9595×10^{-08}	5.4599×10^{-06}	-7.8945×10^{-06}	-6.3069×10^{-06}	1.0492×10^{-07}
	3	8.3187×10^{-08}	-3.6918×10^{-06}	6.0611×10^{-06}	4.7165×10^{-06}	-9.6966×10^{-08}
	4	1.7880×10^{-01}	11.2537	−15.7844	−15.0000	2.3200×10^{-01}
	5	9.9985×10^{-08}	5.8431×10^{-06}	-6.4691×10^{-06}	$-7.0337e\times10^{-06}$	1.1145×10^{-07}
	6	5.6938×10^{-08}	-3.6316×10^{-06}	3.8118×10^{-06}	2.8562×10^{-06}	-5.8678×10^{-08}
	7	8.0253×10^{-08}	-3.8333×10^{-06}	6.8407×10^{-06}	4.7161×10^{-06}	-8.4923×10^{-08}
	8	8.6374×10^{-08}	5.561×10^{-06}	-7.7736×10^{-06}	-3.8296×10^{-06}	1.1169×10^{-07}
	9	8.4415×10^{-08}	5.6505×10^{-06}	-7.6209×10^{-06}	-4.5538×10^{-06}	1.0542×10^{-08}
	10	5.8019×10^{-08}	3.5668×10^{-06}	-5.1631×10^{-06}	-2.4781×10^{-06}	7.1341×10^{-07}
NRBO	1	7.6025×10^{-08}	-4.6379×10^{-06}	4.9587×10^{-06}	3.3803×10^{-06}	-8.8197×10^{-08}
	2	7.9791×10^{-08}	5.4871×10^{-06}	-7.5024×10^{-06}	-5.0411×10^{-06}	1.1702×10^{-07}
	3	4.5000×10^{-08}	6.4174×10^{-07}	1.9462×10^{-07}	1.2416×10^{-06}	2.6760×10^{-09}
	4	7.9854×10^{-08}	4.8676×10^{-06}	-6.5382×10^{-06}	-6.4612×10^{-06}	1.0161×10^{-07}
	5	9.4780×10^{-08}	-3.5855×10^{-06}	6.8877×10^{-06}	6.4291×10^{-06}	-8.9947×10^{-08}
	6	5.4590×10^{-08}	1.4160×10^{-06}	-2.6378×10^{-06}	-2.7416×10^{-07}	4.1030×10^{-08}
	7	7.7556×10^{-08}	-3.5248×10^{-06}	4.6793×10^{-06}	5.2870×10^{-06}	-8.0933×10^{-08}
	8	9.6337×10^{-08}	2.8062×10^{-06}	-4.5705×10^{-06}	-5.1877×10^{-06}	8.0992×10^{-08}
	9	5.8400×10^{-08}	2.5450×10^{-06}	-2.3882×10^{-06}	-3.6217×10^{-06}	4.1128×10^{-08}
	10	8.9179×10^{-08}	9.6326×10^{-07}	6.7787×10^{-07}	1.6863×10^{-06}	-1.3462×10^{-08}
GNRBO	1	7.3513×10^{-08}	2.7158×10^{-06}	-4.2334×10^{-06}	-4.5209×10^{-06}	5.0032×10^{-08}
	2	9.2696×10^{-08}	8.009×10^{-07}	-1.7469×10^{-06}	-3.9857×10^{-06}	1.1163×10^{-08}
	3	6.325×10^{-08}	1.1668×10^{-06}	-1.4645×10^{-06}	-3.254×10^{-06}	3.1566×10^{-08}
	4	9.0051×10^{-08}	-1.1876×10^{-06}	-1.2955×10^{-06}	1.5039×10^{-06}	1.5501×10^{-09}
	5	7.6197×10^{-08}	-2.2943×10^{-06}	2.9585×10^{-06}	1.3215×10^{-06}	-6.004×10^{-08}
	6	9.9034×10^{-08}	2.2049×10^{-06}	-6.1565×10^{-06}	-3.8511×10^{-06}	7.6597×10^{-08}
	7	9.2146×10^{-08}	-3.2821×10^{-06}	5.5135×10^{-06}	6.2409×10^{-06}	-6.9132×10^{-08}
	8	5.795×10^{-08}	-3.2644×10^{-06}	4.9046×10^{-06}	4.1342×10^{-06}	-7.6801×10^{-08}
	9	4.4129×10^{-08}	-4.2491×10^{-06}	-2.9997×10^{-06}	-2.7219×10^{-06}	3.5641×10^{-08}
	10	5.1647×10^{-08}	2.8383×10^{-06}	-5.1605×10^{-07}	-1.2372×10^{-06}	9.7152×10^{-09}

Abbreviations: GA: Genetic Algorithm; GNRBO: Grid searching rule with an NRBO; H-J: Hooke-Jeeves algorithm; PSO: Particle Swarm Optimization; NRBO: Newton-Raphson-based optimizer.

evidenced by the residual curves, the improved algorithm demonstrates superior performance with both the smallest mean error and standard deviation in inversion results. These metrics confirm that the enhanced method achieves optimal accuracy and stability among the four compared approaches. Figure 4 presents a comparative analysis of location errors between the PSO method and the proposed method. While PSO results affected by local optima are omitted from the graph, the boxplot analysis reveals that the proposed method achieves superior convergence and stability in all three coordinate directions (X,Y,Z), with consistently lower location errors compared to PSO.

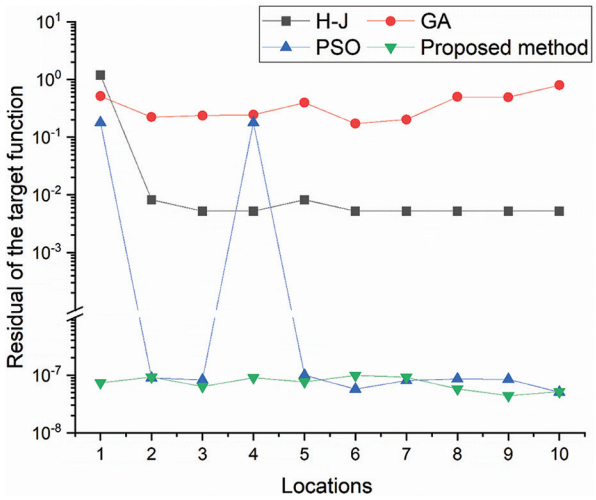

Figure 3. Residuals of the target functions of each location method for No.3 event.
Abbreviations: GA: Genetic Algorithm; H-J: Hooke-Jeeves algorithm; PSO: Particle Swarm Optimization.

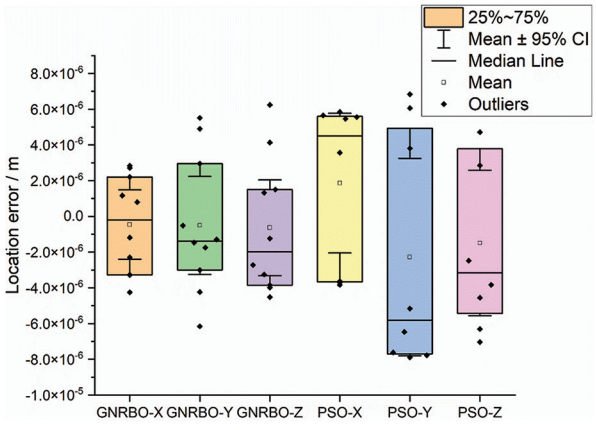

Figure 4. Location error analysis No.3 event, GNRBO-X,Y,Z are location errors on X,Y,Z directions obtained from GNRBO, PSO-X,Y,Z are location errors on X,Y,Z directions obtained from PSO function.
Abbreviations: CI: Confidence interval; GNRBO: Grid searching rule with an NRBO; PSO: Particle Swarm Optimization; NRBO: Newton–Raphson-based optimizer.

3.2. Inversion results analysis on multiple events

Using the theoretical P-wave arrival times derived from Tables 1 and 2, we applied four comparative localization methods to determine the source locations and velocity parameter for the eight microseismic events shown in Figure 3. Table 5 presents the comparative performance metrics for each method, including location errors, velocity inversion errors, and corresponding objective function values.

The results demonstrate that the H-J algorithm fails to accurately locate No.6 event, with positioning errors exceeding 50 m in both the *X* and *Z* directions. Additionally, the method yields a wave velocity error >3 mm/s.

The GA demonstrates unsatisfactory performance in both event localization and velocity inversion across all eight source events. The method fails to converge reliably to true values.

The PSO method demonstrates generally robust inversion performance, successfully converging to accurate estimates for all eight source events. However, convergence accuracy varies significantly across events, with particularly degraded performance for No.1 and 6 events compared to the other cases.

The proposed method demonstrates consistently accurate inversion results across all eight source events. The algorithm achieves unified inversion accuracy with the objective function converging to 10^{-8} magnitude. Spatial positioning errors in all three coordinate directions (X<Y, Z) converge to 10^{-7} magnitude, while velocity inversion errors stabilize at approximately magnitude.

Figure 5 presents the objective function residuals for all four methods, providing clear visual evidence of the proposed method's superior localization accuracy and stability. The residual distributions demonstrate that our approach consistently outperforms the comparison methods in both convergence precision and solution robustness.

Figure 6 presents a comparative analysis of localization errors between the PSO method and the proposed method. The boxplot visualization demonstrates superior performance of our approach in all three coordinate directions (X, Y, Z), exhibiting both enhanced convergence precision and greater solution stability compared to PSO.

4. Field data tests

To validate the practical engineering performance of the enhanced Newton–Raphson method, we conducted field verification using artificial blasting test data from a coal mine. The experimental setup included five controlled

Table 5. Location results of each algorithm for each source

Method	No.	Inversion results				
		Values of target functions	Errors on X-axis (m)	Errors on Y-axis (m)	Errors on Z-axis (m)	Velocity error (m/ms)
H-J	1	1.5800×10^{-02}	3.0125	3.1500	3.8563	1.6370×10^{-01}
	2	1.7500×10^{-02}	3.6625	1.4562	2.0937	7.2500×10^{-02}
	3	5.2000×10^{-03}	3.7190×10^{-01}	5.2500×10^{-01}	3.7190×10^{-01}	7.8000×10^{-03}
	4	1.0500×10^{-02}	1.4187	6.5000×10^{-01}	5.8750×10^{-01}	1.4400×10^{-02}
	5	3.1900×10^{-02}	2.2000	13.2375	3.7250	1.9750×10^{-01}
	6	1.2450×10^{-01}	51.5000	4.7000	54.5000	2.2200
	7	9.7000×10^{-03}	3.5000	6.3750×10^{-01}	1.3031	5.8400×10^{-02}
	8	2.1400×10^{-02}	4.0625	1.7875	9.6250×10^{-01}	6.1300×10^{-02}
GA	1	1.5100×10^{-01}	24.2526	21.5841	28.3689	1.2074
	2	2.8220×10^{-01}	15.6375	4.5920×10^{-01}	8.1980×10^{-01}	2.3230×10^{-01}
	3	1.2350×10^{-01}	8.6080	11.1370	6.5965	1.7040×10^{-01}
	4	4.4900×10^{-01}	46.0113	17.4678	22.8855	4.8210×10^{-01}
	5	2.2850×10^{-01}	8.4517	56.6445	13.4975	7.2600×10^{-01}
	6	8.8500×10^{-02}	16.3381	1.2082	20.0927	7.4680×10^{-01}
	7	2.7640×10^{-01}	108.8177	18.3472	41.8598	1.7117
	8	3.4350×10^{-01}	70.7686	28.7896	15.1159	1.0203
PSO	1	1.7831×10^{-07}	-3.3764×10^{-05}	3.5527×10^{-05}	-4.3877×10^{-05}	1.8437×10^{-06}
	2	9.2647×10^{-08}	3.7085×10^{-06}	-3.0127×10^{-06}	-5.1292×10^{-06}	-9.4259×10^{-08}
	3	8.0139×10^{-08}	-1.0875×10^{-06}	2.8362×10^{-06}	-2.2989×10^{-07}	-2.0578×10^{-08}
	4	9.3529×10^{-08}	-1.0386×10^{-05}	-4.7081×10^{-06}	6.3319×10^{-06}	1.0535×10^{-07}
	5	9.1667×10^{-08}	-6.5514×10^{-06}	-3.6093×10^{-05}	1.07×10^{-05}	5.3501×10^{-07}
	6	9.0373×10^{-06}	3.802×10^{-03}	3.8134×10^{-04}	4.005×10^{-03}	1.6129×10^{-04}
	7	9.688×10^{-08}	3.4813×10^{-05}	-6.3431×10^{-06}	-1.3297×10^{-05}	5.7872×10^{-07}
	8	9.6529×10^{-08}	-1.6689×10^{-05}	-8.0528×10^{-06}	-3.9844×10^{-06}	-2.4895×10^{-07}
GNRBO	1	4.327×10^{-08}	4.2794×10^{-06}	-3.3897×10^{-06}	5.2613×10^{-06}	-2.1536×10^{-07}
	2	9.0878×10^{-08}	-1.4828×10^{-05}	5.6007×10^{-06}	6.2505×10^{-06}	2.9693×10^{-07}
	3	9.7437×10^{-08}	-3.2897×10^{-06}	2.0745×10^{-06}	1.8301×10^{-06}	-2.9323×10^{-08}
	4	9.5457×10^{-08}	-5.2046×10^{-06}	-6.455×10^{-07}	9.316×10^{-07}	5.0079×10^{-08}
	5	6.9913×10^{-08}	-4.8094×10^{-07}	-2.5568×10^{-05}	6.3122×10^{-06}	3.8051×10^{-07}
	6	7.8638×10^{-08}	-1.9404×10^{-05}	-5.3375×10^{-07}	2.061×10^{-06}	8.487×10^{-07}
	7	6.8855×10^{-08}	6.8963×10^{-07}	-1.4791×10^{-06}	-7.0659×10^{-07}	1.2122×10^{-08}
	8	8.4659×10^{-08}	-1.1105×10^{-05}	-4.7895×10^{-06}	-3.5174×10^{-06}	-1.8259×10^{-07}

Abbreviations: GA: Genetic Algorithm; GNRBO: Grid searching rule with an NRBO; H-J: Hooke-Jeeves algorithm; PSO: Particle Swarm Optimization; NRBO: Newton-Raphson-based optimizer.

blasts, with sensor and blast locations detailed in Figure 7A and Tables 6, 7. The parameters of the GNRBO are illustrated in Table 8. Field-acquired P-wave arrival times, documented in Table 9, served as input data for the inversion. Note that neither the velocity model nor the exact origin times of the blasts were known *a priori*, reflecting realistic field conditions.

The localization results are presented in Figure 7A-D and Table 10 presents a comparative analysis of localization results between the proposed method and the coal mine's existing monitoring system. The P-wave arrival times used for both methods were selected based on signal-to-noise ratio criteria from the field data. The location results compared to the existing monitoring system, particularly in the vertical direction. Notably, the method achieves sub-10 m vertical accuracy for four out of five test events, representing a critical improvement for coal mine microseismic monitoring applications where vertical precision is paramount.

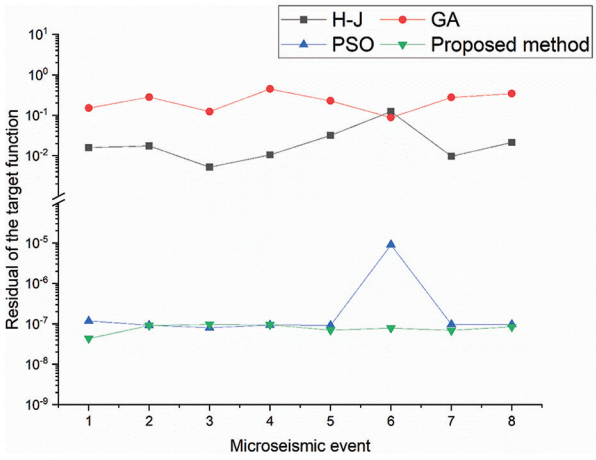

Figure 5. Residuals of the target functions of each location method for all events.
Abbreviations: GA: Genetic Algorithm; H-J: Hooke-Jeeves algorithm; PSO: Particle Swarm Optimization.

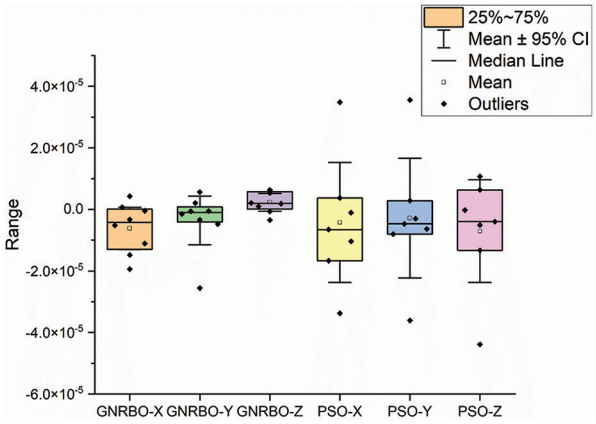

Figure 6. Location error analysis for eight events. GNRBO-X,Y,Z are location errors on X,Y,Z directions obtained from GNRBO, while PSO-X,Y,Z are location errors on X,Y,Z directions obtained from PSO.
Abbreviations: CI: Confidence interval; GNRBO: Grid searching rule with an NRBO; PSO: Particle Swarm Optimization; NRBO: Newton–Raphson-based optimizer.

5. Discussion

The current study introduces a novel approach to microseismic event location that integrates grid search principles with a Newton-Raphson-based optimizer (GNRBO). Unlike conventional arrival-time-based localization techniques, the proposed method does not require an *a priori* velocity model. Instead, it refines estimates within a four-dimensional search space (X, Y, Z, and velocity) to achieve high-precision inversion results. Given that accurate velocity parameters are often difficult to estimate or may vary during microseismic monitoring, this velocity-independent approach enhances localization accuracy.

Table 6. Coordinates of sensors in the monitoring area

Sensor	Coordinates of the sensors (m)		
	X	Y	Z
A	1490.0000	1939.3000	−870.0000
B	1416.3000	2172.4000	−887.2000
C	1350.3000	2381.5000	−890.6000
D	1519.3700	1847.5200	−866.2000
E	1767.6000	1972.2000	−900.1000
F	1699.6000	2188.7000	−908.1000
G	1623.4000	2428.4000	−915.2000
H	1685.0900	2233.5400	−904.0000
I	1467.2700	2011.5000	−878.0000
J	1399	2228.1800	−891.0000
K	1416	2170.4000	−908.5000
L	1454.9800	2050.4900	−875.7000
M	1758.3400	2001.6200	−905.0000
N	1668.1300	2287.6100	−912.0000

Table 7. True locations of microseismic events

Events	Event locations (m)		
	X	Y	Z
1	1474.1840	1984.0200	−858.0000
2	1480.6530	1955.5570	−862.0000
3	1707.8340	2139.8480	−879.0000
4	1707.2180	2129.1720	−879.0000
5	1710.8630	2130.2520	−879.0000

Existing methods, such as the original NRBO[22] and PSO, initialize search particles randomly within the solution space, which may lead to convergence at local optima rather than the global optimum—as demonstrated by the results in Table 4. In contrast, GNRBO ensures robustness by systematically generating initial iterative vectors through uniform sampling of the search space. This strategy increases the likelihood of at least one particle being sufficiently close to the global optimum, thereby improving convergence reliability.

In the synthetic data tests, we first evaluated the inversion performance for a single microseismic event. As illustrated in Figures 3-5, the proposed GNRBO method achieves significantly higher localization accuracy and greater stability compared to the three benchmark methods (H-J, GA, and PSO). While H-J and GA yield suboptimal results, PSO exhibits a tendency to converge to local optima, compromising its reliability.

Subsequently, we extended the analysis to multiple events. Figure 5 demonstrates that GNRBO successfully

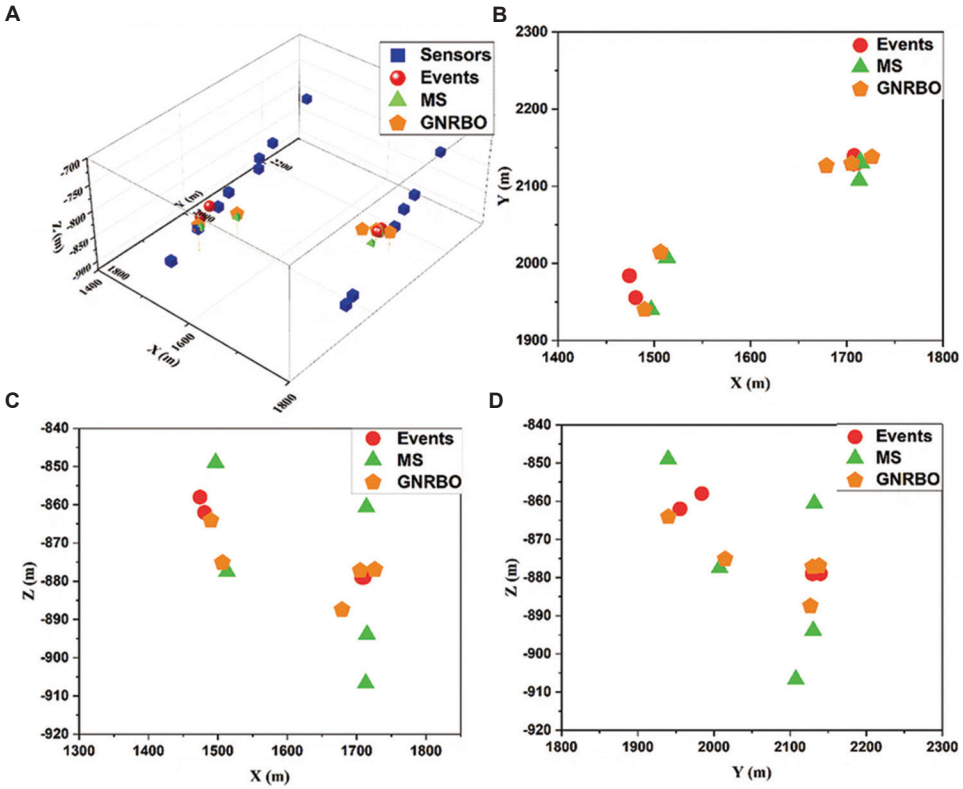

Figure 7. Microseismic monitoring in a coal mine. (A) Location results (X-Y-Z); (B) Location results (X-Y); (C) Location results (X-Z); (D) Location results (Y-Z). Abbreviations: GNRBO: Grid searching rule with an NRBO; MS: Monitoring system; NRBO: Newton–Raphson-based optimizer.

Table 8. Iteration parameters of GNRBO

Method	The range of the searching spaces				Numbers of iteration vectors	Maximum number of iterations
	X (m)	Y (m)	Z (m)	Velocity (m/ms)		
GNRBO	[1000,2000]	[1500,2500]	[−700,−1000]	[3.5]	3025 (*nx*=*ny*=11; *nz*=*nv*=5)	500

Abbreviations: GNRBO: Grid searching rule with an NRBO; NRBO: Newton-Raphson-based optimizer.

Table 9. P-wave arrival time from the field data

Sensors	Arrival times of each event (s)				
	No. 1	No. 2	No. 3	No. 4	No. 5
1	14.1120	6.0780	10.2340	9.7020	6.7560
2	14.1460	6.1340	10.2340	9.7040	6.7580
3	14.1880	/	10.2660	9.7360	6.7900
4	14.1360	6.1000	10.2460	9.7140	/
5	/	/	10.2060	/	6.7280
6	14.1560	/	10.1780	9.6500	6.7040
7	14.2000	/	10.2360	9.7080	6.7600
8	14.1600	/	10.1880	9.6600	6.7140
9	14.0960	6.0940	10.2280	9.6980	6.7520
10	14.1520	6.1440	10.2400	9.7100	6.7640
11	14.1360	6.1400	10.2280	9.6960	6.7500
12	/	/	/	/	/
13	14.1740	6.1380	/	9.6740	/
14	14.1680	6.1700	/	9.6800	6.7300

locates all eight events with high precision, outperforming the other methods. A detailed comparison of localization errors along the X, Y, and Z axes (Figure 6) further confirms the robustness of GNRBO, as evidenced by the consistently smaller error distributions in the boxplot visualization. These results conclusively demonstrate that GNRBO delivers reliable and accurate event localization in synthetic datasets, validating its superiority over benchmark method in this paper.

To evaluate the practical performance of GNRBO, we conducted field tests using artificial blasting data from a coal mine, comparing results against the mine's installed monitoring system. As demonstrated in Figure 7 and Table 10, GNRBO significantly outperforms the conventional monitoring system in localization accuracy. Detailed analysis reveals that GNRBO achieves vertical accuracy within 10 m for 80% of test events (4 out of 5), demonstrating particular improvement in vertical positioning—a critical factor for coal mine safety monitoring. These results confirm GNRBO's

Table 10. Location results based on the field datasets

Event no.	Location error (monitoring system)		Location error (GNRBO)		
	Horizontal error (m)	Vertical error (m)	Horizontal error (m)	Vertical error (m)	Sensors used
1	45.5400	19.5000	44.5300	−17.4600	A, B, C, D, F, G, H, I, J, K, M, N
2	22.4900	13.0000	17.9900	−1.5200	A, B, D, I, J, K
3	32.7700	27.7000	31.7100	−6.9900	A, B, C, D, F, G, H, I, J, K, M, N
4	7.3300	18.4000	2.1300	0.7800	A, B, C, D, F, G, H, I, J, K, M, N
5	4.2400	14.9000	17.1800	1.3500	No. 1,2,3,5,6,7,8,9,10,11,14 A, B, C, E, F, G, H, I, J, K, N

superior performance in real-world applications compared to existing monitoring solutions.

6. Conclusion

This study presents an enhanced microseismic localization and velocity inversion approach that synergistically combines grid search methodology with the Newton-Raphson algorithm. The hybrid method demonstrates significant improvements in localization accuracy and solution stability. Through comprehensive validation using both synthetic and field datasets, we comparatively evaluate our method against three established optimization techniques: the H-J algorithm, GA, and PSO. The key findings are summarized as follows:

(i) The grid search method systematically partitions the solution space to eliminate unreliable localization results caused by randomly-assigned initial vectors. By providing optimized initial parameters for the Newton-Raphson algorithm, this approach maintains high positioning accuracy while significantly improving solution stability. The grid-derived initialization vectors effectively prevent convergence to local optima.

(ii) Using synthetic data, we evaluated the inversion performance of the Newton-Raphson method in comparison with three established optimization approaches: the H-J algorithm, GA, and PSO. Through comprehensive analysis of objective function values, localization errors, and average velocity inversion errors, the results demonstrate that the proposed method achieves superior and more stable positioning accuracy.

(iii) The proposed method was validated using field data from a coal mine microseismic monitoring system. Comparative analysis with the existing localization system demonstrates superior accuracy of our approach, particularly in vertical positioning. The results reveal consistent improvements in depth estimation precision, achieving sub-10-m vertical accuracy for of seismic events (4 out of 5 test cases), which represents a critical enhancement for mine safety applications.

Acknowledgments

None.

Funding

This research was supported by the National Natural Science Foundation of China (42474189), the Open Fund Project of State Key Laboratory for Fine Exploration and Intelligent Development of Coal Research (SKLCRSM23KFA04), and the Science and Technology Innovation Team of Shandong Earthquake Agency (TD202404).

Conflict of interest

The authors declare they have no competing interests.

Author contributions

Conceptualization: Tianqi Jiang
Formal analysis: Shaohui Zhou, Yu Wang, Yajun Li
Investigation: Peng Lin
Methodology: Tianqi Jiang
Visualization: Peng Lin
Writing–original draft: Shaohui Zhou, Junhao Qu
Writing–review & editing: Shaohui Zhou

Availability of data

Data is available from the corresponding author upon reasonable request.

References

1. Ge M, Mrugala M, Iannacchione AT. Microseismic monitoring at a limestone mine. *Geotech Geol Eng.* 2009;27(3):325-339.

   doi: 10.1007/s10706-008-9234-z

2. Verdon JP, Stork AL, Kendall JM. Geomechanical modelling, microseismic monitoring and CO_2 storage. In: *EAGE/SPE Workshop on Integrated Geomechanics in Exploration and Production*. Netherlands: European Association of Geoscientists and Engineers; 2016. p. 1-5.

3. Kim K, Lees JM. Imaging volcanic infrasound sources

using time reversal mirror algorithm. *Geophys J Int*. 2015;202(3):1663-1676.

doi: 10.1093/gji/ggv237

4. Rentsch S, Buske S, Lüth S, Shapiro SA. Fast location of seismicity: A migration-type approach with application to hydraulic-fracturing data. *Geophysics*. 2007;72(1):S33-S40.

doi: 10.1190/1.2401139

5. Geiger L. Probability method for the determination of earthquake epicenters from the arrival time only. *Bull St Louis Univ*. 1912;8:60-71.

6. Li N, Wang E, Ge M, Sun Z. A nonlinear microseismic source location method based on simplex method and its residual analysis. *Arab J Geosci*. 2014;7(11):4477-4486.

doi: 10.1007/s12517-013-1121-0

7. Dong L, Li X, Zhou Z, Chen G, Ma J. Three-dimensional analytical solution of acoustic emission source location for cuboid monitoring network without premeasured wave velocity. *Trans Nonferrous Met Soc China*. 2015;25(1):293-302.

doi: 10.1016/S1003-6326(15)63604-4

8. Kushnir A, Varypaev A, Dricker I, Rozhkov M, Rozhkov N. Passive surface microseismic monitoring as a statistical problem: Location of weak microseismic signals in the presence of strongly correlated noise. *Geophys Prospect*. 2014;62(4):819-833.

doi: 10.1111/1365-2478.12124

9. Zheng J, Lu J, Jiang T, Liang Z. Microseismic event denoising via adaptive directional vector median filters. *Acta Geophys*. 2017;65(1):47-54.

doi: 10.1007/s11600-017-0005-1

10. Zheng J, Lu J, Peng S, Jiang T. An automatic microseismic or acoustic emission arrival identification scheme with deep recurrent neural networks. *Geophys J Int*. 2018;212(3):1389-1397.

doi: 10.1093/gji/ggx487

11. Li Y, Wang H, Fehler M, Fu Y. Wavefield characterization of perforation shot signals in a shale gas reservoir. *Phys Earth Planet Inter*. 2017;267:31-40.

doi: 10.1016/j.pepi.2017.04.003

12. Prange MD, Bose S, Kodio O, Djikpesse HA. An information-theoretic approach to microseismic source location. *Geophys J Int*. 2015;201(1):193-206.

doi: 10.1093/gji/ggv009

13. Jia B, Li F, Pan Y, Zhou L. Microseismic source locating method based on variable step size accelerated search. *Rock Soil Mech*. 2022;43(9):1-9.

doi: 10.16285/j.rsm.2021.5872

14. Cheng J, Song G, Liu T, Hu B, Wang J, Wang J. High precision location of micro-seismic source in underground coal mine. *Chin J Geophys*. 2016;59(2):734-743.

doi: 10.1002/cjg2.30021

15. Gong S, Dou L, Ma X, Liu J. The method to identify the optimal channel numbers for increasing the location accuracy of microseismic events in coal mine. *J China Coal Soc*. 2010;35(12):2017-2021.

doi: 10.13225/j.cnki.jccs.2010.12.014

16. Gong S, Dou L, Ma X, Mu Z, Lu C. Optimization algorithm of network configuration for improving location accuracy of microseism in coal mine. *Chin J Rock Mech Eng*. 2012;31(1):8-17.

17. Duncan PM, Eisner L. Reservoir characterization using surface microseismic monitoring. *Geophysics*. 2010;75(5):139-146.

doi: 10.1190/1.3467760

18. Jiang T, Pei S. Micro-seismic event location based on Newton iteration method and grid-search method. *J Min Sci Technol*. 2019;4(6):480-488.

doi: 10.19606/j.cnki.jmst.2019.06.002

19. Lü J, Jiang Y, Zhao Y, Zhu J, Wang X, Tao L. Study of microseismic positioning based on steady simulated annealing-simplex hybrid algorithm. *Rock Soil Mech*. 2013;34(8):2195-2203.

doi: 10.16285/j.rsm.2013.08.024

20. Luo H, Yu J, Pan Y, Song B, Liu L, Liang J. Seagull optimization based on quantile difference mine earthquake location method. *Prog Geophys*. 2022;37(1):421-429.

doi: 10.6038/pg2022FF0401

21. Dong L, Li X, Tang L, Gong F. Mathematical functions and parameters for microseismic source location without pre-measuring speed. *Chin J Rock Mech Eng*. 2011;30(10):2057-2067.

22. Sowmya R, Premkumar M, Jangir P. Newton-Raphson-based optimizer: A new population-based metaheuristic algorithm for continuous optimization problems. *Eng Appl Artif Intell*. 2024;128:107532.

doi: 10.1016/j.engappai.2023.107532

RETRACTION NOTE

DOI: 10.36922/jse.corr090125
Published online: September 9, 2025

Kong L, Tian Y, YU H, Liu H, Zhou H. Efficient and low-cost node seismic data recovery based on curvelet compression sensing. *Journal of Seismic Exploration*. 2024;33(4):1–21.

This article is retracted at the request of the authors and with the approval of the Editor-in-Chief of *Journal of Seismic Exploration*. The article was originally published while the journal was still under the management of the former publisher, prior to its acquisition by AccScience Publishing.

This retraction is due to an editorial oversight in the manuscript handling process at the prior publisher, which resulted in the authors receiving no formal decision on their submission within an expected timeframe. Without any notice from the prior publisher, authors were completely unaware of the article's acceptance and publication by the *Journal of Seismic Exploration* on November 11, 2024. Believing the manuscript was no longer under consideration by *Journal of Seismic Exploration*, the authors subsequently submitted it to *Applied Geophysics* on August 15, 2024, where it was accepted and published on November 21, 2024 (https://doi.org/10.1007/s11770-024-1141-4). This unintentionally resulted in duplicate publication. The retraction is made to uphold the integrity of the scholarly record.

All authors are aware of this issue and agree to this retraction.

Our Journals

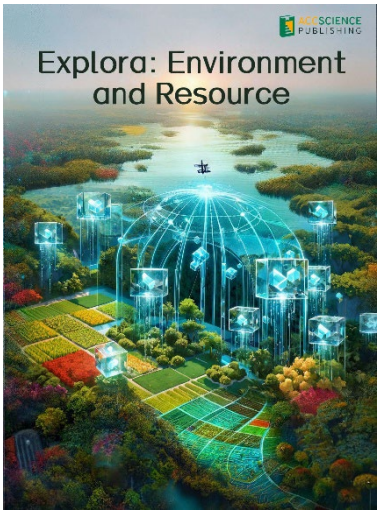

Explora: Environment and Resource (EER) is an international and multidisciplinary journal covering all aspects of the environmental impacts of socio-economic development. It is concerned with the complex interactions among society, development, and the environment, aiming to explore ways and means of achieving sustainability in all human activities related to development.

EER covers subject areas, including but not limited to the following:

- Water reclamation, wastewater treatment and waste management for eco-environment sustainability
- Innovative nanotechnology, catalysis, photocatalysis and nano materials for decontamination practices and renewable energy resources.
- Climate change-related sustainable resource and environment quality analysis
- Microorganisms and plants-oriented low-carbon processes and strategies for clean energy, water and resource management

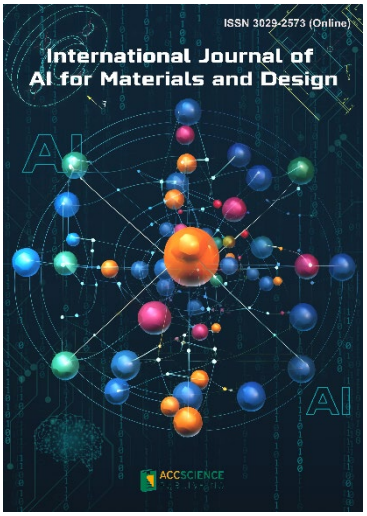

International Journal of AI for Materials and Design is an international, peer-reviewed open-access journal that aims to bridge the cutting-edge research between AI and materials, AI and design. In recent years, the tremendous progress in AI is leading a radical shift of AI research from a mainly academic endeavor to a much broader field with increasing industrial and governmental investments. The maturation of AI technology brings about a step change in the scientific research of various domains, especially in the world of materials and design. Machine learning (ML) algorithms enable researchers to analyze extensive datasets on material properties and accurately predict their behavior in different conditions. This subsequently impact the industry to leverage on big data and advanced analytics to build scientific strategies, scale operational performance of processes and drive innovation. In addition, AI and ML are uniquely positioned to enable advanced manufacturing technologies across the value chain of different industries. Integration of multiple and complementary AI techniques, such as ML, search, reasoning, planning, and knowledge representation, will further accelerate advances in scientific discoveries, engineering excellence and the future of cyber-physical systems manufacturing.

International Journal of AI for Materials and Design covers the following topics: AI or machine learning for material discovery, AI for process optimization, AI and data-driven approaches for product or systems design, application of AI in advanced manufacturing processes such as additive manufacturing, IoT, sensors, robotics, cloud-based manufacturing, intelligent manufacturing for various applications, autonomous experiments, material intelligence, energy intelligence, and AI-linked decarbonization technologies.

Start a new journal

Write to us via email if you are interested to start a new journal with AccScience Publishing. Please attach your CV, professional profile page and a brief pitch proposal in your email. We shall inform you of our decision whether we are interested to collaborate in starting a new journal.

Contact: info@accscience.com

https://accscience.com/journal/JSE

Access Science Without Barriers

Contact

www.accscience.com
9 Raffles Place, Republic Plaza 1 #06-00 Singapore 048619
E-mail: editorial@accscience.com
Phone: +65 8182 1586